Defect Design, Chemical Synthesis and Associated Properties of Multifunctional TiO_2-Based Nanocrystals

by

Qingbo Sun

Research School of Chemistry

ANU College of Physical & Mathematical Sciences

The Australian National University

Sullivans Creek Road

Canberra, Australian Capital Territory, 2601, Australia

A thesis submitted for the degree of Doctor of Philosophy of

The Australian National University

Australian National University

July, 2017

Originality Statement

I hereby declare that this thesis is a collection of my major outcomes arising from my own independent research work during the PhD program. To the best of my knowledge, this thesis does not contain any material previously published or written by another person, or substantial proportions of materials which have been accepted for the award of any other degree or diploma at the Australian National University (ANU) or any other educational institution, except where the acknowledgement and references are made in the thesis. Any contribution made to the research by others, with whom I have worked at ANU or elsewhere, is explicitly acknowledged in the thesis. Regarding to all the publications presented herein, where multiple co-authors are involved, my contribution to these publications has been explicitly stated on the title pages. I also declare that the intellectual content of this thesis is the product of my own work, except to the extent that assistance from others in the project's design and conception or in style, presentation and linguistic expression is acknowledged.

Signed: Qingbo Sun

Date: 2^{ed} July 2017

Copyright Statement

Signed: Qingbo Sun

Date: 2ed July 2017

Authenticity Statement

I certify that the library deposit digital copy is a direct equivalent of the final officially approved version of my thesis. No emendation of content has occurred and if there are any minor variations in formatting, they are the result of the conversion to digital format.

Signed: Qingbo Sun

Date: 2ed July 2017

Abstract

Local defect structures are significant to determine material properties since the defects introduced into host materials would affect their local/average crystal environments and thus lead to a change of their macroscopic physicochemical performances. The intentional design of specific local defect states in materials not only depends on the selected synthesis method and preparation process but also relies on the selected dopant or co-dopant ions. A deep understanding of the intrinsic relationships between local defect structures, chemical synthesis and associated properties is thus thought as one major framework of material genome plan. It also significantly pushes the design, development and application of novel multifunctional materials.

Based on local defect structural design coupled with new synthesis strategies, (In^{3+}, Nb^{5+}) co-doped anatase TiO_2 nanocrystals with the complicated chemical formula of $(Ti^{4+}_{1-x-y-z}Ti^{3+}_{x}In^{3+}_{y}Nb^{5+}_{z})(O^{2-}_{2-(x+y-z)/2}\square_{y/2})$ are synthesized by a solvothermal method ($\square$ here represents oxygen vacancies and also labelled as $V_O^{\bullet\bullet}$). It is experimentally demonstrated that the dual mechanisms of nucleation and diffusion doping are responsible for the synergistic incorporation of difficult-dopant In^{3+} ions and easy-dopant Nb^{5+} ions, and theoretically evidenced that the local defect structures created by the introduced In^{3+}, Nb^{5+} co-dopants, the resultant Ti^{3+} and $V_O^{\bullet\bullet}$ are composed of both $2In'_{Ti}+V_O^{\bullet\bullet}+Ti'_{Ti}+Nb^{\bullet}_{Ti}$ defect clusters and equivalent $Ti'_{Ti}+Nb^{\bullet}_{Ti}$ defect pairs. These introduced local defect structures then act as nucleation centres of baddeleyite- and α-PbO_2-like metastable polymorphic phases and induce an abnormal trans-regime structural transition of co-doped anatase TiO_2 nanocrystals under high pressure. Furthermore, the (In^{3+}, Nb^{5+}) co-doped anatase TiO_2 small nanocrystals with average particle sizes of less than 10 nm can also be used as raw materials to large-scaly manufacture a new generation of TiO_2-based ceramic capacitors designed in terms of electron-pinned defect dipole mechanism. Through the utilization of these small nanocrystals, the sintering temperature of ceramic capacitors can be lowered to about 1200 °C and thus conquers the technological bottleneck facing the fabrication of ceramic capacitors using this type of materials.

To develop the third generation of high-efficient visible light catalysts, (N^{3-}, Nb^{5+}) co-doped anatase TiO_2 nanocrystals with the formula of $(Ti^{4+}_{1-x-y}Ti^{3+}_{x}Nb^{5+}_{y})(O^{2-}_{2-y'-z}\square_{z}N^{3-}_{y'})$ are synthesized through a solvothermal reaction route for efficiently introducing nitrogen

ions into host TiO_2 materials and simultaneously avoiding nitrogen evaporation during subsequent high temperature processing. Experimental and theoretical investigations demonstrate that the formation of highly concentrated defect-pairs between N^{3-} and Nb^{5+} co-dopant ions is key to enhance visible light absorption of TiO_2 nanocrystals, prevent the recombination or trapping of photo-generated charge carrier, and significantly improve visible light catalytic efficiency. It is thus unveiled that a fundamental understanding of the functions of local defect structures and a well-controlled synthetic strategy are critical to develop highly efficient visible light catalysts with unprecedented photocatalytic performances.

In combination of local defect structural design and the exploration of new synthesis strategies, $(Ti^{4+}_{1-x}Ti^{3+}_{x})(O^{2-}_{2-y-z}N^{3-}_{y}\square_{z})$ anatase nanocrystals containing N^{3-} and Ti^{3+} ions are synthesized by using $TiCl_4$ as Ti source, HNO_3 as nitrogen source and ethanol as a reaction solvent. In this material, Ti^{3+}-V_O-$2Ti^{4+}$-N^{3-} defect clusters are formed in anatase TiO_2 nanocrystals and the visible light catalytic properties are greatly enhanced thereof. The formation of local Ti^{3+}-V_O-$2Ti^{4+}$-N^{3-} defect clusters is finally demonstrated to play an important role on the obvious enhancement of Rhodamine B degradation efficiency under only visible light illumination. In further comparison with (In^{3+}, Nb^{5+}) and (N^{3-}, Nb^{5+}) co-doped anatase TiO_2 nanocrystals, it can be concluded that the local defect structures generated by introduced co-dopant ions are complicated in strong-correlated TiO_2 systems and differ from case to case.

Through these systematic investigations on ions co-doped TiO_2 nanocrystals, a major difficulty to efficiently introduce difficult-dopant ions such as N^{3-} and In^{3+} into TiO_2 crystal structures at high concentrations, especially, through wet chemical synthesis, is solved. Two types of high-efficient TiO_2-based visible light catalysts are achieved for environmental remediation by directly using the clean and renewable solar energy; and one raw material for the manufacture of new ceramic capacitors and new TiO_2 metastable polymorphic phases is provided. The discussion on the doping mechanisms, the defect formation and their associated impacts on material performances will not only benefit the future development of physical chemistry, material science and defect chemistry, but also open a new route to design novel multifunctional materials based on local defect structures in materials.

Acknowledgement

To help me achieve the potential to undertake and complete my PhD project, I have obtained the guidance, goodwill and support of a number of people for which I am deeply grateful.

First and foremost, I would like to sincerely thank my supervisor prof. Yun Liu for providing me the PhD opportunity and financially supporting the whole research program during my PhD period. Without her constructive guidance, continuous support, thorough trust and professional comments, I would never succeed in achieving such fruitful research outcomes presented in the thesis. Her supervision also makes the journey towards the completion of my PhD degree rather enjoyable and unforgettable. I am so grateful for being supervised by her and appreciate the invaluable knowledge and analytical skills that she shares with me. More importantly, I have to mention that prof. Yun Liu is an outstanding mentor since she not only teaches me how to do research work but also teaches me how to think in a positive, engaging and supportive manner. I believe that all the experience with her is the most valuable wealth in my life.

I would also like to thank prof. Ray L. Withers for his broad knowledge and unique understanding of local crystal structures. Under his guidance, I deeply comprehend the key functions of local crystal structure on material performances.

I also specially acknowledge Dr. Hua Chen (the Centre for Advanced Microscopy, CAM-ANU) for his expert assistance in the characterization of scanning electron microscopy and related sample preparation, Dr. Lasse Norén for his excellent advice on the analysis of X-ray diffraction patterns, Dr. Terry J. Frankcombe (the University of New South Wales, UNSW) and Dr. David Cortie (the Australian Nuclear Science and Technology Organisation, ANSTO) for their assistance on theoretical calculations during my PhD candidature.

I also sincerely appreciate the collaborative work with prof. Wensheng Shi (the Technical Institute of Physics and Chemistry, Chinese Academy of Sciences, TIPC-CAS), prof. Joanne Etheridge (Monash Centre for Electron Microscopy, Monash University, MCEM-MU), prof. Yuping Zeng (Shanghai Institute of Ceramics, Chinese Academy of Sciences, SIC-CAS), associated prof. Jodie E. Bradby (Research School of Physics and Engineering, the Australian National University, RSPE-ANU), associated prof. Lan Fu (RSPE-ANU), associated prof. Kaihui Zuo (SIC-CAS), Dr. Dehong Yu (ANSTO), Dr. Leigh R.

Sheppard (the Western Sydney University), Dr. Changlin Zheng (MCEM-MU), Ms. Larissa Q. Huston (RSPE-ANU), Mr. Shaoyang Zhang (TIPC-CAS), Mrs. Jie Gao (SIC-CAS), Mr. Muhammad Qadeer Awana (Bahauddin Zakariya University), Mrs Yuanyuan Sun (Changzhou Vocational Institute of Engineering). Due to their collaboration, I can complete my PhD project earlier.

Thanks are also given to the Australian Research Council (ARC) and the Fenghua Advanced Technology Holding Co., Ltd. for their financial support on this thesis work and my other related PhD studies.

Thanks also go to my friendly and lovely colleagues Dr. Wanbiao Hu, Dr. Chunming Wang, Dr. Yuanlie Yu, Dr. Dehong Chen, Dr. Jian Wang, Dr. Kenny Lau, Mr. Wen Dong, Mr. Teng Lu, Mr. Xiaozhou Wang, Mr. Haoxin Mai, Ms. Bethany McBride and many other team members or friends who gave me their support and encouragement in the past few years.

Last but not least, special thanks are also expressed to my mother, my wife Lin Li, my two younger daughters Ruoran Sun and Ruoxi Sun, and other family members who have always believed in me and cheering me up to pursue my interest throughout my PhD study. Their love and encouragement are worth more than I can express in words.

Qingbo Sun (RSC, ANU)

Date: 2ed July 2017

List of Symbols and Abbreviations

Nomenclature

GPa	Gigapascal
GII	Global instability index
r	Ionic radii
n	Refractive index
$Loss\ tan\delta$	Dielectric loss
ε_r	Relative dielectric constant
kV	Kilovolt
mA	Milliamperes
λ	Wavelength
β	The line broadening at half the maximum intensity
θ	The Bragg angles
A_m	The cross-sectional area
L_{av}	The Avogadro's number
W_t	The molecular weight

Acronyms

UV	Ultraviolet
Vis	Visible
ITO	Indium tin oxide
TiO_2	Titanium dioxide
In	Indium

Nb	Niobium
N	Nitrogen
XRD	X-ray diffraction
TEM	Transmission electron microscopy
SEM	Scanning electron microscopy
STEM	Scanning transmission electron microscopy
HADDF	High-angle annular dark-field
XPS	X-ray photoelectron spectroscopy
ICP-OES	Inductively coupled plasma optical emission spectroscopy
TGA	Thermogravimetric analysis
FT-IR	Fourier transform infrared spectroscopy
B.E.T.	Bruauer-Emmett-Teller
DOS	Density of state
PDOS	Projected density of state

Table of Contents

List of Figures

List of Tables

Chapter 1. Introduction

In recent years, titanium dioxide (TiO_2) and TiO_2-based materials (*e.g.* self-modified TiO_2, extrinsic elements doped/co-doped TiO_2, a mixture of two or more polymorphic TiO_2, and the composites of TiO_2 with other materials *etc.*) have attracted broad research and industrial interest since they possess multifunctional features and are thus widely used in a range of fields. As the ninth most-abundant element (0.63%) in earth crust, the storage amount of titanium is rather rich, partially leading to the low-cost of TiO_2 and TiO_2-based materials for their large-scale applications. Furthermore, nontoxicity, relatively chemical stability and good biocompatibility also broadens their potential applications as additives of cosmetics, paints and other commercial products for teeth whitening or air purification *etc*. In the introduction section of this thesis, TiO_2 crystal structures, the application of TiO_2 and TiO_2-based materials, the defects in self-modified and co-doped TiO_2-based materials, the chemical synthesis methods and the associated physicochemical properties of co-doped TiO_2-based materials are briefly reviewed.

1.1 TiO_2 crystal structures

TiO_2 is a typical multiple polymorphic material with up to twelve different types of crystal structures. TiO_X (x=6, 7, 8, 9, 10) polyhedrons, which are used as the basic units to construct these different TiO_2 polymorphs and their related connection modes, are shown in **Figure 1**. Anatase, rutile and brookite are its three common phases and extensively reported to date since (1) they are easier and more mature to be synthesized at the experimental and industrial scales; and (2) they are more stable than other TiO_2 crystal structures at ambient conditions. Though the three normal TiO_2 phases are all composed of TiO_6 octahedrons (Figure 1a-1c), the connection mode of TiO_6 octahedrons slightly differs from one another. In anatase TiO_2 with space group symmetry $I4_1/amd$,[1] each TiO_6 octahedron shares four edges with the nearest ones, and forms zigzag chains along the ***a*** and ***b*** directions. Regarding rutile TiO_2 with space group symmetry $P4_2/mnm$,[2] each TiO_6 octahedron links together with another four basic units by sharing corners along ***a*** and ***b*** directions, and connects with another two by sharing edges along ***c*** direction. As to brookite TiO_2 with space group symmetry *Pbca*,[3] each TiO_6 octahedron shares three edges to form an orthorhombic structure. one of these connection modes determines the crystal arrangement of brookite TiO_2 along the ***a*** direction while the other two connection modes determine their arrangement along the ***c*** direction.

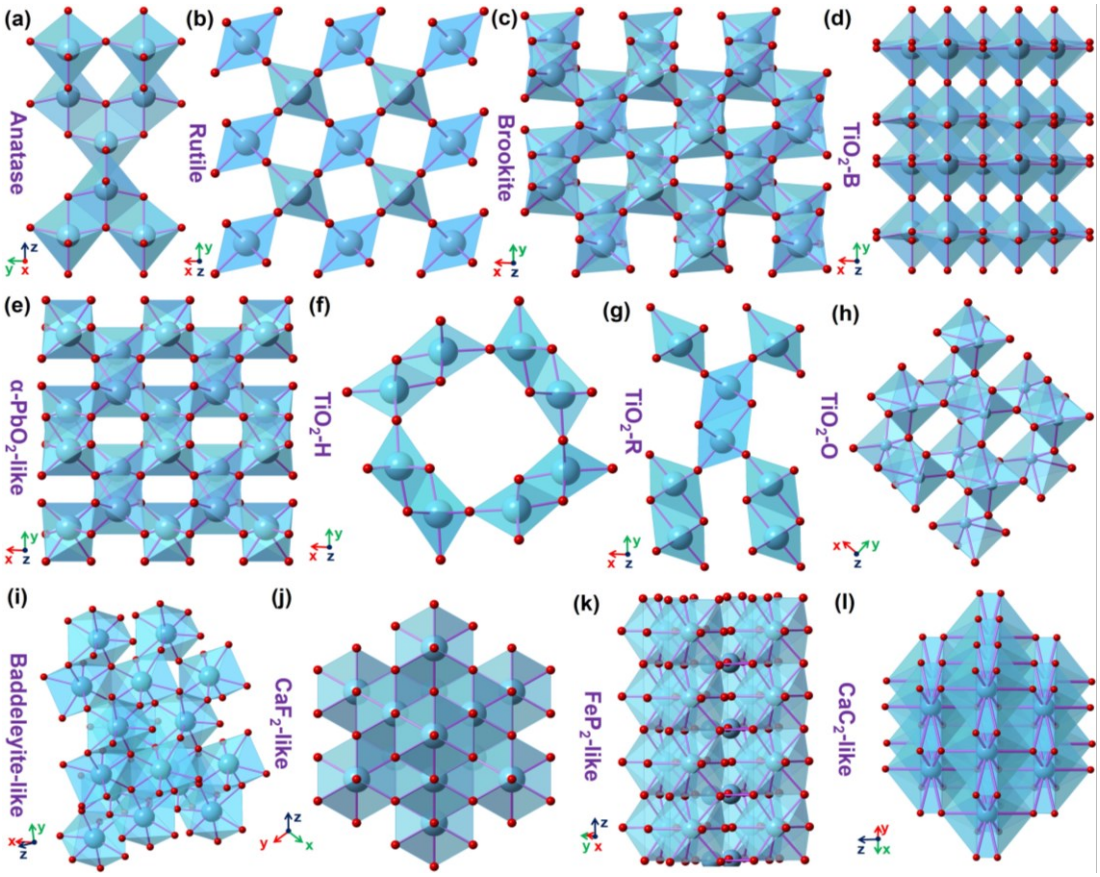

Figure 1. Polyhedral structures of different TiO_2 polymorphs: (a) anatase, (b) rutile, (c) brookite, (d) VO_2-like structure, (e) α-PbO_2-like structure, (f) hollandite-like structure, (g) ramsdellite-like structure, (h) orthorhombic structure, (i) baddeleyite-like structure, (j) CaF_2-like structure, (k) FeP_2-like structure, and (l) CaC_2-like structure.

TiO_6 octahedrons are also used to construct other TiO_2 crystal structures including VO_2-like (TiO_2-B), α-PbO_2-like, hollandite-like (TiO_2-H), ramsdellite-like (TiO_2-R) and TiO_2-O forms. However, the chemical synthesis of these crystal structures becomes more difficult and complicated than that of anatase, rutile or brookite phases. The reports on them are thus scare, and some of them are only predicted theoretically. In the framework structure of TiO_2-B with group space symmetry *C*2/*m*,[4] it is usually described as a stack of (011)-oriented sheets consisting of double layers of edge-sharing TiO_2 octahedrons. The sheets are connected through the corners of the facing octahedrons (note: it is also proposed that the environment of the corresponding Ti atom in a TiO_2-B phase is distorted square-pyramidal rather than octahedral.). In an α-PbO_2-like phase with space group symmetry *Pbcn*,[5] TiO_6 octahedrons form the planar chains sharing edges in a zigzag arrangement along the ***c*** direction. In the TiO_2-H crystal structure with space group symmetry *I*4/*m*,[6] it is composed of double chains of TiO_6 octahedrons by sharing edges (viewed along the ***c*** direction). Furthermore, it also shows 2x2 channels which are formed

along the [001] direction by corner cross-linking double chains. In a TiO_2-R form with space group symmetry *Pbnm*,[7] its basic framework is the TiO_6 double rutile chain. In the TiO_2-O crystal structure with space group symmetry *Pca*21,[8] the TiO_6 octahedrons are severely distorted and the Ti-O bonds present three different lengths.

In addition to these crystal structures composed of TiO_6 octahedrons, TiO_2 also possesses many other polymorphs in which Ti^{4+} ions have higher coordination numbers (*e.g.* 7, 8, 9 and 10). For instance, the baddeleyite-like TiO_2 phase with space group symmetry $P2_1/c$ is constructed by TiO_7 decahedra;[9] the CaF_2-like crystal structure with space group symmetry *Fm*-3*m* is composed of TiO_8 cubes;[10] the FeP_2-like structure is consisted by TiO_9 basic units,[11] and the CaC_2-type structure with space group symmetry *I*4/*mmm* adopts ten-fold coordinated TiO_{10} units by face-sharing dodecahedrons.[12] The ten coordination number is also currently known as the highest coordination number among all TiO_2 crystal structures. Such highly coordinated TiO_2 can only be synthesized under extremely high pressure conditions (above 690 GPa). Since TiO_2 has so many different crystal structures, it is normally taken as a model system to investigate the internal structure of earth by geologists. Future work on experimentally synthesizing or industrially manufacturing these highly-coordinated TiO_2 is necessary since they present ultra-high hardness, excellent conductivity or other abnormal physicochemical performances.

1.2 Application of TiO_2 and TiO_2-based materials

TiO_2 and TiO_2-based materials are now broadly used in optics, electrics, electronics, magnetics and other fields. **Figure 2** shows the main physicochemical properties and applications of TiO_2 and TiO_2-based materials. As the whitest pigment, intrinsic TiO_2 is normally added into paints or cosmetics to strengthen their whiteness. Elemental doping such as Fe, V or Ti^{3+} can make TiO_2-based materials show colour variation and thus important for colourful pigments.[13] Meanwhile, TiO_2 and TiO_2-based materials can also absorb ultraviolent light of solar spectrum and hence lower the damage of intense sunlight on human skins. Their absorbed photon energy can efficiently activate the separation of electron-hole pairs, and are then used to catalyse the decomposition of organic contaminates in water/air, the photo-degradation of plastic products or the splitting of water into hydrogen and oxygen gases.[14] TiO_2 and TiO_2-based materials are thus broadly used as ultraviolent- or visble-light photocatalysts in wastewater purification, air cleaning, and environmental remediation *etc*.

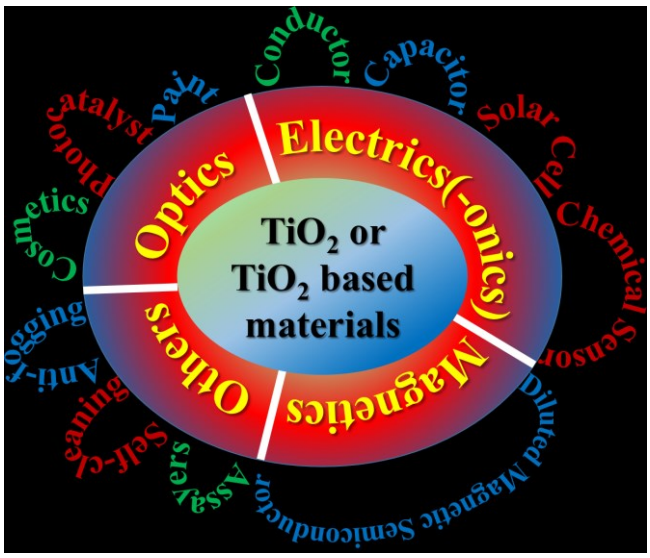

Figure 2. The major applications of TiO_2 and TiO_2-based materials.

TiO_2 and TiO_2-based materials are also widely applied in electrics or electronics. As a potential candidate of transparent conductive oxides, they can potentially replace the traditional ITO as a transparent electrode due to their low resistivity ($2x10^{-4}$ Ω•cm at room temperature) and high internal transmittance (95% in the visible light region).[15] In the assembling of solar cells like dye sensitive solar cells and hybrid organic-inorganic perovskite solar cells, they are normally used as the compact/mesoporous layers to separate electrons and holes.[16,17] In the sensors, they are normally used to detect gas molecules, soluble organics in water environment or biological substances *etc*.[18] Besides these applications, TiO_2-based materials also make a big progress in the application of capacitors because they simultaneously show colossal permittivity, relatively low dielectric loss and excellent temperature stability.[19] Their outstanding dielectric properties open up a new way to manufacture the future generation of single-layer or multi-layer ceramic capacitors.

In magnetics, TiO_2-based materials achieve extensive focus on the preparation of spintronic devices.[20] As a type of diluted magnetic semiconductors, both charge and spin degrees of freedom of carriers are used to store and transmit information. When some of transition metal ions (*e.g.* Fe, Co, Ni or Cu) are introduced into the crystal lattices of TiO_2 host materials, the diamagnetic or antiferromagnetic TiO_2 is transferred to be ferromagnetic. This magnetic transition is beneficial to offer lower power consumption and greater operating speed than the charge-based analogues.

In addition, TiO_2 and TiO_2-based materials are also broadly used in other fields such as anti-fogging and self-cleaning coating, high refractive index glasses (*e.g.* anatase: n≈2.56;

rutile: n≈2.61 and brookite: n≈2.58) and even the assay of some chemicals. For instance, ultrafast drying, antifogging as well as the self-cleaning of dirt or organic contaminates can be realized through controlling the superhydrophilicity or superhydrophobicity of TiO_2 or TiO_2-based material surfaces.[21,22]

1.3 Defects in TiO_2 and TiO_2-based materials

Perfect and stoichiometric TiO_2 materials almost do not exist naturally or even cannot be synthesized artificially. That is, TiO_2 and TiO_2-based materials must contain a certain type or level of defects. Some of these defects do not significantly affect their physicochemical properties and thus can be neglected. The others play critical roles depending on the concentration, the forms of introduced defects or the level of structural distortion.[23] It is commonly accepted that several properties of solid materials are controlled not so much by their geometric and electronic structure but by faults or defects in the crystal structures.[24] Through introducing different types, different forms and/or different concentrations of defects into TiO_2-based host materials, their local/average crystal structure can be tuned and thus their macroscopic performances can be changed by the intentional defect design and associated defect engineering. The introduced defect species, defect types or defect densities are directly related to the preparation procedures, synthesis methods, and the selection of extrinsic co-dopant or dopant ions.

1.3.1 Defects in self-modified TiO_2

Self-modifying means that TiO_2 materials are modified by the change of chemical valence, stoichiometric ratio, and atomic position of Ti and O other than by the introduction of additional elements. In the self-modified TiO_2 materials, intrinsic defects are rich and diverse depending on the concrete preparation conditions. They not only include point defects like oxygen vacancies, titanium interstitials, titanium vacancies and oxygen interstitials or reduced titanium (Ti^{3+}), but also include planar defects like shear planes.

1.3.1.1 Point defects in self-modified TiO_2

Oxygen vacancy is one of the most important defects, and it is also supposed to be one prevalent point defect in TiO_2. Oxygen vacancy in self-modified TiO_2 materials has been broadly investigated by both theoretical calculations and experimental characterizations.[25] It has been demonstrated that oxygen vacancies can behave as important adsorption and active sites for heterogeneous catalysis, which are able to strongly affect the reactivity of host TiO_2 materials. Once oxygen ions in TiO_2 crystal

structure are removed from their regular sites, oxygen vacancies will be left there. According to the chemical valences, oxygen vacancies can be categorized into doubly ($V_O^{\bullet\bullet}$), singly ($V_O^{\bullet}$) and neutral (V_O) ionized one, respectively.

Some experimental evidences are provided for the existence of oxygen vacancies with different chemical valences. For example, the results of infrared absorption spectroscopy point out that the energy level of doubly ionized $V_O^{\bullet\bullet}$ locates at about 1.18 eV below the conduction band edge while that of $V_O^{\bullet}$ is at about 0.75 eV.[26] It is in consistency with that of *Ab initio* density functional theory calculations.[23,27] Thermogravimetric analysis and electrical characterization further exhibit that the formation energy of $V_O^{\bullet\bullet}$ and $V_O^{\bullet}$ is 4.6 and (3.6-4.0) eV, respectively, though these values are slightly different depending on the reaction temperature and the partial pressure of oxygen gas.[28] For the neutral oxygen vacancies, the calculated formation energy is about 5.19-5.45 eV under extreme O-rich conditions and 1.42-1.65 eV under extreme Ti-rich conditions.[29] In addition, scanning tunnelling microscope (STM) images show some bright spots in the atomic column of oxygen[30] while photoluminance spectra present the enhancement of peak intensity and blue-shift of peak positions due to the formation of oxygen vacancies.[31]

Another dominant point defect in self-modified TiO_2 is Ti^{3+} ions. It is generated by the reduction of Ti^{4+} ions at a high temperature or under reduction conditions such as hydrogen, carbon monoxide gas and others. Ti^{3+} ions are thought as donor dopants to increase the conductivity of TiO_2 or act as reactive agents for many adsorbents. They are also believed to be the origin of blue coloration or "colour centre" of TiO_2. The formation of Ti^{3+} ions in TiO_2 is supported by several experimental evidences, (1) the g-tensor typical of a Ti $3d^1$ state measured by electronic paramagnetic resonance (EPR);[32] (2) the Ti^{3+} signal with the binding energy of ~457.7 eV detected by X-ray photoelectron spectroscopy (XPS);[33] and (3) a bandgap state of ~2 eV above the valence band (VB) maximum probed by ultraviolent photoemission spectroscopy (UPS), electron energy loss spectroscopy (EELS), or STM.[34-38] Though these techniques provide solid evidences for the existence of Ti^{3+} ions, it is still difficult to confirm their quantitate concentrations, their location in self-modified TiO_2 (bulk or surface), and their direct impacts on material properties.

In addition to oxygen vacancies and Ti^{3+} ions, there are also many other types of point defects such as titanium interstitials,[39] titanium vacancies,[40] and oxygen interstitials[41] *etc*. Due to only fewer studies on these defects, their experimental and theoretical evidences

should be further provided to demonstrate whether they indeed exist in TiO_2 materials. Moreover, these defects are usually formed at special conditions such as strict oxygen conditions or much longer reaction time. Their controllable synthesis is thus a difficulty. At most cases, the point defect species in TiO_2 is not single. Two or more types of point defects simultaneously exist in TiO_2 and thus lead to a complication in their analysis and characterization.

1.3.1.2 Shear planes in self-modified TiO_2

The appearance of crystallographic shear planes (*i.e.* magnéli phases) make the story of defects in self-modified TiO_2 materials more complicated. Crystallographic shear virtually displaces one slab of crystal with respect to a neighbouring slab, along a defined *(hkl)* plane, the shear plane, the displacement being defined by a shear vector, which approximates to a lattice vector of the parent structure when allowance is made for distortions in the fused octahedral groups.[42] The shear vector must have a component normal to the shear plane in order to give rise to a change in chemical composition. The shear vector lying wholly in the shear plane produces a stacking fault or antiphase boundary.[43] In a series of oxygen-deficient TiO_2 compounds, the normally observed shear plane is (12-1), but other shear planes also exist in samples, for example, (13-2).

Ab initio calculations point out that the defects' formation energies of magnéli phases is lower than that of isolated point defects. It is thus preferable to form a Magnéli phase at a particular concentration of oxygen deficiency.[44] These crystallographic shear planes are natural charge storage materials with a storage capacity that rivals the best known supercapacitors.[45] The experimental evidences of crystallographic shear planes are provided by electron microscopy, electron diffraction, direct lattice imaging, and X-ray diffraction *etc*.

1.3.2 Defects in co-doped TiO_2-based materials

The introduction of two or more extrinsic elements into TiO_2 crystal structures would form their co-doped TiO_2-based materials. According to the types of incorporated elements, co-doped TiO_2-based materials are categorized into three different types, that is, (1) metal+metal (M, M) ions co-doped TiO_2; (2) non-metal+non-metal (N_o, N_o) ions co-doped TiO_2; and (3) non-metal+metal (N_o, M) ions co-doped TiO_2. The dopant M ions are thought to substitute a proportion of Ti^{4+} or occupy the interstitial positions of TiO_2 crystal structures depending on their ionic radius and the synthesis condition of co-doped

TiO_2-based materials. The dopant N_o ions are designed to replace a proportion of O^{2-} ions, or they can also occupy the interstitial positions. The incorporated co-dopants can locally exist as isolated point defects, bind together to form defect pairs, or combine with other induced ions to form complicated defect clusters or inter-grown shear planes in the co-doped TiO_2-based materials. These different defect types are critical to determine the physicochemical properties of TiO_2-based materials. In the following, (N^{3-}, M^{5+}) and (M^{3+}, M^{5+}) co-doped TiO_2-based materials are taken as examples to further describe the formation of local defect structures, the used synthesis methods to introduce local defect states, as well as the effects of introduced defects on TiO_2-based material properties like visible light catalytic and colossal permittivity performances.

1.3.2.1 Defects in (N^{3-}, M^{5+}) co-doped TiO_2 for visible light catalysts

(N^{3-}, M^{5+}) co-doping (M=Nb, V, Ta and others) is an efficient strategy to activate the visible light catalytic (VLC) behaviour of TiO_2 materials for broad use in wastewater purification, air cleaning, hydrogen generation, and sterilization. It is thus significant to enhance the utilization efficiency of clean/renewable solar energy, and to alter the current state of environmental pollution. In (N^{3-}, M^{5+}) co-doped TiO_2-based materials, N^{3-} and M^{5+} ions are simultaneously incorporated into TiO_2 crystal structures by substituting a proportion of the Ti^{4+} and O^{2-} host ions. The atomic orbitals of these extrinsic co-dopant ions will hybridize with that of Ti^{4+}, O^{2-} or each other to extend the light absorption of TiO_2 towards the visible light regime, to reduce recombination of electron-hole pairs, and finally to enhance VLC efficiency. Furthermore, the coupling of N^{3-} and M^{5+} ions also increases the doping concentration of difficult-dopant N^{3-} ions.

The selected M^{5+} ions mainly include Nb^{5+}, Ta^{5+} and V^{5+} metal ions. In the atomic periodic table, niobium (Nb) is the 41st element with an electronegativity of 1.6 Pauling units and has the electronic configuration of $1s^22s^22p^63s^23p^63d^{10}4s^24p^64d^45s^1$. Nb ions normally have three chemical valences depending on the number of lost electrons in 4d and 5s orbitals, *i.e.*, Nb^{5+} (the ionic radius, r_{ion}=0.078 nm in six-coordinated octahedral), Nb^{4+} (r_{ion}=0.082 nm), and Nb^{3+} (r_{ion}=0.086 nm).[46]

Tantalum (Ta) is the 73rd element with an electronegativity of 1.5 Pauling units and has the electronic configuration of $1s^22s^22p^63s^23p^63d^{10}4s^24p^64d^{10}4f^{14}5s^25p^65d^36s^2$. Ta^{5+}, Ta^{4+} and Ta^{3+} are their three stable ions at normal conditions. The ionic radii of Ta ions are the same as that of Nb ions (r_{ion} of Ta^{5+}=0.078 nm; Ta^{4+}=0.082 nm; Ta^{3+}=0.086 nm). Vanadium (V) is the 43rd element with an electronegativity of 1.63 Pauling units and has

the electronic configuration of $1s^2 2s^2 2p^6 3s^2 3p^6 3d^3 4s^2$. The ionic radii of V ions are smaller than that of Ta or Nb ions, and are 0.068 (V^{5+}); 0.072 nm (V^{4+}); and 0.078 nm (V^{3+}), respectively.

Since Ta^{5+} and Nb^{5+} ions have almost the similar ionic radius as Ti^{4+} (r_{ion}=0.0745 nm) and their elements show the similar electronegativity as Ti (1.54), they are normally co-doped together with N^{3-} ions into host TiO_2 without producing a large distortion in the local/average crystal structures. The smaller V^{5+} ions are sometimes also used as co-dopants due to their easy substitution of Ti^{4+} ions.

Furthermore, M^{5+} dopant ions lose one additional electron in contrast to the Ti^{4+} host ions. This electron is well compensated by the co-doping of N^{3-} cations. The molar ratio of M^{5+} and N^{3-} co-dopants is thus expected to be 1:1 for charge balance. Any deviation of this stoichiometric ratio will generate extra Ti^{3+} ions or additional oxygen vacancies. In the two scenarios, (N^{3-}, M^{5+}) co-doping is actually accompanied by N^{3-} or M^{5+} mono-doping.

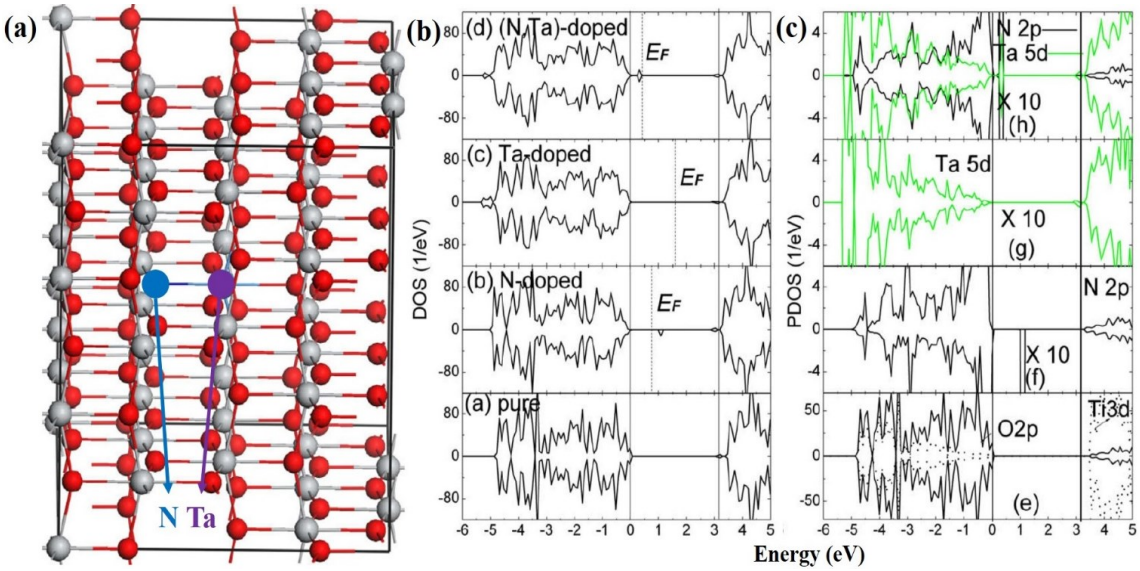

Figure 3. A 108-atom supercell containing substituted N and Ta co-dopants (a), the calculated total DOS (b) and PDOS (c) of un-doped, Ta mono-doped, N mono-doped and (N, Ta) co-doped anatase TiO_2.[67]

Theoretical calculations demonstrate that N and Ta co-dopants prefer to directly bind together in one octahedron among various co-doped configurations (**Figure 3**). An increase in the N-Ta distances will lead to a higher total formation energy. The hybridization of N2*p* and Ta5*d* states in (N, Ta) co-doped TiO_2 reduces recombination centres caused by impurity levels (Figure 3b and 3c), narrows the bandgap, increases carrier mobility, and finally enhances the VLC properties of (N, Ta) co-doped anatase

TiO_2 materials. The calculated bandgap value (2.7 eV) is also in consistency with the experimental results. The similar scenario also happens in (N, V) co-doped TiO_2. N and V will chemically bind together and narrow the bandgap by about 0.45 eV through providing an acceptor level of about 0.33 eV above the valence band and a donor level of about 0.12 eV below the conduction band. Moreover, the N and V have a large binding energy of about 0.77 eV, making them rather stable against separation, but the controlling of chemical valences of V^{5+} ions is too difficult technologically.

Various experimental routes have been tried to date to synthesize (N^{3-}, M^{5+}) co-doped TiO_2 materials. **Table 1** lists the detailed synthesis processes, the characterized material properties and the measured VLC effects. As seen, the used N sources are categorized into three different types: (1) the colourless liquid HNO_3 (nitric acid), NH_4OH (ammonia solution), $C_4H_{11}N$ (*n*-Butylamine), $C_6H_{15}N$ (triethylamine), and $C_6H_{15}NO_3$ (triethanolamine); (2) the solid CH_4N_2O (urea), $C_6H_{12}N_4$ (hexamethylenetetramine) and NH_4VO_3 (ammonium metavanadate), as well as (3) NH_3 (ammonia) or N_2 (nitrogen) gas. Meanwhile, the used M^{5+} sources include $NbCl_5$ (niobium pentachloride), $Nb(OCH_2CH_3)_5$ (niobium ethoxide), $(NH_4)[(NbOF_4)(NbF_7)_2$, $Ti_{1-x}Nb_x$ alloy, $TaCl_5$ (tantalum pentachloride), Ta metal, $(Ta_2O_5)_{0.01}(TiO_2)_{0.99}$ pellets, $TaC_{15}H_{35}O_5$ (tantalum isopropoxide), NH_4VO_3 (ammonium metavanadate) and others. The used Ti sources are mainly focused on $Ti(SO_4)_2$ (titanium sulphate), $TiCl_4$ (titanium tetrachloride), $C_{12}H_{28}O_4Ti$ (titanium isopropoxide, TTIP), $C_{16}H_{36}O_4Ti$ (titanium butoxide, $Ti(OBu)_4$), N mono-doped TiO_2, $Ti_{1-x}Nb_x$ alloy or Ti metal.

According to the difference in the selected raw materials, many synthesis methods have been tried to date to prepare (N^{3-}, M^{5+}) co-doped TiO_2 materials. The microwave-assisted hydrothermal or direct hydrothermal route are able to achieve (N^{3-}, M^{5+}) co-doped TiO_2 nanocrystals without any post-sintering process. In this reaction route, the raw materials containing Ti^{4+}, M^{5+} and N^{3-} ions were firstly dispersed in distilled water to form one solution. The prepared solution was then added into autoclaves to chemically react at the set temperature and reaction time. When the autoclaves cooled down to room temperatue, (N^{3-}, M^{5+}) co-doped TiO_2 product was finally achieved by separating them from the solution, washing and drying. This synthesis route is also easy to control the morphology and particle size of prepared (N^{3-}, M^{5+}) co-doped TiO_2 nanomaterials. Another widely used synthesis route is sol-gel and post-sintering treatment. At the so-gel stage, M^{5+} mono-doped or (N^{3-}, M^{5+}) co-doped amorphous TiO_2 or their hydroxides was prepared firstly. The subsequent post-sintering treatment at high temperature and N_2/NH_3

atmosphere not only induced the crystallization of mono-doped/co-doped TiO_2 but also further incorporated N^{3-} ions into M^{5+} mono-doped TiO_2. Though this method can also synthesize (N^{3-}, M^{5+}) co-doped TiO_2 nanomaterials, two adverse effects are also caused simultaneously, that is, (1) the serious agglomeration of nanoparticles at high temperature; and (2) the surface doping of N^{3-} ions due to their high temperature diffusion process. Furthermore, it is also not easy to experimentally control the doping ratios of N^{3-} and M^{5+} co-dopants.

In addition, other synthesis methods like magnetron sputtering, anodization, aerosol assisted chemical vapour deposition and others are also tried to prepared (N^{3-}, M^{5+}) co-doped TiO_2 films or nanotube arrays. These methods sometimes also need the post-sintering treatment to dope N^{3-} ions into the as-prepared M^{5-} mono-doped TiO_2 or require expensive sputtering instrument. The reports on these synthesis methods to prepare (N^{3-}, M^{5+}) co-doped TiO_2 materials are thus few in contrast to that of hydrothermal or sol-gel methods.

It can be further found from Table 1 that the normally achieved (N^{3-}, M^{5+}) co-doped TiO_2 materials show anatase and rutile crystal structures, but most of them are focused on co-doped anatase TiO_2. For example, in combination of solvothermal and post-sintering methods, (N^{3-}, Ta^{5+}) co-doped rutile TiO_2 nanowires/nanorods were prepared by firstly achieving Ta^{5+} mono-doped rutile TiO_2 nanowires/nanorods at the solvothermal reaction conditions and then further incorporating N^{3-} ions through high-temperature nitridation. The synthesis of co-doped rutile TiO_2 is more difficult than that of anatase one since it experimentally needs strong-acid or higher temperature conditions. On the other hand, the N^{3-} and M^{5+} co-dopants normally act as the inhibitor of phase transition from anatase to rutile and thus lead to a higher difficulty to synthesize (N^{3-}, M^{5+}) co-doped rutile TiO_2. Additionally, the loss of N^{3-} ions at high temperature also technologically restricts the formation of co-doped rutile crystal structure. The measured bandgap of prepared (N^{3-}, M^{5+}) co-doped TiO_2 ranges from 3.2 to 2.0 eV. Such a wide range is not only related to the used synthesis methods but also is related to "whether N^{3-} ions are really co-doped into TiO_2 with M^{5+} ions." At present, the assignment of "N^{3-} dopant ions in materials" is technologically difficult given the tiny difference of N XPS peaks from N^{5+} to N^{3-} ions and the N contamination on the nanomaterial surfaces. Furthermore, it is more difficult to distinguish "surface doping" or "bulk doping" just based on the characterization of XPS spectra since it can only detect the chemical information of material surface. It is thus understandable why many previous reports on (N^{3-}, M^{5+}) co-doped TiO_2 only present

Table 1. The synthesis processes, characterized properties and VLC effects for (N^{3-}, M^{5+}) co-doped TiO_2 materials (M=Nb, Ta and V).

Co-dopant	Synthesis				Characterization					VLC properties				
	N source	Nb source	Ti source	Method & condition	N (at.%)	Nb (at.%)	Phase	Bandgap (eV)	Shape	Light source	Dye (mg/L)	VLCs (g/L)	C/C_0, (%)	Ref
N^{3-}+Nb^{5+}	NH_4OH/ CH_4N_2O	$NbCl_5$	$Ti(SO_4)_2$	Microwave-assisted hydrothermal	15 (nominal)	10 (XPS)	Anatase	3.1	NP (~9 nm)	Halogen lamp (500 W, > 400 nm)	H_2O	0.4	100 umol/h	47
	$C_6H_{12}N_4$	$NbCl_5$	$TiCl_4$	Microwave-assisted hydrothermal (190 °C, 0.5 h)	-	2 (EDX)	Anatase	2.8	NP	LED lamps	NO (2ppm)	-	31%	48
	NH_3	$NbCl_5$	$C_{16}H_{36}O_4Ti$	Sol-gel & Post-sintering (500 °C, 5 h, NH_3)	-	1-33.3 (nominal)	Anatase	2.0	NP (20 nm)	Xe lamp (150 W, AM 1.5G filter)	MB (40)	-	7@120 min	49,50
	NH_3	$NbCl_5$	$C_{16}H_{36}O_4Ti$	Sol-gel & Post-sintering (500 °C, 5 h, NH_3)	0.2 (XPS)	25 (XPS)	Anatase	2.2	NP (20 nm)	Xe lamp (150 W, AM 1.5G filter)	H_2O	1	7umol/h	51
	NH_3	$Ti_{1-x}Nb_x$	$Ti_{1-x}Nb_x$	Anodization & Post-sintering (450 °C, 0.5 h,NH_3)	8.2 (XPS)	10 (nominal)	Anatase	2.8	NTA	Halogen lamp (3.0 mW/cm^2, > 400 nm)	MB (2)	-	12 @ 120 min	52
	NH_3	$(NH_4)[(NbOF_4)(NbF_7)_2]$	Ti foil	Anodization & Post-sintering (550 °C, 2 h, NH_3)	6.9 (XPS)	4 (bulk)	Anatase	-	NTA	Oriel EmArc (200 W)	-	-	-	53

	NH_4OH & HNO_3	$NbCl_5$	$C_{12}H_{28}O_4Ti$	Sol-gel & Post-sintering (400 °C, 3h, air)	-	0.5	Anatase	3.0	NP	Xe lamp (300 W, > 420 nm)	4-CP	1	0 @ 120 min	54
	$C_4H_{11}N$	$C_{10}H_{15}O_5Nb$	$C_{12}H_{28}O_4Ti$	Aerosol assisted chemical vapour deposition	0.06-0.09 (XPS)	2-10 (XPS)	Anatase	2.4-3.5	Films	-	-	-	-	55
	CH_4N_2O	$TaCl_5$	$C_{16}H_{36}O_4Ti$	Sol-gel & Post-sintering (500 °C, 1 h, air)	13.4 (XPS)	12.8 (XPS)	Anatase	2.7	NP	Xe lamp (500 W, > 420 nm)	MB (5)	1	32@240min	56
	NH_4OH	Ta	$C_{12}H_{28}O_4Ti$	Hydrothermal & Post-sintering (300 °C, 1 h, air)	1.7 (XPS)	0.29 (XPS)	Anatase	2.8	NP (20 nm)	Hg-Xe lamp (500 W, > 420 nm)	MB (5)	3	7@180min	57
N^{3-}+ Ta^{5+}	N_2	$(Ta_2O_5)_{0.01}(TiO_2)_{0.99}$	Ti & $(Ta_2O_5)_{0.01}$ $(TiO_2)_{0.99}$	Magnetron sputtering (400 °C)	0.5-0.6 (XPS)	2.3-1.3 (XPS)	Anatase	3.1-3.2	Film	Xe lamp (420 nm to 500 nm)	Oleic acid	-	11@120 min	58
	NH_3	$C_{15}H_{35}O_5Ta$	$TiCl_4$	Solvothermal & Post-sintering (500 °C, 2 h, NH_3)	-	0.29 (XPS)	Rutile	-	NW	visible light (>420 nm)	-	-	-	59
	NH_3	$C_{10}H_{25}O_5Ta$	$C_{12}H_{28}O_4Ti$	Microwave-assisted solvothermal & post-sintering (350 °C, 1 h, NH_3)	-	-	rutile	2.6	NR	Xe lamp (500 W, > 420 nm)	H_2O	0.5	0.7 umol/h	60

	$C_6H_{15}N$	NH_4VO_3	$C_{16}H_{36}O_4Ti$	Sol-gel & Post-sintering (450 °C, 2 h, air)	4 (nominal)	2 (nominal)	Anatase	2.3	NP (7nm)	Xe lamp (150 W, 15cm)	RhB (95.8)	0.29	0@60min	61
	$C_6H_{15}NO_3$	NH_4VO_3	$Ti(SO_4)_2$	Two-step hydrothermal (180 °C, 22h)	3.12 (XPS)	1.0 (ICP) 0.5(XPS)	Anatase	2.5	NP (13 nm)	Xe lamp (400 W, > 400 nm)	PCP-Na (20)	0.4	20@275 min	62
	$C_6H_{15}N$	V^{4+}	$C_{16}H_{36}O_4Ti$	Two-step hydrothermal (180 °C, 22h)	-	-	Anatase	2.8	NP (5 nm)	Xe lamp (400W, > 400 nm)	MB (1.6)	-	80@275 min	63
N^{3+}+V^{5+}														
	NH_4VO_3 or NH_3OH	NH_4VO_3	TiO_2 nanotubes	Hydrothermal (180 °C, 12 h)	2.97 (XPS)	20 (nominal)	Anatase	-	NP (11 nm)	Xe lamp (300W, > 420 nm)	MO (3.3)	-	54@300 min	64
	NH_4VO_3	NH_4VO_3	N-TiO_2	Hydrothermal (180 °C, 5 h)	3.4 (XPS)	4.2 (XPS)	Anatase	2.3	NTA	Hg lamp (300 W, > 420 nm)	CO_2	-	64.5 ppm/h·cm	65
	$C_6H_{15}N$	NH_4VO_3	$C_{16}H_{36}O_4Ti$	Sol-gel & Hydrothermal (180 °C, 20 h)	0.62 (XPS)	2 (nominal)	Anatase	2.5	NP	Halide lamp (400 W, 420nm)	CAP (25)	1	$325x10^{-4}$ min^{-1}	66

Note: in the Table 1, NP: nanoparticle; NTA: nanotube array; NW: nanowire; NR: nanorod; RhB: Rhodamine B; MB: methylene blue; 4-CP: 4-chlorophenol; MB: methylene blue; MO: methylene orange; PCP-Na: sodium pentachlorophenate; and CAP: chloramphenicol.

the nominal N^{3-} doping concentrations or even do not discuss it at all. However, the analysis of chemical compositions is fundamental to further investigate the material performances. The unbalanced ratio of N^{3-} and M^{5+} co-dopants tends to introduce the disadvantages of N^{3-} or M^{5+} mono-doping into TiO_2 materials and questions whether the observed light absorption behaviours or visible light catalytic effects are really related to $N^{3-}$and M^{5+} co-doping. Therefore, it is completely necessary to quantitatively analyse the chemical compositions of (N^{3-}, M^{5+}) co-doped TiO_2 through different technical instruments including TGA-DSC, N-O determinator, XPS and others in order to confirm that (1) the N^{3-} dopants are really co-doped into TiO_2 crystal structures with M^{5+} ions; (2) how many N^{3-} dopants exist in host TiO_2 materials; (3) whether N^{3-} and M^{5+} co-dopants are equal to avoid the adverse effects of their mono-doping; and (4) whether N^{3-} and M^{5+} co-dopants have been coupled together to significantly enhance visible light catalytic properties.

In contrast to (N^{3-}, Nb^{5+}) or (N^{3-}, Ta^{5+}) co-doping, it is found that V^{5+} and V^{4+} (V^{3+}) ions almost co-exist in all prepared (N^{3-}, V^{5+}) co-doped TiO_2. Though the real reasons for the easy change of chemical valences of V^{5+} ions are still not clear to date, V is not an appropriate dopant in the design and development of (N^{3-}, M^{5+}) co-doped TiO_2. By contrast, Nb^{5+} and Ta^{5+} dopants are chemically stable at almost all the reported synthesis conditions. They are thus appropriate M^{5+} ions for co-doping with N^{3-} ions.

The decomposition of dyes was characterized under visible light illumination to demonstrate the VLC efficiency of (N^{3-}, M^{5+}) co-doped TiO_2. The decomposition rate (C/C_0) changes a lot among different researcher groups. This is not only caused by the intrinsic features of prepared (N^{3-}, M^{5+}) co-doped TiO_2 materials but also is related to the detailed experimental setup or operation (*e.g.* the used light sources, the measured dye concentrations and types, the added VLC amount, the added concentrations of photocatalysts or dyes *etc.*). In addition to the decomposition of dyes using these (N^{3-}, M^{5+}) co-doped TiO_2 photocatalysts, water splitting experiments were also conducted occasionally. It is still hard to compare the photocatalytic efficiency of different VLCs prepared by different researchers for generating hydrogen. However, the generally accepted viewpoint is that (N^{3-}, M^{5+}) co-doping is more efficient in the enhancement of VLC properties in contrast to N^{3-} or M^{5+} mono-doping.

In summary, N^{3-} and M^{5+} co-dopants would bind together in their co-doped TiO_2 host materials. The introduction of N^{3-} and M^{5+} co-dopants into TiO_2 crystal structures are

critical to narrow the bandgap, remove the "trapping or recombination centres" of photo-generated carriers, increase the doping levels of N^{3-} ions, and thus enhance visible light catalytic properties. In contrast to Nb^{5+} and Ta^{5+} ions, the chemical valences of V^{5+} are too easy to change. It is thus better to select Nb^{5+} and Ta^{5+} as co-dopants of N^{3-} ions. Given that the difficulty in comparing the experimental results achieved by different research groups, the standard photocatalytic procedures and conditions should be proposed, and accurate chemical compositions should be determined by all researchers. Based on the overall considerations on the recent progress of (N^{3-}, M^{5+}) co-doped TiO_2 materials and the existed problems in the current research field of visible light catalysts, (N^{3-}, Nb^{5+}) co-doped TiO_2 nanocrystals are taken as an example and further investigated from the different aspects of local defect structure, chemical synthesis methods and associated visible light catalytic performances.

1.3.2.2 Defects in (M^{3+}, M^{5+}) co-doped TiO_2 for dielectric properties

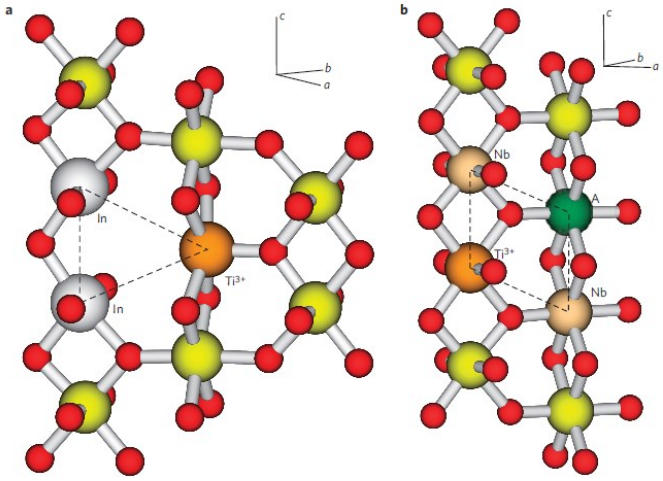

Figure 4. Structure of the In and Nb defect complexes. a,b, Ball-and-stick illustration of the triangular $2In^{3+}$-V_O-Ti^{3+} (a) and diamond $2Nb^{5+}$-Ti^{3+}-A_{Ti} (b) complexes common to stable (Nb +In) co-doped TiO_2. Unlabelled atoms are Ti^{4+} (yellow) and O (red). The triangle- and diamond- shaped motifs are sketched with dashed lines.[19]

Novel materials, which simultaneously possess colossal permittivity (CP), low dielectric loss (tanδ), excellent temperature- (T) and frequency- (F) stability, are ideal for the future development of modern microelectronics as well as the industrial manufacture of high-energy-density storage devices. Our previous work on (In^{3+}+Nb^{5+}) co-doped rutile TiO_2 ceramics not only provided a new type of materials with CP>10^4, loss tanδ<0.05 and nearly complete independence of T or F in the measurement range, but also proposed a new mechanism of electron-pinned defect dipoles to explain this abnormal dielectric behavior.[19]

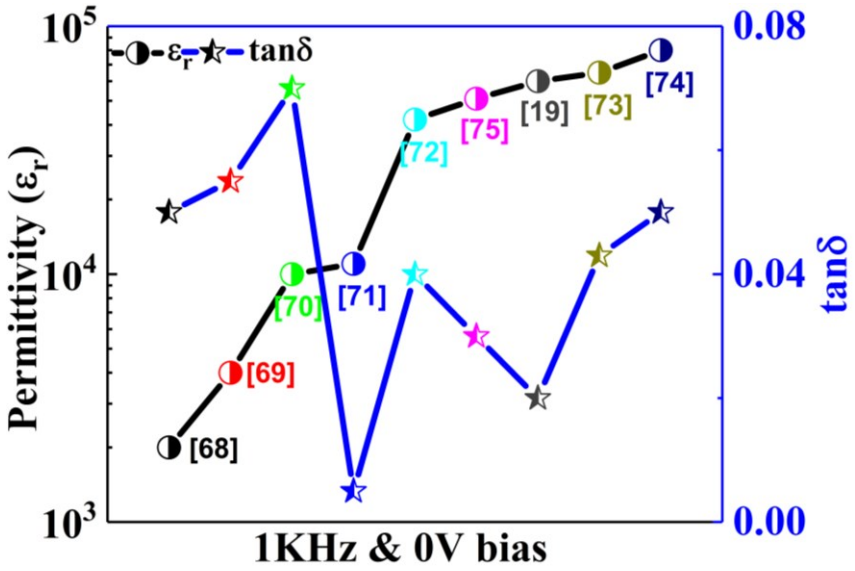

Figure 5, The reported dielectric properties of (In^{3+}+Nb^{5+}) co-doped rutile TiO_2 materials measured at 1kHz, room temperature and 0V bias in the references.[19, 68-75] It shows that dielectric constants and dielectric loss change broadly.

Figure 5 shows the experimental data of dielectric constant (ε_r) and dielectric loss of (In^{3+}+Nb^{5+}) co-doped rutile TiO_2 measured at 1 kHz, 0 V bias and room temperature conditions, summarized from the published references.[19, 68-75] It can be seen that the achieved ε_r covers from ~2000 to ~80000 while loss tanδ spans from ~0.005 to ~0.07. If the dielectric spectra in the measured frequency and temperature range are further compared, the discrepancy of ε_r or loss tanδ becomes more obvious among different research groups.

Due to the obvious difference in experimental results, various mechanisms, which include electron-pinned defect dipoles (EPDD), internal barrier layer capacitance (IBLC), surface barrier layer capacitance (SBLC) and others, are now proposed to explain their measured dielectric phenomena. The debate on the origin of CP in co-doped TiO_2 is still in progress and the intrinsic reasons why there are so large changes for dielectric properties is still unclear. Since creating the designated defect clusters in materials is highly sensitive to their compositions, the synthetic conditions and experimental process *etc.*, it is possible to introduce different defect species or defect structures into host TiO_2 and thus result in the change of dielectric properties/mechanisms. For example, just using smaller Al^{3+} ions to substitute the larger In^{3+} ions, the prepared (Al^{3+}+Nb^{5+}) co-doped rutile TiO_2 presents different macroscopic behaviours and local defect structures in contrast to (In^{3+}+Nb^{5+}) co-doping.[82] **Figure 6** shows the gradient distribution of chemical compositions (Ti^{3+} and O^{2-} ions) and the inter-grown, intermediate, metal ion rich structure formed in (Al^{3+}+Nb^{5+})

co-doped rutile TiO_2 ceramics. In addition, the presence of Ti^{3+} ions even in un-doped TiO_2 makes it more difficult to control their doping concentration experimentally. The additional Ti^{3+} ions will generate free electrons and lower the resistivity of co-doped rutile TiO_2-based materials. It is thus important to tune the technological parameters to really achieve the designed local defect structures.

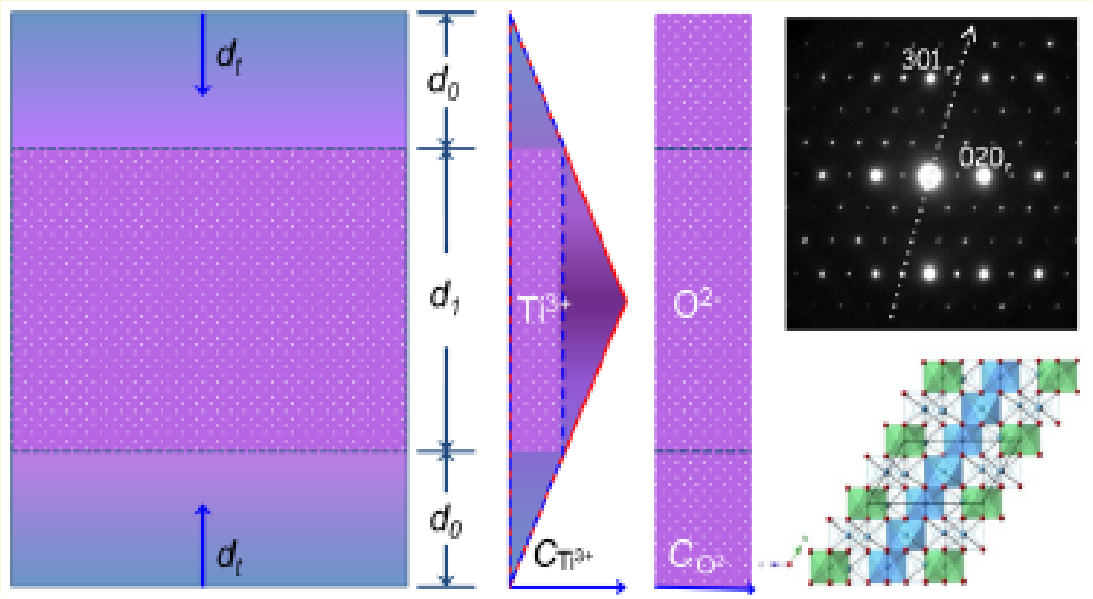

Figure 6, The gradient distribution of chemical compositions (Ti^{3+} and O^{2-} ions) and the inter-grown, intermediate, metal ion rich structure in (Al, Nb) co-doped rutile TiO_2 ceramics.[82]

Given that the electrode materials used in the fabrication of ceramic capacitors are normally composed of cheap metals like Ni, Al or related alloys, these cheap metals have lower melting point of below 1200 °C. However, the current sintering temperatures of (In^{3+}+Nb^{5+}) co-doped rutile TiO_2 ceramics are generally around 1400 °C. It also restricts the large-scale commercialization of this novel material in the preparation of single-/multi-layer ceramic capacitors. In order to lower the sintering temperature of (In^{3+}+Nb^{5+}) co-doped rutile TiO_2 ceramics, one efficient route is to directly use (In^{3+}+Nb^{5+}) co-doped TiO_2 nanocrystals as raw materials. Due to the size-effect of nanomaterials, the sintering temperature of (In^{3+}+Nb^{5+}) co-doped rutile TiO_2 ceramics is expected to be lowered below the melting point of electrode materials. To our best knowledge, there is no report on the synthesis of (In^{3+}+Nb^{5+}) co-doped TiO_2 nanocrystals. The difficulty perhaps lies in how to efficiently introduce so large In^{3+} ions into TiO_2 nanocrystals.

In summary, the introduction of M^{3+} and M^{5+} co-dopants into rutile TiO_2 can significantly change the dielectric properties of host TiO_2 materials due to the introduction of local

defect structures. Based on the potential and broad applications of (In^{3+}+Nb^{5+}) co-doped TiO_2 in the fabrication of ceramic capacitors, the development of their nanopowders is thus inevitable to further solve the difficulty in their commercialized manufacture. (In^{3+}+Nb^{5+}) co-doped anatase TiO_2 nanocrystals are thus synthesized in this thesis project. The local defect structure caused by In^{3+}, Nb^{5+} co-dopants, the resultant Ti^{3+} and V_O are investigated in the anatase crystal structure. Furthermore, the high-pressure reaction behaviour of these nanopowders are also studied by *in-situ* Raman spectroscopy.

1.4 Motivation and outline of the thesis

The topic of this dissertation is to develop multifunctional TiO_2-based nanocrystals for various realistic applications through local defect structure design in combination with the exploration of chemical synthesis methods and associated properties. Based on local defect structure design in materials, the physicochemical properties of TiO_2-based nanocrystals, for instance, their visible light catalytic properties, their dielectric properties, their high-pressure reaction behaviours and others are expected to be controllably tuned. As an efficient technological route to deliberately design local defect structures in TiO_2-based materials, ionic co-doping including cation-cation and cation-anion co-doping is investigated. The chemical synthesis methods used to introduce co-dopant ions into TiO_2 nanocrystals are mainly focused on solvothermal reaction in this thesis since (1) it can directly synthesize ions co-doped TiO_2 nanocrystals without any post-treatment process; (2) it can easily control the shape and particle size of achieved nanomaterials; (3) it can guarantee the homogeneous distribution and reaction of host and co-dopant ions in the whole reaction system. The ions co-doped TiO_2 nanocrystals synthesized thereof are then characterized by different measurement instruments including XRD, XPS, ICP-OES, SEM-EDS, (HR) TEM, Raman spectroscopy, abreacted-correction HADDF-STEM and others in order to show the intrinsic properties of the synthesized co-doped nanocrystals. Their photocatalytic properties, high-pressure reaction behaviours and dielectric properties are also investigated.

Firstly, the gradual exhaustion of non-renewable resources has motivated researchers to investigate a wide range of materials for the highly efficient utilization of clean and renewable solar energy. Among these materials, visible light catalysts (VLCs) are vital and ideal for photo-degradation, dye-sensitized solar cells, hydrogen generation from water as well as organic synthesis with the potential to convert more than ~45% of sunlight to chemical or electrical energy. As the third generation of photocatalysts, ions

co-doped TiO_2-based nanocrystals attract much research and industry interest. Based on local defect structure design, it is found that the simultaneous introduction of (N^{3-}, Nb^{5+}) ions into anatase TiO_2 crystal structures will locally form N^{3-}-Nb^{5+} defect pairs. These defect pairs can efficiently enhance visible light catalytic activation through narrowing the bandgap of TiO_2 and reducing the recombination centres of photo-excited carriers. Technologically, a solvothermal reaction route is designed to generate the expected N^{3-}-Nb^{5+} defect pairs in TiO_2 crystal structure. Experimental and theoretical investigations also demonstrate the emergent behaviour of locally forming defect-pair structure for the preparation of high-efficient visible light catalysts.

Secondly, anatase TiO_2 nanocrystals containing (N^{3-}, Ti^{3+}) ions are synthesized at the similar reaction conditions as that of (N^{3-}, Nb^{5+}) co-doped samples to further develop high-efficient visible light catalysts. It is found that the presence of Ti^{3+} ions can increase the doping levels of difficult-dopant N^{3-} ions. These two ions and resultant oxygen vacancies will integrate together to locally form Ti^{3+}-V_O-$2Ti^{4+}$-N^{3-} defect clusters in TiO_2 crystal structure. Due to the introduction of local defect clusters, one mid-gap energy level is newly generated in the TiO_2 bandgap and its location is determined by the associated defect structural models. These anatase TiO_2 nanocrystals modified by Ti^{3+}-V_O-$2Ti^{4+}$-N^{3-} defect clusters also shows a high efficiency for the decomposition of Rhodamine B under only visible light illumination condition.

Thirdly, (In^{3+}, Nb^{5+}) co-doped anatase TiO_2 nanocrystals are synthesized in order to solve the current difficulty of higher sintering temperature facing the preparation of TiO_2-based ceramic capacitors designed in terms of electron-pinned defect dipoles mechanism. Experimentally, the doping mechanisms of difficult-dopant In^{3+} ions and easy-dopant Nb^{5+} ions are investigated. It is found that the dual mechanisms of nucleation and diffusion doping are responsible for the synergistic incorporation of these two co-dopant ions. Theoretically, it is evidenced that the local defect structures created by the introduced In^{3+}, Nb^{5+} co-dopants, the resultant Ti^{3+} and $V_O^{\bullet\bullet}$ are composed of both $2In_{Ti}^{'}+V_O^{\bullet\bullet}+Ti_{Ti}^{'}+Nb_{Ti}^{\bullet}$ defect clusters and equivalent $Ti_{Ti}^{'}+Nb_{Ti}^{\bullet}$ defect pairs.

Finally, the high pressure reaction behaviour of the synthesized (In^{3+}, Nb^{5+}) co-doped anatase TiO_2 nanocrystals is investigated by *in situ* Raman spectroscopy. Due to the introduction of local defect-cluster and defect-pair structures, it is found that these co-doped anatase TiO_2 nanocrystals possess an abnormal trans-regime structural transition. Through the high pressure reaction, the baddeleyite- and α-PbO_2-like metastable

polymorphic phases of TiO_2 materials are synthesized thereof. In addition, these small nanocrystals are demonstrated to enable lowering the sintering temperature of related ceramics to about 1100 °C and thus conquers the technological bottleneck facing the preparation of ceramic capacitors using this type of material.

This thesis is composed of the following chapters:

Chapter 1 is an introduction to the relevant background information of this thesis.

Chapter 2 is a summary of the used experimental and characterization methods of this thesis.

Chapter 3 shows the major publications from this thesis including 5 peer-reviewed journal articles. Additional data used for the supporting information of these publications have also been attached to related papers.

Chapter 4 summarizes the main achievements during the PhD research project and prospects the potential continuing work for future investigations.

Chapter 5 lists the publications, patents and conference presentations.

References

[1] M. Horn, C. F. Schwerdtfeger and E. P. Meagher. Refinement of the structure of anatase at several temperatures. Zeitschrift für Kristallographie Crystalline Materials (1972), *136*, S273-281.

[2] C. E. Ekuma and D. Bagayoko. Ab-initio electronic and structural properties of rutile titanium dioxide. Japanese Journal of Applied Physics (2011), *50*, 101103.

[3] E. P. Meagher and G. A. Lager. Polyhedral thermal expansion in the TiO_2 polymorphs. Refinement of the crystal structures of rutile and brookite at high temperature. Canadian Mineralogist (1979), *17*, 77-85.

[4] T. P. Feist and P. K. Davies. The soft chemical synthesis of TiO_2 (B) from layered titanates. Journal of Solid State Chemistry (1992), *101*, 275-295.

[5] S. K. Filatov, N. A. Bendeliani, B. Albert, J. Kopf, T. I. Dyuzheva and L. M. Lityagina. Crystalline structure of the (TiO_2)-II high-pressure phase at 293, 223 and 133 K according to single-crystal X-ray diffraction data. Doklady Physics (2007), *52*, 195-199.

[6] M. Latroche, L. Brohan, R. Marchand and M. Tournoux. New hollandite oxides: TiO_2 and $K_{0.06}TiO_2$. Journal of solid state chemistry (1989), *81*, 78-82.

[7] H. Zhang and J. F. Banfield. Structural characteristics and mechanical and thermodynamic properties of nanocrystalline TiO_2. Chemical Reviews (2014), *114*, 9613-9644.

[8] Z. Fu, Y. Liang, S. Wang and Z. Zhong. Structural phase transition and mechanical properties of TiO_2 under high pressure. Physica Status Solidi B (2013), *250*, 2206-2214.

[9] H. Sato, S. Endo, M. Sugiyama, T. Kikegawa, O. Shimomura and K. Kusaba. Baddeleyite-type high-pressure phase of TiO_2. Science (1991), *251*, 4995.

[10] M. Mattesini, J. S. Almeida, L. Dubrovinsky, N. Dubrovinskaia, B. Johansson and R. Ahuja. Physical Review B (2004), *70*, 212101.

[11] H. Dekura, T. Tsuchiya, Y. Kuwayama and J. Tsuchiya. Physical Review Letters (2011), *107*, 045701.

[12] X. Zhong, J. Wang, S. Zhang, G. Yang and Y. Wang. Ten-fold coordinated polymorph and metallization of TiO_2 under high pressure. RSC Advance (2015), *5*, 54253.

[13] J. Večeřa, I. Šedová, P. Mikulášek and P. Šulcová. Synthesis and Characterization of Rutile Pigments with Cr and Nb. Journal of Inorganic Chemistry (2014), *2014*, 705493.

[14] J. Schneider, M. Matsuoka, M. Takeuchi, J. Zhang, Y. Horiuchi, M. Anpo and D. W. Bahnemann. Understanding TiO_2 photocatalysis: mechanisms and materials. Chemical Reviews (2014), *114*, 9919-9986.

[15] Y. Furubayashi, T. Hitosugi, Y. Yamamoto, K. Inaba, G. Kinoda, Y. Hirose, T. Shimada and T. Hasegawa. Applied Physics Letters (2005), *86*, 252101.

[16] U. Bach, D. Lupo, P. Comte, J. E. Moser, F.Weissörtel, J. Salbeck, H. Spreitzer and M. Grätzel. Solid-state dye-sensitized mesoporous TiO_2 solar cells with high photon-to-electron conversion efficiencies. Nature (1998), *395*, 583-585.

[17] B. Roose, S. Pathak and U. Steiner. Doping of TiO_2 for sensitized solar cells. Chemical Society Reviews (2015), *44*, 8326-8349.

[18] J. Bai and B. Zhou. Titanium dioxide nanomaterials for sensor applications. Chemical Reviews (2014), *114*, 10131-10176.

[19] W. Hu, Y. Liu, R. L. Withers, T. J. Frankcombe, L. Norén, A. Snashall, M. Kitchin, P. Smith, B. Gong, H. Chen, F. Brink, J. Schiemer and J. Wong-Leung. Nature Materials (2013), *12*, 821.

[20] Y. Matsumoto, M. Murakami, T. Shono, T. Hasegawa, T. Fukumura, M. Kawasaki, P. Ahmet, T. Chikyow, S.-Y. Koshihara and H. Koinuma. Room-temperature ferromagnetism in transparent transition metal-doped titanium dioxide. Science (2001), 291, 854-856.

[21] R. Wang, K. Hashimoto, A. Fujishima, M. Chikuni, E. Kojima, A. Kitamura, M. Shimohigoshi and T. Watanabe. Light-induced amphiphilic surfaces. Nature (1997), *388*, 431-432.

[22] L. Zhang, N. Zhao and J. Xu. Fabrication and application of superhydrophilic surfaces: a review. Journal of Adhesion Science and Technology (2014), 28, 769-790.

[23] F. M. Hossain, G. E. Murch, L. Sheppard and J. Nowotny. The effect of defect disorder on the electronic structure of rutile TiO_{2-x}. Defect and Diffusion Forum (2006), *251-252*, 1-12.

[24] G. Pacchioni. Oxygen vacancy: the invisible agent on oxide surfaces. ChemPhysChem (2003), *4*, 1041-1047.

[25] X. Pan, M. -Q. Yang, X. Fu, N. Zhang and Y. -J. Xu. Defective TiO_2 with oxygen vacancies: synthesis, properties and photocatalytic applications. Nanoscale (2013), 5, 3601-3614.

[26] D. C. Cronemeyer. Infrared absorption of reduced rutile TiO_2 single crystals. Physical Reviews (1959), *113*, 1222.

[27] M. K. Nowotny, L. R. Sheppard, T. Bak and J. Nowotny. Defect chemistry of titanium dioxide. application of defect engineering in processing of TiO_2-based photocatalysts. The Journal of Physical Chemistry C (2008), *112*, 5275-5300.

[28] J. -F. Marucco, J. Gautron and P. Lemasson. Thermogravimetric and electrical study of non-stoichiometric titanium dioxide TiO_{2-x} between 800 and 1100 °C. Journal of Physics and Chemistry of Solids (1981), 42, 363-367.

[29] P. Déak, B. Aradi and T. Frauenheim. Quantitative theory of the oxygen vacancy and carrier self-trapping in bulk TiO_2. Physical Review B (2012), 86, 195206.

[30] M. Setvín, U. Aschauer, P. Scheiber, Y. -F. Li, W. Hou, M. Schmid, A. Selloni and U. Diebold. Reaction of O_2 with subsurface oxygen vacancies on TiO_2 anatase (101). Science (2013), *341*, 988-991.

[31] C. Mercado, Z. Seeley, A. Bandyopadhyay, S. Bose and J. L. McHale. Photoluminescence of dense nanocrystalline titanium dioxide thin films: effect of doping and thickness and relation to gas sensing. ACS Applied Materials & Interfaces (2011), *3*, 2281-2288.

[32] P. F. Chester. Electron spin resonance in semiconducting rutile. Journal of Applied Physics (1961), *32*, 2233.

[33] L. -B. Xiong, J. -L. Li, B. Yang and Y. Yu. Ti^{3+} in the surface of titanium dioxide: generation, properties and photocatalytic application. Journal of Nanomaterials (2012), *2012*, 831524.

[34] V. E. Henrich, G. Dresselhaus and H. J. Zeiger. Observation of two-dimensional phases associated with defect states on the surface of TiO_2. Physical Review Letters (1976), *36*, 1335.

[35] R. L. Kurtz, R. Stock-Bauer, T. E. Madey, E. Román and J. L. D. Segovia. Synchrotron radiation studies of H_2O adsorption on TiO_2 (110). Surface Science (1989), *218*, 178-200.

[36] M. Nolan, S. D. Elliot, J. S. Mulley, R. A. Bennet, M. Basham and P. Mulheran. Electronic structure of point defects in controlled self-doping of the TiO_2 (110) surface: combined photoemission spectroscopy and density functional theory study. Physical Review B (2008), *77*, 235424.

[37] M. A. Henderson, W. S. Epling, C. H. F. Peden and C. L. Perkins. Insights into photoexcited electron scavenging processes on TiO_2 obtained from studies of the reaction of O_2 with OH groups adsorbed at electronic defects on TiO_2 (110). The Journal of Physical Chemistry B (2003), *107*, 534-545.

[38] S. Wendt, P. T. Sprunger, E. Lira, G. K. H. Madsen, Z. Li, J. Ø. Hansen, J. Matthiensen, A. Blekinge-Rasmussen, E. Lægsgaard, B. Hammer and F. Besenbacher. The role of interstitial sites in the Ti3*d* defect state in the band gap of titania. Science (2008), *320*, 1755-1759.

[39] T. Tanaka, A. Sumiya, H. Sawada, Y. Kondo and K. Takayanagi. Direct observation of interstitial titanium ions in TiO_2 substrate with gold nanoparticle. Surface Science (2014), *619*, 39-43.

[40] M. K. Nowotny, T. Bak, J. Nowotny and C. C. Sorrell. Titanium vacancies in nonstoichiometric TiO_2 single crystal. Physica Status Solidi B (2005), *242*, R88-R90.

[41] H. Kamisaka and K. Yamashita. Theoretical study of the interstitial oxygen atom in anatase and rutile TiO_2: electron trapping and elongation of the $r_{(O\text{-}O)}$ bond. The Journal of Physical Chemistry C (2011), *115*, 8265-8273.

[42] J. S. Anderson and R. J. Tilley. Crystallographic Shear in oxygen-deficient rutile: an electron microscope study. Journal of Solid State Chemistry. (1970), *2*, 472-482.

[43] J. S. Anderson and B. G. Hyde. On the possible role of dislocations in generating ordered and disordered shear structures. Journal of Physics and Chemistry of Solids (1967), *28*, 1393.

[44] L. Liborio and N. Harrison. Thermodynamics of oxygen defective Magnéli phases in rutile: A first-principles study. Physical Review B (2008), *77*, 104104.

[45] A. C. M. Padilha1, H. Raebiger, A. R. Rocha and G. M. Dalpian. Charge storage in oxygen deficient phases of TiO_2: defect Physics without defects. Scientific Reports (2016), *6*, 28871.

[46] The ionic radius and electronegativity of Nb, Ta and V elements and ions can be found from the below website of https://www.webelements.com.

[47] H.-Y. Lin and C.-Y. Shih. Efficient one-pot microwave-assisted hydrothermal synthesis of M (M = Cr, Ni, Cu, Nb) and nitrogen co-doped TiO_2 for hydrogen production by photocatalytic water splitting. Journal of Molecular Catalysis A: Chemical (2016), *411*, 128-137.

[48] P. Zhang, S. Yin, T. Sekino, S.W. Lee and T. Sato. Nb and N co-doped TiO_2 for a high-performance de NOx photocatalyst under visible LED light irradiation. Research on Chemical Intermediates (2013) *39*, 1509-1515.

[49] T. M. Breault and B. M. Bartlett. Lowering the band gap of anatase-structured TiO_2 by coalloying with Nb and N: electronic structure and photocatalytic degradation of methylene blue dye. The Journal of Physical Chemistry C (2012), *116*, 5986-5994.

[50] T. M. Breault and B. M. Bartlett. Composition dependence of TiO_2:$(Nb,N)_x$ compounds on the rate of photocatalytic methylene blue dye degradation. The Journal of Physical Chemistry C (2013), *117*, 8611-8618.

[51] T. M. Breault, J. J. Brancho, P. Guo and B. M. Bartlett. Visible light water oxidation using a co-catalyst loaded anatase-structured $Ti_{1-(5x/4)}Nb_xO_{2-y-\delta}N_y$ compound. Inorganic Chemistry (2013), *52*, 9363-9368.

[52] Z. Xu, W. Yang, Q. Li, S. Gao and J. K. Shang. Passivated n–p co-doping of niobium and nitrogen into self-organized TiO_2 nanotube arrays for enhanced visible light photocatalytic performance. Applied Catalysis B (2014), *144*, 343-352.

[53] T. Cottineau, N. Béalu, P.-A. Gross, S. N. Pronkin, N. Keller, E. R. Savinova and V. Keller. One step synthesis of niobium doped titania nanotube arrays to form (N, Nb) co-doped TiO_2 with high visible light photoelectrochemical activity. Journal of Materials Chemistry A (2013), *1*, 2151-2160.

[54] J. Lim, P. Murugan, N. Lakshminarasimhan, J. Y. Kim, J. S. Lee, S.-H. Lee and W. Choi. Synergic photocatalytic effects of nitrogen and niobium co-doping in TiO_2 for the redox conversion of aquatic pollutants under visible light. Journal of Catalysis (2014), *310*, 91-99.

[55] N. P. Chadwick, E. N. K. Glover, S. Sathasivam, S. N. Basahel, S. A. Althabaiti, A. O. Alyoubi, I. P. Parkina and C. J. Carmalt. Photo-activity and low resistivity in N/Nb

codoped TiO_2 thin films by combinatorial AACVD. Journal of Materials Chemistry A (2016), *4*, 407-415.

[56] Y. F. Zhao, C. Li, J. Y. Hu, Y. Y. Gong, L. Y. Niu and X. J. Liu. Ta and N modulated electronic, optical and photocatalytic properties of TiO_2. Physics Letters A (2016), *380*, 910-916.

[57] N. T. H. Le, T. D. Thanh, V.-T. Pham, T. L. Phan, V. D. Lam, D. H. Manh, T. X. Anh, T. K. C. Le, N. Thammajak, L. V. Hong and S. C. Yu. Structure and high photocatalytic activity of (N, Ta)-doped TiO_2 nanoparticles. Journal of Applied Physics (2016), *120*, 142110.

[58] K. Obata, H. Irie and K. Hashimoto. Enhanced photocatalytic activities of Ta, N co-doped TiO_2 thin films under visible light. Chemical Physics (2007), *339*, 124-132.

[59] S. Hoang, S. Guo and C. B. Mullins. Coincorporation of N and Ta into TiO_2 nanowires for visible light driven photoelectrochemical water oxidation. The Journal of Physical Chemistry C (2012), *116*, 23283-23290.

[60] A. Nakada, S. Nishioka, J. J. M. Vequizo, K. Muraoka, T. Kanazawa, A. Yamakata, S. Nozawa, H. Kumagai, S.-I. Adachi, O. Ishitani and K. Maeda. Solar-driven Z-scheme water splitting using tantalum/nitrogen co-doped rutile titania nanorod as an oxygen evolution photocatalyst. Journal of Materials Chemistry A (2017), DOI: 10.1039/c6ta10541f.

[61] R. Jaiswal, N. Patel, D. C. Kothari and A. Miotello. Improved visible light photocatalytic activity of TiO_2 co-doped with vanadium and nitrogen. Applied Catalysis B (2012), *126*, 47-54.

[62] J. Liu, R. Han, Y. Zhao, H. Wang, W. Lu, T. Yu and Y. Zhang. Enhanced photoactivity of V-N codoped TiO_2 derived from a two-step hydrothermal procedure for the degradation of PCP-Na under visible light irradiation. The Journal of Physical Chemistry C (2011), *115*, 4507-4515.

[63] D.-E. Gu, B.-C. Yang and Y.-D. Hu. V and N co-doped nanocrystal anatase TiO_2 photocatalysts with enhanced photocatalytic activity under visible light irradiation. Catalysis Communications (2008), *9*, 1472-1476.

[64] J. Zhong, J. Xu and Q. Wang. Nitrogen and vanadium co-doped TiO_2 mesosponge layers for enhancement in visible photocatalytic activity. Applied Surface Science (2014), *315*, 131-137.

[65] D. Lu, M. Zhang, Z. Zhang, Q. Li, X. Wang and J. Yang. Self-organized vanadium and nitrogen co-doped titania nanotube arrays with enhanced photocatalytic reduction of CO_2 into CH_4. Nanoscale Research Letters (2014), *9*, 272.

[66] N. K. Eswar, P. C. Ramamurthy and G. Madras. Novel synergistic photocatalytic degradation of antibiotics and bacteria using V-N doped TiO_2 under visible light: the state of nitrogen in V-doped TiO_2. New Journal of Chemistry (2016), *40*, 3464-3475.

[67] R. Long and N. J. English. Band gap engineering of (N, Ta)-codoped TiO_2: a first-principles calculation. Chemical Physics Letters (2009), *478*, 175-179.

[68] X.-G. Zhao, P. Liu, Y.-C. Song, A.-P. Zhang, X.-M. Chen and J.-P. Zhou. Origin of colossal permittivity in $(In_{1/2}Nb_{1/2})TiO_2$ via broadband dielectric spectroscopy. Physical Chemistry Chemical Physics (2015), *17*, 23132-23139.

[69] Z. Gai, Z. Cheng, X. Wang, L. Zhao, N. Yin, R. Abah, M. Zhao, F. Hong, Z. Yu and S. Dou. A colossal dielectric constant of an amorphous TiO_2: (Nb, In) film with low loss fabrication at room temperature. Journal of Materials Chemistry C (2014), *2*, 6790-6795.

[70] H. Han, P. Dufour, S. Mhin, J. H. Ryu, C. Tenailleau and S. Guillemet-Fritsch. Quasi-intrinsic colossal permittivity in Nb and In co-doped rutile TiO_2 nanoceramics synthesized through a oxalate chemical-solution route combined with spark plasma sintering. Physical Chemistry Chemical Physics (2015), *17*, 16864-16875.

[71] Y. Q. Wu, X. Zhao, J. L. Zhang, W. B. Su and J. Liu. Huge low-frequency dielectric response of (Nb,In)-doped TiO_2 ceramics. Applied Physics Letters (2015), *107*, 242904.

[72] J. Li, F. Li, C. Li, G. Yang, Z. Xu and S. Zhang. Evidences of grain boundary capacitance effect on the colossal dielectric permittivity in (Nb+ In) co-doped TiO_2 ceramics. Scientific Report (2015), *5*, 8295.

[73] J. Li, F. Li, Y. Zhuang, L. Jin, L. Wang, X. Wei, Z. Xu and S. J. Zhang. Microstructure and dielectric properties of (Nb + In) co-doped rutile TiO_2 ceramics. Journal of Applied Physics (2014), *116*, 074105.

[74] J. Li, F. Li, Z. Xu, G. Yang and S. Zhang. Nonlinear *I-V* behavior in colossal permittivity ceramics: (Nb+ In) co-doped rutile TiO_2.Ceramics International (2015), *41*, S798-S803.

[75] W. Tuichai, S. Danwittayakul, S. Maensiri and P. Thongbai. Investigation on temperature stability performance of giant permittivity (In+Nb) in co-doped TiO_2 ceramic: a crucial aspect for practical electronic applications. RSC Advance (2016), *6*, 5582-5589.

[76] K. Th. Fehr, A. Günther, R. Hochleitner and E. Schmidbauer. Electrical properties of rutile-type $In(Al)_{0.025}Nb_{0.025}Ti_{0.95}O_2$ ceramics. Journal of Electroceramics (2014), *33*, 163-171.

[77] Z. Li, J. Wu, D. Xiao, J. Zhu and W. Wu. Colossal permittivity in titanium dioxide ceramics modified by tantalum and trivalent elements. Acta Materialia (2016), *103*, 243-251.

[78] X. Cheng, Z. Li and J. Wu. Colossal permittivity in ceramics of TiO_2 co-doped with niobium and trivalent cation. Journal of Materials Chemistry A (2015), *3*, 5805-5810.

[79] W. Dong, W. Hu, A. Berlie, K. Lau, H. Chen, R. L. Withers and Y. Liu. Colossal dielectric behavior of Ga+Nb co-doped rutile TiO_2. ACS Applied Materials & Interfaces (2015), *7,* 25321-25325.

[80] Z. Li, J. Wu and W. Wu. Composition dependence of colossal permittivity in $(Sm_{0.5}Ta_{0.5})_xTi_{1-x}O_2$ ceramics. Journal of Materials Chemistry C (2015), *3,* 9206-9216.

[81] W. Tuichai, P. Srepusharawoot, E. Swatsitang, S. Danwittayakul and P. Thongbai. Giant dielectric permittivity and electronic structure in (Al + Sb) co-doped TiO_2 ceramics. Microelectronic Engineering (2015), *146*, 32-37.

[82] W. Hu, K. Lau, Y. Liu, R. L. Withers, H. Chen, L. Fu, B. Gong and W. Hutchison. Colossal Dielectric Permittivity in (Nb+Al) Codoped Rutile TiO_2 Ceramics: Compositional Gradient and Local Structure. Chemistry of Materials (2015), *27*, 4934-4942.

[83] A. Wen, D. Yuan, X. Zhu, J. Zhu, D. Xiao and J. Zhu. Electrical and dielectric properties of aluminum/niobium co-doped $CaCu_3Ti_4O_{12}$ Ceramics. Ferroelectrics (2016), *492,* 1-9.

[84] Z. Wang, M. Cao, Q. Zhang, H. Hao, Z. Yao, Z. Wang, Z. Song, Y. Zhang, W. Hu and H. Liu. Dielectric relaxation in Zr-doped $SrTiO_3$ ceramics sintered in N_2 with giant permittivity and low dielectric loss. Journal of the American Ceramic Society (2015), *98,* 476-482.

Chapter 2. Experiment and Characterization

2.1 Chemicals

Chemicals used in this thesis project are overviewed and listed in **Table 2**. The selected titanium source is liquid titanium tetrachloride ($TiCl_4$) with the molar mass (*M*) of 189.7 g/mol. Niobium(V) chloride ($NbCl_5$, *M*=270.2 g/mol) is mainly used as one niobium source. Since the two chemicals are very sensitive to humidity, their operation is proposed in a N_2 glove box or through a Schlenk line. Indium(III) nitrate [$In(NO_3)_3$, *M*=300.8 g/mol] and indium(III) acetate [$In(C_2H_3O_2)_3$, *M*=292.0 g/mol] are used as the indium source. Nitric acid (HNO_3, *M*=63.0 g/mol) and ammonia water (NH_4OH, *M*=35.0 g/mol) are respectively used as the nitrogen source. The used solvent is mainly focused on ethanol. According to the chemical compositions of co-doped materials, different volumes/weights of chemicals are added experimentally.

Table 2. The detailed information of chemicals used in this thesis project including their chemical formula, CAS number, molar mass, states and producers.

Reactants	Chemical Formula	CAS number	Molar mass (g/mol)	States	Producers
Ethanol	CH_3CH_2OH	64-17-5	46.1	Liquid	EMD Millipore Corporation
Titanium tetrachloride	$TiCl_4$	7550-45-0	189.7	Liquid	Sigma-Aldrich
Indium(III) nitrate	$In(NO_3)_3$	207398-97-8	300.8	Solid	Alfa Aesar
Indium(III) acetate	$In(C_2H_3O_2)_3$	25114-58-3	292.0	Solid	Alfa Aesar
Niobium(V) chloride	$NbCl_5$	10026-12-7	270.2	Solid	Alfa Aesar
Nitric Acid	HNO_3	7697-37-2	63.0	Liquid	Ajax Finechem Pty Ltd
Ammonia Water	NH_4OH	1336-21-6	35.0	Liquid	APS Finechem

2.2 Synthesis process

A solvothermal reaction route is designed to synthesize ions [*e.g.* (In^{3+}, Nb^{5+}), (N^{3-}, Nb^{5+}) and (N^{3-}, Ti^{3+})] co-doped anatase TiO_2 nanocrystals. The experimental flowing chart is presented in **Figure 7**. It is mainly categorized into three steps: (1) the homogeneous mixing of used chemicals in ethanol solvent to form one transparent solution; (2) the reaction of this transparent solution in autoclaves at scheduled temperature and period; (3) the collection of solvothermal products by centrifuging, washing and drying post-treatment process.

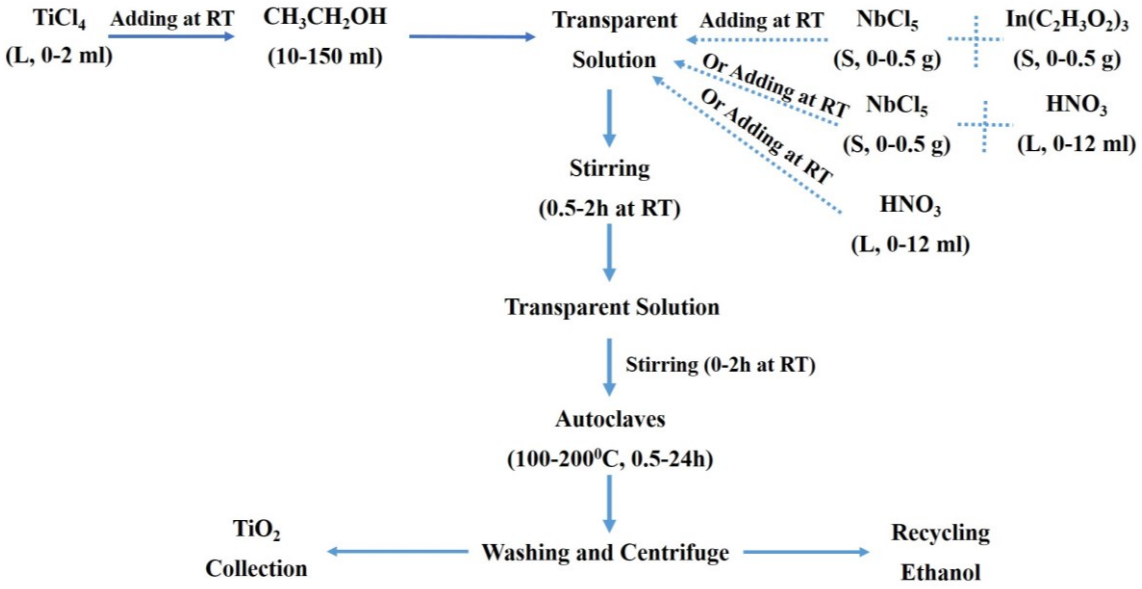

Figure 7, The experimental flowing chart for synthesizing (In^{3+}, Nb^{5+}), (N^{3-}, Nb^{5+}) and (N^{3-}, Ti^{3+}) co-doped anatase TiO_2 nanocrystals.

For example, to prepare (In^{3+}, Nb^{5+}) co-doped nanocrystals with the doping concertation of 4.6 at% of each dopant ion, 0.68 mL $TiCl_4$, 0.092 g $NbCl_5$ and 1.6406 g $In(C_2H_3O_2)_3$ were separately added into 120 mL ethanol solvent to form one transparent solution. This transparent solution was firstly stirred at room temperature for 2 hours and then transferred into an autoclave with the inner volume of about 200 mL. After the sealed autoclave was heated to 200 °C and kept at this temperature for 14 h, the solid product [*i.e.* (In^{3+}, Nb^{5+}) co-doped anatase TiO_2 nanocrystals] formed in the solution was centrifuged, washed with ethanol and distilled water, and finally dried at 60 °C for 12 h.

Replacing the added $In(C_2H_3O_2)_3$ by concentrated HNO_3 (69%), (N^{3-}, Nb^{5+}) co-doped anatase TiO_2 nanocrystals were synthesized following the similar process as the preparation of (In^{3+}, Nb^{5+}) co-doped TiO_2. Typically, $TiCl_4$ (0.68 mL) and $NbCl_5$ (0.092

g) were first added into ethanol (120 mL) solvent to form a transparent solution under magnetically stirring. HNO_3 with different volumes were then added into the transparent solution in order to effectively introduce nitrogen sources into the reaction solution. After the above mixture was stirred for two hours at room temperature, it was transferred into an autoclave with an inner volume of about 200 mL. The autoclave was sealed and heated at 200 °C for 12 h in an oven. When the autoclave cooled down to room temperature, the solvothermal product synthesized in the reaction solution [*i.e.*, (N^{3-}, Nb^{5+}) co-doped anatase TiO_2 nanocrystals] was separated by a centrifuge (20,000 rounds per minute), washed with ethanol (distilled water) for five times and finally dried at 60 °C for 12 h.

Further removing the added $NbCl_5$ from the receipe of synthesizing (N^{3-}, Nb^{5+}) co-doped anatase TiO_2 nanocrystals, (N^{3-}, Ti^{3+}) co-contained anatase TiO_2 nanocrystals can be also prepared by the similar solvothermal reaction route. However, due to the possible explosion of mixing ethanol and nitric acid, the volume of ethanol should be far more than that of concentrated HNO_3, and only the latter can be added into the former under magnetically stirring in order to effectively prevent their too vigorous chemical reaction.

2.3 Material characterization

2.3.1 Structural characterization

An X-ray diffractometer and a Raman spectroscopy were used to determine the crystal structure of synthesized solvothermal products. Through these two instruments, it can be judged whether the synthesized samples are pure phase and whether dopant or co-dopant ions have been incorporated into host materials. The regular changes of their related peaks will then confirm the possible "real" doping or co-doping.

X-ray Powder Diffraction. Powder X-ray diffraction patterns (XRD) of the synthesized ions co-doped/co-contained TiO_2 nanocrystals were characterized using a PANalytical's X-ray diffractometer with CuKα radiation. The applied voltage of X-ray diffractometer is 45 kV and the current is 40 mA. The setup step size is 0.013° and the time per step is 300s. The total scanning time in the range of 5° to 100° takes about 2 hours for each sample. Refining the collected XRD patterns through the JANA 2006 software, the average structural information of prepared solvothermal products including their phases, lattice parameters and others can be confirmed. In addition, the average crystallite sizes can be obtained by the calculation of Scherrer equation $D = \frac{K\lambda}{\beta cos\theta}$. In this equation, θ represents the Bragg angles and β is the line broadening at half the maximum intensity.

D is the average crystallite size; λ is the X-ray wavelength of CuKα radiation (0.15418 nm); and K is a dimensionless shape factor.

Raman Spectroscopy. Raman spectroscopy (a Renishaw Raman System using 532 nm laser) is a spectroscopic technique based on the principle of inelastic scattering of monochromatic light usually from a laser source. It can identify molecules and study chemical bonding of materials as structural fingerprint through different vibrational, rotational, and other low-frequency modes. Through analysing the different Raman active modes, the phase structure of samples and the possible defects can be demonstrated.

2.3.2 Chemical composition and chemical valence analysis

Given the difficulty in the quantitative analysis of N^{3-} ions, three different analytical instruments were used in this project. X-ray photoelectron spectroscopy is used to analyse the chemical valences and doping levels of N element nearing the sample surfaces. A thermogravimetric analysis equipment is used to detect the thermal decomposition behaviours of solvothermal products under gradually heating conditions, thus confirming the doping concentrations of N^{3-} ions. In addition, Nitrogen/Oxygen determinator is specially used to determine the N concentrations by immediately heating the samples to high temperatures of about 2000 °C in 2-5 seconds. It provides the total doping concentrations of N element in samples. Further analysing the measurement results from the above three different methods, an acceptable doping level of N^{3-} ions can be achieved, and the debates on "surface doping" or "bulk doping" can be solved.

X-ray Photoelectron Spectroscopy. X-ray photoelectron spectroscopy (XPS, Thermo-ESCALAB250Xi) is a surface-sensitive quantitative spectroscopic technique to analyse the surface chemistry of a material including elemental compositions at the parts per thousand range, chemical valences of the elements that exists within materials and others. Here, XPS is used to confirm the chemical valences and chemical compositions of In, Nb, N and Ti elements.

Thermogravimetric Analysis. Thermogravimetric analysis (TGA, STA 8000 of PerkinElmer) is a method of thermal analysis to present the changes of physical and chemical properties of materials with increasing temperatures or prolonging reaction time. It is commonly used to determine the mass loss or gain of samples due to the decomposition, oxidation, or the loss of volatiles. It is thus here used to analyse the doping level of N ions and the decomposition behaviour of samples at high temperature.

Nitrogen/Oxygen Determinator. Nitrogen/Oxygen determinator (N/O determinator, TC-600) is one instrument to particularly analyse nitrogen and oxygen elements in materials. It is thus used to analyse the doping concentration of N ions through evaporate all nitrogen ions in samples.

To determine the doping levels of metal ions including In^{3+}, Nb^{5+} or Ti^{4+}/Ti^{3+}, scanning electron microscope attached with energy dispersive X-ray spectroscopy and inductively coupled plasma optical emission spectrometry are used in this project. The detailed characterization process, the used instrument information and the required samples are described below.

Scanning Electron Microscope. A Hitachi 4300 SEM attached with an energy dispersive X-ray spectroscopy (EDS) was used to quantitatively analyse the chemical compositions at selected spots or areas of the samples. Prior to EDS measurements, the synthesized anatase nanopowders were firstly pressed into pellets and then sintered at 1400 °C for 20 h in order to achieve dense ceramic pellets. Subsequently, the ceramic pellets were polished to obtain smooth surfaces, and coated with carbon to avoid possible discharging.

Inductively Coupled Plasma Optical Emission Spectrometry. Inductively coupled plasma optical emission spectrometry (ICP-OES) is an analytical technique used for the detection of trace metals. Since ICP-OES has a high accuracy for the quantitative analysis of trace elements in samples, it is used to quantitatively characterize the doping concentrations of dopant ions including In, Nb and Ti in the synthesized co-doped TiO_2 nanocrystals. Furthermore, the analytical results of ICP-OES are also compared with that of SEM-EDS. It is found that the measured In and Nb doping concentrations achieved by the two different analysis methods are consistent to each other.

Besides XPS for the chemical valence analysis, electron paramagnetic resonance spectroscopy is further used to confirm the presence Ti^{3+} ions.

Electron Paramagnetic Resonance Spectroscopy. Electron paramagnetic resonance spectroscopy (EPR, a Bruker ER200D spectrometer) is a magnetic resonance method to detect unpaired electrons in materials. Since Ti^{3+} ions have unpaired electrons, they are easily to be distinguished from the EPR measurement. In this thesis project, EPR is thus used to demonstrate the presence of Ti^{3+} ions and its analytical result is consistent to that of XPS.

2.3.3 Morphological characterization and element mapping

To determine the particle shape and size of synthesized solvothermal products, field-emission scanning electron microscope and high-resolution transmission electron microscopy were used. Through the two technical tools, it can be also confirmed whether the synthesized samples contain possible impurities and whether the dopants/co-dopants are homogeneously distributed in nanocrystals.

Field-emission scanning electron microscope. Field-emission scanning electron microscope (FESEM, Zeiss-UltraPlus with an operating voltage of 15 kV) was used to characterize the morphologies and particle sizes of the ions co-doped TiO_2 nanocrystals synthesized experimentally in this thesis project.

Transmission Electron Microscopy. High-resolution transmission electron microscopy (HRTEM, JEOL-2100F) and aberration-corrected high-angle annular dark-field scanning transmission electron microscopy (HAADF-STEM, Double-corrected FEI Titan3 80-300 FEGTEM) were used to characterize the microscopic morphologies and co-doped information of synthesized ions co-doped TiO_2 nanocrystals. In particular, the HAADF-STEM imaging is highly sensitive to related variations of the atomic numbers in samples and thus can demonstrate whether co-dopant ions are "really doped" into the crystal structure of host TiO_2 nanomaterials.

2.3.4 Other characterizations

The light absorption behaviour and bandgap of solvothermal products were characterized by UV-Vis-NIR spectrophotometer; the chemical groups chemically or physically binding on sample surfaces were analysed by Fourier transform infrared spectroscopy; and the specific surface area of prepared nanocrystals was measured by Brunauer-Emmett-Teller instrument.

UV-Vis-NIR spectrophotometer. UV-Vis-NIR spectrophotometer (Varian, Cary 5G) is an instrument which measures the reflection or absorbance optical characteristics of materials. It is used to measure the optical absorption behaviours of the synthesized co-doped nanocrystals, and thus used to determines their bandgaps. It is also used to evaluate the catalytic effects of prepared TiO_2-based photocatalysts by measuring the decomposition of dyes (*e.g.* Rhodamine B, methylene blue or methylene orange *etc.*) under visible light illumination.

Fourier transform infrared spectroscopy. Fourier transform infrared spectroscopy (FT-IR, PerkinElmer) is a technique which is used to obtain an infrared spectrum of absorption

or emission of a solid, liquid or gas. It is thus used to analyse organic groups adsorbed on the surfaces of synthesized nanocrystals. The result of FT-IR is then connected with that of TGA to further confirm the heat-decomposition behaviour of the prepared ions co-doped TiO_2 nanocrystals.

B.E.T. instrument. Brunauer-Emmett-Teller instrument (B.E.T. QuadraSorb SI-MP) is applied in this research project to determine the specific surface area of synthesized nanoparticles. Prior to the measurement, the samples were degassed in vacuum at 423 K for 8 hours. The nitrogen adsorption-desorption data were then recorded at liquid nitrogen temperature (~77 K). The values are calculated through the equation $S = \frac{(V_m \times L_{av} \times A_M)}{W_t}$. In this equation, "*S*" stands for the specific surface area of samples; "V_m" is the monolayer capacity; " L_{av}" is the Avogadro's number (6.022×10^{23}); A_m is the cross-sectional area (1.62×10^{-19} m^2) and W_t is the molecular weight of N_2 (28.013 g mol^{-1}).

2.4 Measurement of visible light catalytic property

Rhodamine B (RhB) was chosen as a model organic compound to evaluate the photocatalytic effects of our synthesized (N, Nb) co-doped anatase TiO_2 nanocrystals. RhB solution (20 mg L^{-1}) was prepared by mixing RhB (20 mg) with distilled water (1 L). Then, (N, Nb) co-doped TiO_2 photocatalysts were added into the RhB solution with a mass concentration of 1 g L^{-1}. A 500 W Xe lamp with a 400 nm cut-off filter provided visible light irradiation for photocatalytic measurement. The resultant solution containing RhB and photocatalysts was stirred for 30 minutes in the dark to reach RhB adsorption equilibrium on the surfaces of (N, Nb) co-doped anatase TiO_2 nanocrystals, after which the photocatalytic reaction was initiated by illumination (time=0). The decomposition of RhB was characterized by a UV-Vis spectrometer based on a typical RhB peak at ~552 nm.

2.5 Measurement of high pressure reaction behaviour

A diamond anvil cell with a cullet size of 400 μm was employed to investigate the high-pressure behavior. A stainless steel gasket was indented to a thickness of 30 μm and a 200 μm diameter hole was drilled at the center. It served as the sample chamber. (In^{3+}+Nb^{5+}) co-doped anatase TiO_2 nanopowders and two small ruby balls were loaded into the above chamber. The mixture of 4 parts of ethanol and one part of methanol were used as the pressure transmitting medium within the cell. The sample was carefully loaded to 46.2 GPa in small steps. The pressure inside the diamond cell was determined by the pressure

dependent shift of the ruby fluorescence R1 line. In situ Raman measurements were taken using a Renishaw inVia Reflex Spectrometer System (532 nm laser).

Chapter 3. Major Publications

3.1 The formation of defect-pairs for highly efficient visible-light catalysts

I wrote the draft of this paper. I developed an approach for synthesizing (N^{3-}, Nb^{5+}) co-doped TiO_2 samples with different compositions. I characterized the related material properties using XRD, Raman spectroscopy, HRTEM, SEM/EDS, XPS, UV-VIS, N-O determinator, TGA-DSC and others. I also analysed the experimental results of DFT calculations performed by Terry J. Frankcombe and David Cortie, and the results of photocatalytic measurement conducted by Shaoyang Zhang.

The Formation of Defect-Pairs for Highly Efficient Visible-Light Catalysts

Qingbo Sun, David Cortie, Shaoyang Zhang, Terry J. Frankcombe, Guangwei She, Jie Gao, Leigh R. Sheppard, Wanbiao Hu, Hua Chen, Shangjun Zhuo, Dehong Chen, Ray L. Withers, Garry McIntyre, Dehong Yu, Wensheng Shi, and Yun Liu**

The gradual exhaustion of non-renewable resources has motivated researchers to investigate a wide range of materials for the highly efficient utilization of clean and renewable solar energy. Among these materials, visible-light catalysts (VLCs) are vital and ideal for photodegradation, dye-sensitized solar cells, hydrogen generation from water, as well as organic synthesis with the potential to convert more than ≈45% of sunlight to chemical or electrical energy. Most of the current VLCs like Ag_3PO_4,[1] $BiVO_4$,[2] or N-doped TiO_2[3] are only active in a certain solar spectral region and display limited photocatalytic performance. Other VLCs such as noble metal ions doped $SrTiO_3$[4] or decorated TiO_2[5,6] can extend the absorption edge to the whole visible-light regime but they suffer from rapid photogenerated charge carrier recombination due to the presence of trapping centers (e.g., oxygen vacancies) or impurity energy levels. The recombination of electron–hole pairs not only suppresses the solar energy conversion efficiency but also deteriorates the photocatalytic activity of VLCs. Therefore, high-performance photocatalysts should have broad light absorption while maintaining effective separation of electron–hole pairs in order to ensure the efficient utilization of solar energy for photocatalytic applications.

Technologically, several approaches have been proposed to date to enhance the photocatalytic performance of wide-bandgap semiconductors under visible-light irradiation. For instance, the lattice-disorder engineering of nanocrystalline TiO_2 (via hydrogenation) enables an effective combination of visible and infrared absorption with the additional benefit of carrier trapping on surfaces.[7] The design of a bandgap gradient distribution enables the solubility limits of undissolved ions to be increased and significantly inhibits the formation of recombination centers.[8] 3D-ordered construction of macroporous skeletons of N-doped TiO_2 also greatly enhances visible-light-driven photocatalytic properties by physically increasing surface area.[9] These different approaches represent substantial progress in the research and development of novel VLCs.

Ionic co-doping, especially cation and anion co-doping, is another facile route. Co-doping has recently drawn considerable attention[10–20] as this method can potentially tailor the energy band structure, enhance optical absorption, reduce the number of recombination centers by balancing charges and thus provide a cost-effective way to promote photocatalytic activity. The reported results, on the other hand, have been very diverse. There is no consensus concerning which type and what form of co-dopants should be introduced into host materials for achieving peak performance. Taking (N^{3-}, M^{5+}) co-doped TiO_2 as an example, where M^{5+} represents a pentavalent cation and N^{3-} is a nitrogen anion, it has been technologically difficult to introduce equivalent concentrations of M^{5+} and N^{3-} ions into a host material. High-temperature ammonolysis[10–15] was attempted to incorporate nitrogen ions into pre-prepared M^{5+} mono-doped TiO_2 but the achieved N^{3-} doping level was

Q. Sun, Dr. D. Cortie, Dr. W. Hu, Dr. D. Chen,
Prof. R. L. Withers, Prof. Y. Liu
Research School of Chemistry
The Australian National University
Canberra, ACT 2601, Australia
E-mail: yun.liu@anu.edu.au

Dr. D. Cortie, Prof. G. McIntyre, Dr. D. Yu
The Australian Nuclear Science and Technology Organisation
Lucas Height, NSW 2234, Australia

S. Zhang, Dr. G. She, Prof. W. Shi
Technical Institute of Physics and Chemistry
Chinese Academy of Sciences
Beijing 100190, China
E-mail: shiws@mail.ipc.ac.cn

Dr. T. J. Frankcombe
School of Physical
Environmental and Mathematical Sciences
The University of New South Wales
Canberra, ACT 2601, Australia

J. Gao, Prof. S. Zhuo
Analysis and Testing Center for Inorganic Materials
Shanghai Institute of Ceramics
Chinese Academy of Sciences
Shanghai 200050, China

Dr. L. R. Sheppard
School of Computing
Engineering and Mathematics
Western Sydney University
Penrith, NSW 2751, Australia

Dr. H. Chen
Centre for Advanced Microscopy
The Australian National University
Canberra, ACT 2601, Australia

DOI: 10.1002/adma.201605123

less than 2 at%.[12,21] In addition, the distribution of N^{3-} ions is often inhomogeneous with its concentration gradually lowering from the surface to the interior of co-doped TiO_2.[8] Wet chemical methods like sol–gel synthesis have also been tried to directly add nitrogen sources to the reaction solution.[17–20] However, the post-calcination treatment for crystallinity at temperatures over 400 °C inevitably leads to the loss of N^{3-} ions.[22] Therefore, a well-balanced stoichiometric ratio of M^{5+} to N^{3-} has never been realized, although photocatalytic properties have been moderately improved.

From a theoretical perspective, there is also ambiguity concerning the electronic and chemical configurations of specific co-dopants in host materials and the related consequences for photocatalytic properties. The formation of impurity energy levels in the bandgap,[23] the creation of mid-gap energy levels,[11,17] the appearance of Ti^{3+} states and F^+ centers,[10,17,24] interstitial nitrogen states[25] as well as the red shift of the absorption edge[10,26] have all been suggested as mechanisms for the observed enhancement of photocatalytic activity. Some investigators believe that cation–anion co-dopants can bind together to form defect-pairs[27,28] while other work emphasizes the role of decoupled point defects formed under typical chemical conditions.[11,16] Our recent work on the development of co-doped TiO_2-based colossal permittivity materials[29,30] demonstrated the complexity of ionic co-doping in structurally strongly correlated oxides. Once co-doped ions are introduced into host materials, they may stay as isolated point defects by either replacing ions in regular lattice sites or occupying interstitial positions. They may also form defect-pairs or clusters coupled with the host ions and local crystal structure. The former presents an additive effect of point defects and the latter results in a significant emergent behavior due to the combination of co-doped ions into a unique defect-pair or cluster form. The formation of defect states strongly depends on the preparation conditions and methods of material synthesis.

With this in mind, we have strategically designed a new approach for the development of (N^{3-}, M^{5+}) co-doped TiO_2 with higher N^{3-} concentrations for a real synergistic and cooperative interaction between co-dopants. That is, another ion should be introduced to improve the local crystal chemical environment for accommodating more nitrogen ions. In this scenario, the two co-dopants must interact closely with each other within a small vicinity to form defect-pairs or clusters. The impact of newly formed defect-pairs or clusters would be expected to behave as a new type of defect which not only has the special features of individual dopant but also effectively avoids the drawbacks of single doping. In the case of (N^{3-}, Nb^{5+}) co-doped anatase TiO_2 nanocrystals, the following factors were further considered: i) the well-balanced charges of N^{3-} and Nb^{5+} ions to the maximum extent avoiding the generation of additional defects such as Ti^{3+} ions or oxygen vacancies ($V_O^{\cdot\cdot}$); ii) the more difficult reduction of Nb^{5+} ions than Ti^{4+} ions to keep the chemical valence of niobium dopants experimentally controllable; and iii) the formation of strong correlation (defect-pairs) between N^{3-} and Nb^{5+} ions to activate significant emergent behaviors for the physicochemical properties. The resultant materials were subsequently characterized as VLCs for water purification using Rhodamine B (RhB) as a model pollutant. Density functional theory (DFT) calculations were performed to gain insight into the observed photocatalytic effects and the related mechanisms arising from the formation of highly concentrated N^{3-}–Nb^{5+} defect-pairs. This study demonstrates how to design and develop novel photocatalytic materials for highly efficient conversion of solar energy.

In order to efficiently introduce nitrogen ions into host materials and simultaneously avoid nitrogen evaporation during subsequent high-temperature processing, a solvothermal reaction route was used in this work for material synthesis. This enables the chemical reaction to occur homogeneously at the molecular level under pressure and at a lower temperature. This method also prevents the loss of nitrogen ions during reaction due to the closed environment. For instance, to successfully synthesize (N, Nb) co-doped TiO_2, $NbCl_5$ and $TiCl_4$ are dissolved in ethanol and chemically reacted with nitric acid at 200 °C for 12 h.[31] Repeating this reaction procedure, we synthesized a series of (N, Nb) co-doped TiO_2 samples, where the nominal concentration of Nb^{5+} ions was fixed during the whole experimental process while the nominal N^{3-} doping level was varied by adjusting the concentration of nitric acid in the reaction solution (Section SI-1, Supporting Information). After optimization, the structure and chemical compositions of the resultant solvothermal products were determined by X-ray powder diffraction (XRPD), high-resolution transmission electron microscopy (HRTEM), field-emission scanning electron microscopy (FESEM), and X-ray photoelectron spectroscopy (XPS). Additionally, a nitrogen/oxygen determinator, thermogravimetric analysis, and differential scanning calorimetry were also used to further estimate the resultant nitrogen concentrations (Section SI-6, Supporting Information), which were found to be reasonably consistent with the results determined by XPS. The experimental details are presented in Section SI-2 (Supporting Information).

The typically synthesized samples were experimentally analyzed to have Nb^{5+} ionic concentrations of about 5.4, 5.3, and 5.6 at% per $\left(Ti^{4+}_{1-x-y}Ti^{3+}_{x}Nb^{5+}_{y}\right)\left(O^{2-}_{2-y'-z}\square_z N^{3-}_{y'}\right)$ formula unit and N^{3-} ionic concentrations of about 3.7, 5.6, and 7.5 at% (labeled as N-poor, N-equal and N,-rich), respectively (Section SI-5 and SI-6, Supporting Information). XRPD analysis (**Figure 1**a) suggests that all prepared (N, Nb) co-doped TiO_2 particles belong to the anatase phase with space group symmetry $I4_1/amd$. The diffraction peaks are very broad, indicating that the materials have a small particle size, further calculated via the Scherrer equation (Equation S1, Supporting Information) to show their average diameters are less than 10 nm (Section SI-8, Supporting Information). This is also confirmed by a FESEM image (Figure S2a, Supporting Information), but more accurately estimated by HRTEM lattice images (Figure 1c; Section SI-7 and SI-8, Supporting Information). From ⟨100⟩ oriented HRTEM lattice images (Figure 1c, insets in Figure S2c,d of the Supporting Information), it is found that the dominant exposed crystal faces of these three different (N, Nb) co-doped TiO_2 nanoparticles are {011} facets combined, to a lesser extent, with (002) facets. Furthermore, the three types of samples have almost equivalent specific surface area (≈170 $m^2\ g^{-1}$, Section SI-9, Supporting Information). In addition, we observed that the color of the synthesized nanoparticles varied from light brown to dark brown with increasing N^{3-} concentrations (Figure 1b). This color variation clearly indicates a change in

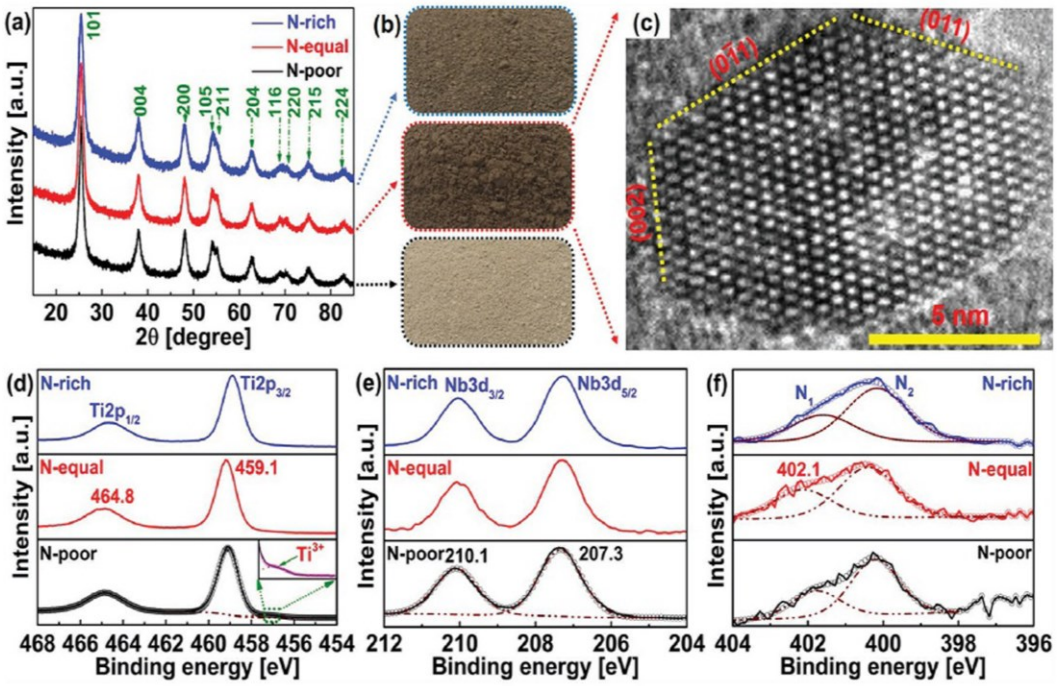

Figure 1. a–c) XRD patterns (a), photographs (b), an HRTEM lattice image (c) along a ⟨100⟩ direction, and d–f) XPS data of N-poor (5.4 at% Nb^{5+} + 3.7 at% N^{3-}), N-equal (5.3 at% Nb^{5+} + 5.6 at% N^{3-}), and N-rich (5.6 at% Nb^{5+} + 7.5 at% N^{3-}) co-doped TiO_2 nanocrystals which were synthesized by the solvothermal reaction.

their visible-light absorption, as will be further demonstrated below. From XPS analysis (Figure 1d–f; Section SI-5, Supporting Information), it is found that some Ti^{4+} ions of the N-poor TiO_2 samples are reduced to Ti^{3+} ions to compensate for the additional positive charges associated with the excessive Nb^{5+} ions. As a result of charge compensation, the total doping concentrations of Ti^{3+} (1.7 at%) and N^{3-} (3.7 at%) are equal to that of Nb^{5+} (5.4 at%). Similarly, oxygen vacancies ($V_O^{\cdot\cdot}$, labeled as $\square_z$ in the formula unit above) are generated in the N-rich co-doped TiO_2 to balance the extra negative charges arising from the excess N^{3-} ions. If Nb^{5+} and N^{3-} ions are doped at equal concentrations, i.e., if $y = y'$, neither Ti^{3+} ions nor $V_O^{\cdot\cdot}$ defects would be generated. In fact, no such defects are observed even in our N-equal co-doped samples where the concentrations of Nb^{5+} and N^{3-} are not exactly identical but very close (5.3 at% Nb^{5+} + 5.6 at% N^{3-}). It is evident that the N doping level per formula unit can reach up to 7.5 at% with Nb^{5+} co-doping using this solvothermal reaction route. Such a high N^{3-} doping level suggests that Nb^{5+} co-doping facilitates the introduction of N^{3-} ions into anatase TiO_2.

Figure 2a shows the optical absorption spectra of (N, Nb) co-doped TiO_2 nanoparticles. Their light absorption range covers the entire visible-light regime from 400 to 800 nm, which is much broader, relative to the results previously reported for (N, Nb) co-doped TiO_2 particles.[10–15,17–20] For the N-equal and N-rich co-doped TiO_2 with higher N^{3-} doping levels, the

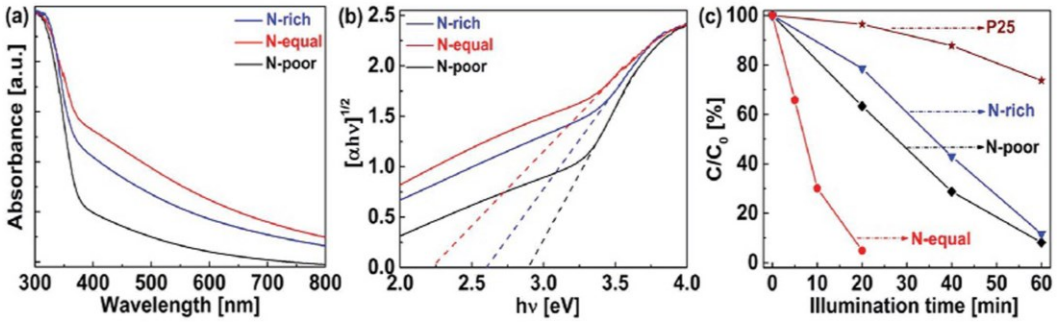

Figure 2. a,b) UV–Vis absorption spectra (a) and associated Tauc plots (b) of three typical N-poor (5.4 at% Nb^{5+} + 3.7 at% N^{3-}), N-equal (5.3 at% Nb^{5+} + 5.6 at% N^{3-}) and N-rich (5.6 at% Nb^{5+} + 7.5 at% N^{3-}) co-doped TiO_2 nanocrystals. c) Photocatalytic degradation of Rhodamine B under visible-light irradiation ($\lambda \geq 400$ nm) using these nanocrystals as visible-light catalysts, where the commercial Degussa P25-TiO_2 is also measured for a reference.

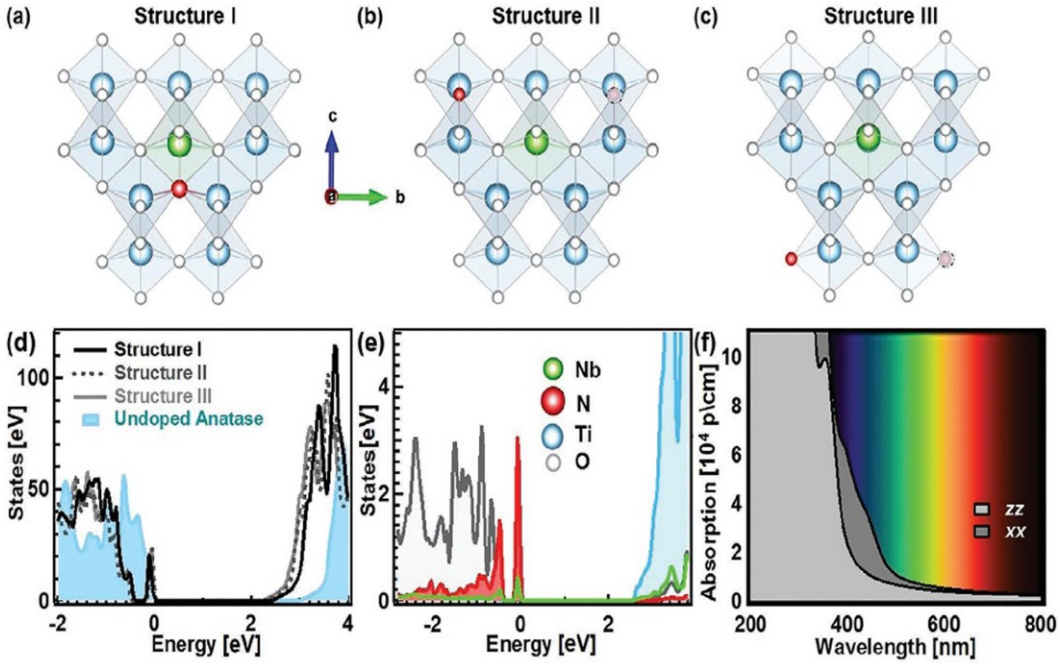

Figure 3. a–c) Candidate defect-pair chemical structures (I–III) considered for DFT calculations of substitutional Nb and N in anatase TiO_2. The dotted circles indicate the symmetry-equivalent position of the nitrogen positioned in the supercell. d) The total density of states calculated using the mBJ potential in the three structures compared to undoped anatase TiO_2, with $E = 0$ corresponding the Fermi energy. e) The partial density of states for the lowest-energy defect-pair structure (I) showing the shallow nitrogen acceptor lever in the gap and the Nb 3d states high in the conduction band. f) Calculated optical absorption coefficient from structure I for two components (*xx*, *zz*) of the anisotropic optical tensor, showing absorption into the visible-light region (400–700 nm) depicted by the overlaid spectrum.

respective light absorption even extends into the near-infrared regime. The strongest light absorption is observed in our N-equal TiO_2 with almost identical Nb^{5+} and N^{3-} doping concentrations (5.3 at% Nb^{5+} + 5.6 at% N^{3-}). This is in good agreement with their color change (Figure 1b). In addition, the Tauc plots of Figure 2b show that the bandgap of these co-doped TiO_2 materials becomes significantly narrower with increasing N^{3-}. The bandgap values are ≈2.9 and ≈2.6 eV for N-poor and N-rich samples, respectively. The N-equal TiO_2 is even better with a bandgap reduction to ≈2.2 eV, demonstrating the importance of fine-tuning chemical scheme to give charge-compensated defects in balanced concentrations.

The photocatalytic activity of these VLCs is investigated by measuring the decomposition of RhB under visible-light irradiation, using a 500 W Xe lamp with a cutoff wavelength of 400 nm. Experimental details are presented in Section SI-3 (Supporting Information). Compared with the commercial Degussa P25-TiO_2, the photocatalytic activity of all three (N, Nb) co-doped anatase TiO_2 samples is superior and the N-equal co-doped TiO_2 is outstanding (Figure 2c). As seen, the N-equal co-doped TiO_2 requires less than 20 min to accomplish nearly complete decomposition of RhB. It is noticed that the N-poor, N-equal, and N-rich co-doped TiO_2 nanocrystals have similar average particle sizes, the analogous crystal facets exposed on the surface, almost equivalent specific surface area (Section SI-9, Supporting Information), but show a clear difference in VLC effect. Hence, it is concluded that N^{3-} and Nb^{5+} ionic co-doping, which has been experimentally realized by the solvothermal reaction route, is critical to stabilize the N-doping and/or accommodate more N^{3-} ions in the host TiO_2. High co-dopant loading is significant to improve photocatalytic activity, but the charge-compensated defects in balanced Nb^{5+} and N^{3-} concentrations are a decisive factor influencing the outstanding visible-light catalytic performance in this material.

To elucidate how the (N, Nb) co-doping strategy modifies the electronic structure and leads to the enhanced VLC performance, first principles calculations were performed. **Figure 3**a–c shows some of the candidate chemical structures that were modeled using DFT calculations for the (N, Nb) co-doped TiO_2 compound. The starting configurations were generated by substituting equivalent Nb and N into various Ti and O sites with dopant concentrations (≈6.25 at%) close to the optimal experimental values (≈5.3 at% Nb^{5+} + 5.6 at% N^{3-}), and then allowing the ions to relax to low-energy configurations using the Perdew–Burke–Ernzerhof (PBE) functional. **Table 1** reports the total energies, indicating that it is energetically favorable to position substitutional N–Nb in a nearest neighbor configuration (Structure I). Indeed, the energy cost for positioning N–Nb further apart is ≈0.1 eV (Structures II and III), setting the corresponding temperature scale in the thermodynamic limit as $\Delta E/k_B = 1160$ K, where k_B is the Boltzmann constant. For this reason, the formation of structures such as II and III are improbable under the experimental synthesis conditions of this work and the local crystal

Table 1. Density functional theory calculations for candidate defect-pair chemical structures (I–III). The total energy has been computed using the general gradient approximate (GGA)-PBE functional, whereas the bandgap values were obtained using the mBJ potential.

Samples	Nb–N distance [Å]	Energy [eV]	Bandgap [eV]
Structure I	1.929	0	2.43
Structure II	4.289	0.116	2.40
Structure III	6.001	0.124	2.36
Pure anatase	–	–	2.98

chemistry favors the formation of directly bonded N–Nb configurations, i.e., defect-pairs.

To model the electronic effects of the resultant defect-pairs, the density of states (DOSs) was calculated using the modified Becke–Johnson (mBJ) potential which is a parameter-free ab initio method for the bandgap prediction.[32,33] The total DOSs for undoped and (N, Nb) co-doped anatase TiO_2 with various doped structures (I–III) are shown in Figure 3d. The calculated bandgap lies within 10% of the experimental values, for example, producing 2.98 eV for undoped anatase TiO_2 (experimental value 3.1–3.2 eV).[34] All of the structures that contain Nb and N have a reduced bandgap compared to the pure anatase structure, with values close to 2.4 eV (Table 1). This corroborates the main optical bandgap (≈2.2 eV) observed in the experiment (Figure 2b). The first principles calculations hence again indicate some cooperative electronic effect of the Nb and N species. Figure 3e shows the element-specific partial DOSs for the nearest-neighbor N–Nb structure I demonstrating that the Nb levels are high in the conduction band whereas the N forms a shallow acceptor level that almost overlaps the valence band maxima. The combination of these properties ensures thermal occupation under typical experimental conditions, providing an effective way to engineer the band-edge. Moreover, the Fermi energy offset from the valence band (taken as the $E = 0$) is not modified compared to pure anatase TiO_2, illustrating the advantages of the passivated co-doping involved with the N^{3-}–Nb^{5+} defect-pairs. This enhances photocatalytic performances by preventing unwanted recombination pathways for photogenerated charge carriers.[28]

To directly show that the N^{3-}–Nb^{5+} defect-pairs also enhance the harvesting of visible light, we calculated the optical absorption predicted for the resulting electronic structure. Figure 3f shows the absorption coefficient for the nearest-neighbor N^{3-}–Nb^{5+} defect-pair structure I based on the joint-density-of-states method.[35] Both absorption tensor components (*xx* and *zz*) indicate finite absorption into the visible regions, tailing off rapidly near the indirect-bandgap energy (516 nm). By contrast, we also report the electronic-structure calculations for interstitial nitrogen species (Section SI-10, Supporting Information) as some researchers think that they might play a crucial role in nitrogen mono-doped TiO_2.[36] However, the calculated results for such interstitial nitrogen species in the neighborhood of Nb^{5+} ions show that light absorption is only achieved below 440 nm (≈2.82 eV), which represents a significant drop in light-harvesting performance. Clearly, the electronic structure originating from the N^{3-}–Nb^{5+} defect-pairs in closely neighboring substitutional positions is a key to producing enhanced visible absorption which is necessary for high photocatalytic performance.

In summary, this work introduces the concept of defect-pairs to make anatase TiO_2 a strikingly superior VLC. This is because the formation of highly concentrated defect-pairs, in this case N^{3-}–Nb^{5+}, will greatly reduce the bandgap, enhance visible-light absorption, and diminish photoexcited charge carrier recombination. The realization of high nitrogen concentrations benefits from the defect design and the formation of N^{3-}–Nb^{5+} defect-pair structure. Solvothermal reaction provides an effective approach to further promote the achievement of such high level of co-dopants. Given that the improvements in the TiO_2-based VLC performance have been very limited despite massive efforts over the past three decades, this work provides a breakthrough in the design of TiO_2-based VLCs. The new mechanism and associated strategy we have developed here not only elevate TiO_2 to the ranks of the best available VLCs, thus benefiting all practical applications, but also provide new insights to improve existing and newly developing VLCs for a clean environment (e.g., waste-water/chemical treatment) and renewable energy (e.g., water splitting for hydrogen generation).

Experimental Section

The detailed information about the synthesis and analysis of (N, Nb) co-doped anatase TiO_2 nanocrystals, the characterization of photocatalytic performance, density functional theory calculations and other related materials are available in the Supporting Information.

Supporting Information

Supporting Information is available from the Wiley Online Library or from the author.

Acknowledgements

Q.S., D.Co., T.J.F. and Y.L. acknowledge the support of the Australian Research Council (ARC) in the form of Discovery Projects. Y.L. and T.J.F. also appreciate the support from the ARC Future Fellowships program. S.Z., G.S. and W.S. thank the financial support from CAS (XDB17030000) and MOST of China (2016YFA0200800). The authors also appreciate Antonio Tricoli and Guanyu Liu (the Australian National University) for their assistance in the B.E.T. measurement and Bill Gong (University of New South Wales) for his help in XPS characterization. The authors acknowledge the facilities and the scientific and technical assistance of the Australian microscopy and microanalysis research facility (AMMRF) at the Centre of advanced Microscopy, the Australian National University. Q.S., D.Co., Y.L., W.S., and T.J.F. make the main contribution to the preparation of this manuscript. Y.L. initiated this research, planned and coordinated all experimental and theoretical work. W.S. and T.J.F. supervised the photocatalytic and theoretical work collaborated with Y.L. Q.S. developed the approach for the fabrication of the samples with different compositions and synthetic conditions. S.Z. and G.S. conducted the photocatalytic experiment. D.Co. conducted theoretical calculation, collaborated with G.M. and D.Y.. Q.S., W.H., R.L.W., L.R.S., and D.Ch. conducted HRTEM, SEM/EDS, XPS, and light absorption with the assistance of H.C. and L.R.S.. J.G. and S.Z. conducted the chemical composition analysis relevant to nitrogen. All the authors were involved in the data analysis and discussion as well as manuscript preparation. The authors declare no competing financial interest.

Note: Figure 3 was replaced on March 15, 2017, after initial publication online. In the figure when originally published, the symmetry-equivalent position of the nitrogen was not properly displayed.

Received: September 22, 2016
Revised: December 8, 2016
Published online: January 23, 2017

[1] Z. Yi, J. Ye, N. Kikugawa, T. Kako, S. Ouyang, H. Stuart-Williams, H. Yang, J. Cao, W. Luo, Z. Li, Y. Liu, R. L. Withers, *Nat. Mater.* **2010**, *9*, 559.
[2] T. W. Kim, Y. Ping, G. A. Galli, K.-S. Choi, *Nat. Commun.* **2015**, *6*, 8769.
[3] R. Asahi, T. Morikawa, T. Ohwaki, K. Aoki, Y. Taga, *Science* **2001**, *293*, 269.
[4] K. Iwashina, A. Kudo, *J. Am. Chem. Soc.* **2011**, *133*, 13272.
[5] Q. Zhang, D. Q. Lima, I. Lee, F. Zaera, M. Chi, Y. Yin, *Angew. Chem.* **2011**, *123*, 7226.
[6] L. Jing, W. Zhou, G. Tian, H. Fu, *Chem. Soc. Rev.* **2013**, *42*, 9509.
[7] X. Chen, L. Liu, P. Y. Yu, S. S. Mao, *Science* **2011**, *331*, 746.
[8] G. Liu, L.-C. Yin, J. Wang, P. Niu, C. Zhen, Y. Xie, H.-M. Chen, *Energy Environ. Sci.* **2012**, *5*, 9603.
[9] T. Wang, X. Yan, S. Zhao, B. Lin, C. Xue, G. Yang, S. Ding, B. Yang, C. Ma, G. Yang, G. Yang, *J. Mater. Chem. A* **2014**, *2*, 15611.
[10] T. M. Breault, B. M. Bartlett, *J. Phys. Chem. C* **2012**, *116*, 5986.
[11] C. Marchiori, G. D. Liberto, G. Soliveri, L. Loconte, L. L. Presti, D. Meroni, M. Ceotto, C. Oliva, S. Cappelli, G. Cappelletti, C. Aieta, S. Ardizzone, *J. Phys. Chem. C* **2014**, *118*, 24152.
[12] T. M. Breault, J. J. Brancho, P. Guo, B. M. Bartlett, *Inorg. Chem.* **2013**, *52*, 9363.
[13] S. Hoang, S. Guo, C. B. Mullins, *J. Phys. Chem. C* **2012**, *116*, 23283.
[14] T. Cottineau, N. Béalu, P.-A. Gross, S. N. Pronkin, N. Keller, E. R. Savinova, V. Keller, *J. Mater. Chem. A* **2013**, *1*, 2151.
[15] T. M. Breault, B. M. Bartlett, *J. Phys. Chem. C* **2013**, *117*, 8611.
[16] H. Choi, D. Shin, B. C. Yeo, T. Song, S. S. Han, N. Park, S. Kim, *ACS Catal.* **2016**, *6*, 2745.
[17] J. Lim, P. Murugan, N. Lakshminarasimhan, J. Y. Kim, J. S. Lee, S.-H. Lee, W. Choi, *J. Catal.* **2014**, *310*, 91.
[18] P. Zhang, S. Yin, T. Sekino, S. W. Lee, T. Sato, *Res. Chem. Intermed.* **2013**, *39*, 1509.
[19] Y. Shen, T. Xiong, J. Shang, K. Yang, *Res. Chem. Intermed.* **2008**, *34*, 353.
[20] L. Rimoldi, C. Ambrosi, G. D. Liberto, L. L. Presti, M. Ceotto, C. Oliva, D. Meroni, S. Cappelli, G. Cappelletti, G. Soliveri, S. Ardizzone, *J. Phys. Chem. C* **2015**, *119*, 24104.
[21] C. Burda, Y. Lou, X. Chen, A. C. S. Samia, J. Stout, J. L. Gole, *Nano Lett.* **2003**, *3*, 1049.
[22] T. C. Jagadale, S. P. Takale, R. S. Sonawane, H. M. Joshi, S. I. Patil, B. B. Kale, S. B. Ogale, *J. Phys. Chem. C* **2008**, *112*, 14595.
[23] Q. Meng, T. Wang, E. Liu, X. Ma, Q. Ge, J. Gong, *Phys. Chem. Chem. Phys.* **2013**, *15*, 9549.
[24] A. Folli, J. Z. Bloh, A. Lecaplain, R. Walker, D. E. Macphee, *Phys. Chem. Chem. Phys.* **2015**, *17*, 4849.
[25] S. Banerjee, S. C. Pillai, P. Falaras, K. E. O'Shea, J. A. Byrne, D. D. Dionysiou, *J. Phys. Chem. Lett.* **2014**, *5*, 2543.
[26] R. Long, N. J. English, *Chem. Phys. Lett.* **2009**, *478*, 175.
[27] X. Ma, Y. Wu, Y. Lu, J. Xu, Y. Wang, Y. Zhu, *J. Phys. Chem. C* **2011**, *115*, 16963.
[28] Y. Gai, J. Li, S.-S. Li, J.-B. Xia, S.-H. Wei, *Phys. Rev. Lett.* **2009**, *102*, 036402.
[29] W. Hu, Y. Liu, R. L. Withers, T. J. Frankcombe, L. Norén, A. Snashall, M. Kitchin, P. Smith, B. Gong, H. Chen, J. Schiemer, F. Brink, J. Wong-Leung, *Nat. Mater.* **2013**, *12*, 821.
[30] W. Hu, K. Lau, Y. Liu, R. L. Withers, H. Chen, L. Fu, B. Gong, W. Hutchison, *Chem. Mater.* **2015**, *27*, 4934.
[31] Y. Liu, Q. Sun, R. L. Withers, W. Shi, *AU 2016903458*, **2016**.
[32] F. Tran, P. Blaha, *Phys. Rev. Lett.* **2009**, *102*, 226401.
[33] P. Blaha, K. Schwarz, G. K. H. Madsen, D. Kvasnicka, J. Luitz, *WIEN2k: An Augmented Plane Wave + Local Orbitals Program for Calculating Crystal Properties*, Techn. Universität, Vienna, Austria **2001**.
[34] D. O. Scanlon, C. W. Dunnill, J. Buckeridge, S. A. Shevlin, A. J. Logsdail, S. M. Woodley, C. R. A. Catlow, M. J. Powell, R. G. Palgrave, I. P. Parkin, G. W. Watson, T. W. Keal, P. Sherwood, A. Walsh, A. A. Sokol, *Nat. Mater.* **2013**, *12*, 798.
[35] C. Ambrosch-Draxl, J. O. Sofo, *Comput. Phys. Commun.* **2006**, *175*, 1.
[36] M. Ceotto, L. L. Presti, G. Cappelletti, D. Meroni, F. Spadavecchia, R. Zecca, M. Leoni, P. Scardi, C. L. Bianchi, S. Ardizzone, *J. Phys. Chem. C* **2012**, *116*, 1764.

ADVANCED MATERIALS

Supporting Information

for *Adv. Mater.*, DOI: 10.1002/adma.201605123

The Formation of Defect-Pairs for Highly Efficient Visible-Light Catalysts

Qingbo Sun, David Cortie, Shaoyang Zhang, Terry J. Frankcombe, Guangwei She, Jie Gao, Leigh R. Sheppard, Wanbiao Hu, Hua Chen, Shangjun Zhuo, Dehong Chen, Ray L. Withers, Garry McIntyre, Dehong Yu, Wensheng Shi, and Yun Liu**

Supporting information (SI)

The Formation of Defect-pairs for Highly Efficient Visible Light Catalysts

*Qingbo Sun, David Cortie, Shaoyang Zhang, Terry J. Frankcombe, Guangwei She, Jie Gao, Leigh R. Sheppard, Wanbiao Hu, Hua Chen, Shangjun Zhuo, Dehong Chen, Ray L. Withers, Garry McIntyre, Dehong Yu, Wensheng Shi** and Yun Liu**

SI-1, The synthesis of (N, Nb) co-doped anatase TiO_2 nanocrystals

(N, Nb) co-doped anatase TiO_2 nanocrystals were synthesized by a solvothermal method. Typically, $TiCl_4$ (0.68 mL) and $NbCl_5$ (0.092 g) were first added into ethanol (120 mL) solvent to form a transparent solution under magnetically stirring. HNO_3 (69%) with the respective volumes (1, 2 and 4 mL) were then added into the transparent solution in order to effectively introduce the nitrogen source into the reaction solution. After the above mixture was stirred for two hours at room temperature, it was transferred into an autoclave with an inner volume of about 200 mL. The autoclave was sealed and heated at 200 °C for 12 h in an oven. When the autoclave cooled down to room temperature, the solvothermal product synthesized in the reaction solution was separated by a centrifuge (20,000 rounds $minute^{-1}$), washed with ethanol (distilled water) for five times and finally dried at 60 °C for 12 h. Following this reaction and collection route, (N, Nb) co-doped anatase TiO_2 nanocrystals with fixed Nb^{5+} doping concentrations and variable N^{3-} doping concentrations were synthesized. According to the measured doping concentrations of nitrogen ions, the synthesized products were labelled as N-poor, N-equal and N-rich, respectively.

SI-2, Compositional, structural and spectral characterization of (N, Nb) co-doped anatase TiO_2 nanocrystals

(N, Nb) co-doped anatase TiO_2 nanocrystals were analyzed by X-ray powder diffraction (XRPD,

PANalytical's X-ray diffractometer with CuKα radiation), high-resolution transmission electron microscope (HRTEM, JEOL-2100F), field-emission scanning electron microscope (FESEM, Zeiss, UltraPlus) and UV-VIS-NIR spectrophotometer (Varian, Cary 5G). The chemical valence and atomic percentage of Nb, N and Ti in the co-doped nanocrystals were carefully analyzed by X-ray photoelectron spectroscopy (XPS, Thermo ESCALAB250Xi). Nitrogen/Oxygen (N/O) determinator (TC-600, LECO) was also utilized to estimate the doping levels of nitrogen ions (measured in Helium gas, 450 mL per minute). Additionally, the thermogravimetric (TG) and differential scanning calorimetric (DSC) data were collected by STA 8000 (PerkinElmer) with the heating rates of 5 °C per minute in the flowing air (20 mL per minute) to understand the stability and concentration of nitrogen in the samples. The specific surface area was measured through the Brunauer-Emmett-Teller (B.E.T.) method with QuadraSorb SI-MP instrument. Prior to the measurement, the samples were degassed in vacuum at 423 K for 8 hours. The nitrogen adsorption-desorption data were then recorded at liquid nitrogen temperature (~77 K).

SI-3, The characterization of photocatalytic performance

Rhodamine B (RhB) was chosen as a model organic compound to evaluate the photocatalytic activities of our synthesized (N, Nb) co-doped anatase TiO_2 nanocrystals. RhB solution (20 mg L^{-1}) was prepared by mixing RhB (20 mg) with distilled water (1 L). Then, (N, Nb) co-doped TiO_2 photocatalysts were added into the RhB solution with a mass concentration of 1 g L^{-1}. A 500 W Xe lamp with a 400 nm cut-off filter provided visible light irradiation for photocatalytic measurement. The resultant solution containing RhB and photocatalysts was stirred for 30 minutes in the dark to reach RhB adsorption equilibrium on the surfaces of (N, Nb) co-doped anatase TiO_2 nanocrystals, after which the photocatalytic reaction was initiated by illumination

(time=0). The decomposition of RhB was characterized by a UV-Vis spectrometer based on a typical RhB peak at ~552 nm.

SI-4, Density functional theory calculations

The calculations were performed under periodic boundary conditions in a 2×2×1 supercell by reference to the unit cell of pure anatase TiO_2. Atomic positions and the cell parameters were optimized using ionic relaxation, and the resulting total energy of the various defect-pair structures was evaluated accurately using PBE-GGA PAW potentials[S1,S2] with a plane-wave basis cutoff of 400 eV in the VASP software.[S3,S4] The number of outer electrons treated as valence for each element in VASP calculations was: Ti (12), O (6), Nb (13) and N (5). After structural relaxation, the density of electronic states of the resulting structures was calculated using the WIEN2K software that implements an all-electron method.[33] For the final electronic structure calculation of defect-pairs, we deployed the sophisticated modified-Becke-Johnson (mBJ) potential that allows a parameter-free method to accurately predict experimental bandgaps, which substantially improves on the Kohn-Shan bandgaps predicted by the Local Density Approximation (LDA) or Generalized Gradient Approximation (GGA).[32] The fully relaxed GGA chemical structures were used as the input for the mBJ electronic structure calculation in WIEN2K.[32,33] The calculations were well converged with respect to the size of the k-mesh (6×6×6 points) and plane-wave cutoff (R_{KMax}=8). Unlike previous LDA/GGA calculations, the absolute values of the calculated mBJ bandgap for the co-doped (2.4 eV) and pure anatase (2.98 eV) are also close to the experimental values, further demonstrating the accuracy of the mBJ approach in this case. It is noteworthy that the experimental light absorption also has a weak tail that extends out to longer wavelengths (800 nm) than the theoretical calculation. Analyzing the experimental data closely indicates a mixture of absorption mechanisms that include strong interband transitions together with a second weaker mechanism facilitating sub-band gap absorption. In particular, the latter seems to correspond

with dipole-forbidden indirect transitions, not modelled in the DFT calculations that necessarily exclude finite-size, excitonic and phononic effects.[35]

SI-5, XPS analysis of (N, Nb) co-doped anatase TiO_2 nanocrystals

Table S1. The atomic percentages of cations (Nb^{5+}, Ti^{3+} and Ti^{4+}) and N^{3-} in (N, Nb) co-doped anatase TiO_2 nanocrystals measured by XPS.

	The ratio of selected ions to total ions [at.%]				The ratio of doped ions to total *C*[a] [at.%]		
Samples	Nb^{5+}	N^{3-}	Ti^{3+}	Ti^{4+}	y (=Nb^{5+}/*C*)	y' (=N^{3-}/*C*)	x (=Ti^{3+}/*C*)
N-poor	1.27	0.87	0.4	21.79	5.4	3.7	1.7
N-equal	1.26	1.34	0	22.59	5.3	5.6	0
N-rich	1.32	1.77	0	22.34	5.6	7.5	0

[a] Here, "*C*" represents all cations in (N, Nb) co-doped anatase TiO_2 nanocrystals which include Nb^{5+}, Ti^{3+} and Ti^{4+} ions. y, y' and x are related to the $(Ti^{4+}_{1-x-y}Ti^{3+}_{x}Nb^{5+}_{y})(O^{2-}_{2-y'-z}\square_z N^{3-}_{y'})$ formula.

Table S1 shows the respective atomic ratios of Nb^{5+}, N^{3-}, Ti^{3+} and Ti^{4+} to the total atoms in (N, Nb) co-doped anatase TiO_2 nanocrystals (Columns 2-5). Their atomic ratios to the total cations (*C* in the Table S1) are also listed here in Columns 6-8. For the N-poor co-doped TiO_2, the ratio of Nb^{5+} to total cations (Ti^{4+}+Ti^{3+}+Nb^{5+}) is ~5.4 at.% while that of N^{3-} to total cations is about 3.7 at.%. The doping concentration of N^{3-} ions per $(Ti^{4+}_{1-x-y}Ti^{3+}_{x}Nb^{5+}_{y})(O^{2-}_{2-y'-z}\square_z N^{3-}_{y'})$ formula unit, y', is obviously lower than that of Nb^{5+} ions, y. This sample is thus named as "N-poor". Note that x, y and y' can be determined directly from the above Table S1 while the concentration of oxygen vacancies per formula unit, $z = {}^1/_2\{x - [y-y']\}$, from the requirements of charge balance. Additionally, some Ti^{3+} ions are found in the N-poor samples and the ratio of Ti^{3+} to total cations is calculated to be about 1.7 at.%. For the N-equal co-doped TiO_2, the ratio of Nb^{5+} to total cations is about 5.3 at.% and that of N^{3-} to total cations is about 5.6 at.%. Since the doping concentrations of Nb^{5+} and N^{3-} ions are very close to 1:1, we name them as "N-equal". Similarly, N-rich co-doped TiO_2 has a Nb^{5+} ionic doping concentration of about 5.6 at.% and N^{3-} of about 7.5 at.%. The doping level of N^{3-} is higher than that of Nb^{5+}. We thus name this sample as "N-

rich". In the N-equal and N-rich samples, we do not detect any XPS signal of Ti^{3+}, which are different from the N-poor co-doped TiO_2 samples.

SI-6, TG-DSC and N/O determinator data of N-equal co-doped anatase TiO_2 nanocrystals

Figure S1 shows the TG-DSC curves of N-equal co-doped TiO_2 nanocrystals. It is found that their weight loss below 440 °C is ~13.0 wt.%. Such a substantial loss generally comes from physically/chemically bonded chemicals on the surfaces of the materials.[S5-S8] Above 440 °C, the weight loss becomes less (~1.0 wt.%) and continues till 850 °C. This loss corresponds to the nitrogen concentration of ~6.7 at.% per $(Ti^{4+}_{1-x-y}Ti^{3+}_{x}Nb^{5+}_{y})(O^{2-}_{2-y'-z}\square_{z}N^{3-}_{y'})$ formula unit, supposing that the loss is all from nitrogen in this temperature range. The nitrogen concentration is further estimated by nitrogen/oxygen determinator, by which it is ~5.7 at.% (~0.85 wt.%) per $(Ti^{4+}_{1-x-y}Ti^{3+}_{x}Nb^{5+}_{y})(O^{2-}_{2-y'-z}\square_{z}N^{3-}_{y'})$ formula unit. Note that the three approaches have different principles and measurement environment (vacuum for XPS; flowing air for TG-DSC; Helium gas for N/O determinator). The obtained experimental results for the nitrogen concentrations are reasonably consistent with one another.

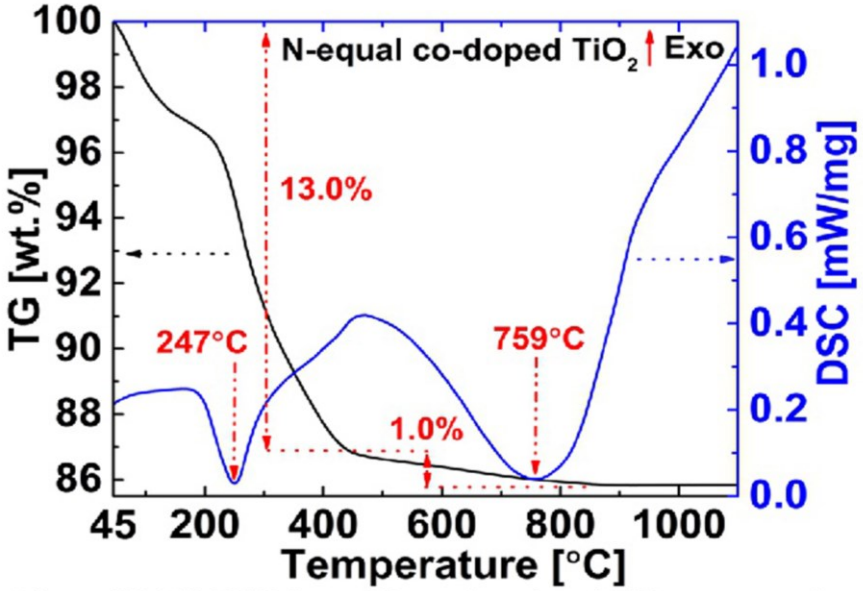

Figure S1. TG-DSC data of N-equal co-doped TiO_2 nanocrystals.

SI-7, FESEM and TEM images of (N, Nb) co-doped anatase TiO_2 nanocrystals

Figure S2 shows that the three N-poor, N-equal and N-rich co-doped TiO_2 nanocrystals synthesized by the solvothermal method have a small particle size of less than 10 nm. From the inserted HRTEM lattice images of Figure S2 (c) and (d), it can be found that the exposed crystal faces of N-poor and N-rich co-doped nanoparticles are both dominated by the (011) and (0-11) facets. Additionally, the (002) crystal faces can also be observed. These results are analogous to that of N-equal co-doped samples shown in the Figure 1 (c) of the main text.

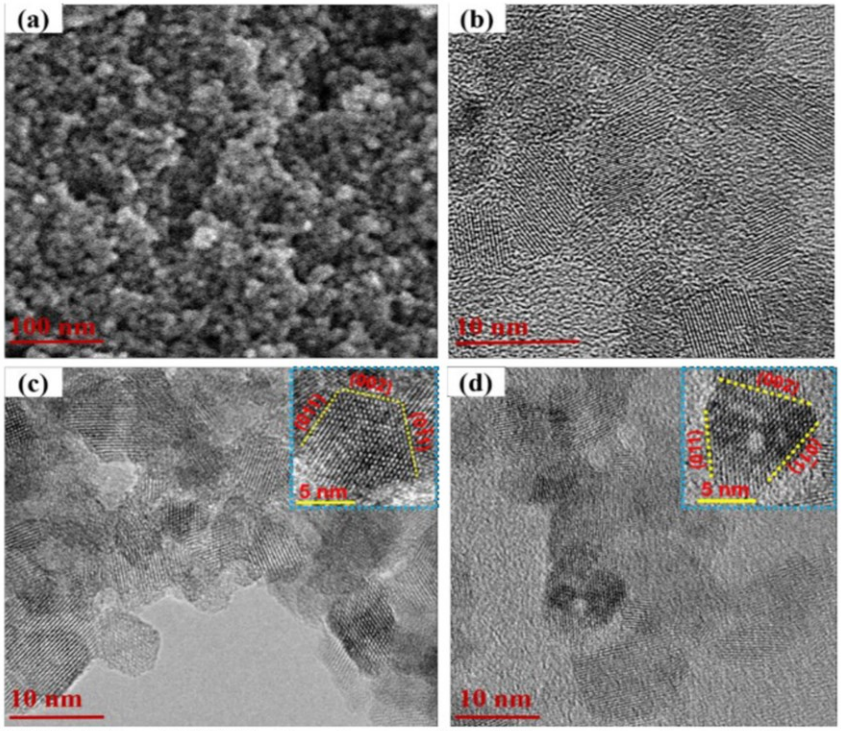

Figure S2. FESEM (a) and TEM lattice images (b) of N-equal co-doped TiO_2 nanocrystals. (c) and (d) are the corresponding TEM lattice images of N-poor and N-rich co-doped TiO_2 nanocrystals, respectively. The insets in (c) and (d) are the related HRTEM lattice images oriented along a <100> direction. The lattice fringes observed correspond to (011), (0-11) and (002), respectively. Note that the nanocrystal facets in each case are also (011), (0-11) and (002), respectively.

SI-8, The average particle size of (N, Nb) co-doped anatase TiO_2 nanocrystals

The Scherrer equation (**Equation S1**)[S9] is used to calculate the average particle size of (N, Nb) co-doped anatase TiO_2 nanocrystals, where the Bragg angles (θ) and the line broadening at half the maximum intensity (β) come from the strongest (101) diffraction peak; D is the average

particle size; λ is the X-ray wavelength of CuKα radiation (0.15418 nm) and K is a dimensionless shape factor (~0.9).

$$D = \frac{K\lambda}{\beta cos\theta} \qquad \text{Equation S1}$$

The calculated results by the Scherrer equation are further compared with that estimated according to their respective TEM lattice images (Figure S2). The below **Table S2** shows their average particle size calculated by the Scherrer equation and estimated from TEM lattice images. It can be found that the average particle size of the three different samples are all less than 10 nm and the achieved results from the two different methods are very close.

Table S2. The average particle size of N-poor, N-equal and N-rich co-doped TiO_2 nanocrystals calculated by the Scherrer equation and estimated from their TEM lattice images.

Samples	XRD Results			TEM Results
(Nb^{5+}+N^{3-}) co-doped TiO_2	2θ [°]	β	D [nm]	D [nm]
N-poor	25.31	1.01	8.1	8.7
N-equal	25.25	1.11	7.3	7.2
N-rich	25.29	1.31	6.3	6.9

SI-9, The specific surface area of (N, Nb) co-doped anatase TiO_2 nanocrystals

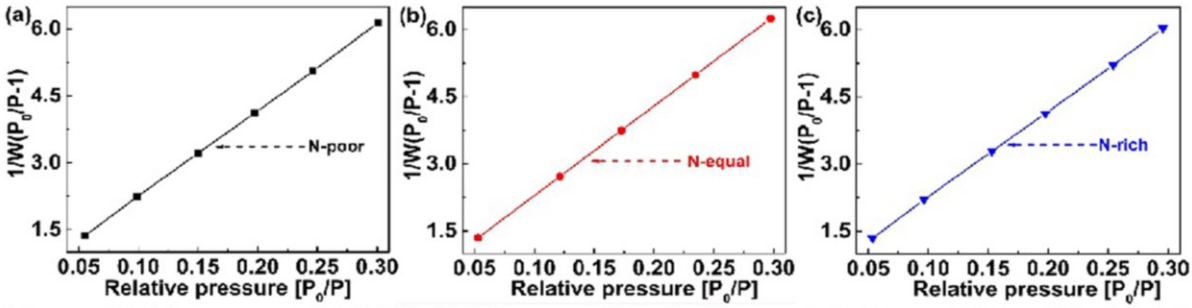

Figure S3. The curves of 1/[W(P_0/P-1)] versus P/P_0 for N-poor (a), N-equal (b) and N-rich (c) co-doped TiO_2 nanocrystals, respectively. They are used to calculate the V_m values and thus further to achieve the specific surface area.

The specific surface area of (N, Nb) co-doped TiO_2 nanocrystals was measured through the Brunauer-Emmett-Teller (B.E.T.) method at liquid nitrogen temperature (~77 K). Their values are calculated through **Equation S2**. In this equation, "*S*" stands for the specific surface area of

samples; "V_m" is the monolayer capacity; " L_{av}" is the Avagadro's number (6.022×10^{23}); A_m is the cross-sectional area (1.62×10^{-19} m^2) and W_t is the molecular weight of N_2 (28.013 g mol^{-1}).

$$S = \frac{(V_m \times L_{av} \times A_M)}{W_t} \qquad \text{Equation S2}$$

In order to calculate the V_m values, the slope and intercept of the $1/[W(P_0/P-1)]$ versus P/P_0 lines in **Figure S3** are fitted and the detailed data are shown in **Table S3.**

Table S3. The respective specific surface area of N-poor, N-equal and N-rich co-doped TiO_2 nanocrystals as well as the related parameters used for the calculation.

Samples	Slope	Intercept	B.E.T. specific surface area [$m^2 g^{-1}$]
N-poor	19.355	0.3036	177.2
N-equal	20.041	0.2853	171.3
N-rich	19.274	0.3264	177.7

The calculated results show that the specific surface area are 177.2, 171.3 and 177.7 $m^2 g^{-1}$ for N-poor, N-equal and N-rich co-doped TiO_2 nanoparticles, respectively (Table S3). The three different (N, Nb) co-doped samples do not have a big difference in terms of the specific surface area.

SI-10, The DFT calculations of possible interstitial nitrogen in (N, Nb) co-doped anatase TiO_2 nanocrystals

In nitrogen monodoped TiO_2, it is widely reported that the nitrogen dopants may occupy interstitial positions, supported by the formation of interstitial N-O species, which can coordinate Ti in a $\eta 2$ fashion through π bond.[36] For the sake of adding completeness to the chemical model describing the seperate case of N-Nb co-doping, we also considered a number of interstitial N doping scenarios to investigate if they could assist in explaining the key experimental features. The calculation procedure used is identical to that described in the main text based on ionic relaxation with GGA-PBE PAW followed by accurate electronic structure calculations using the mBJ potential. For brevity, we do not show all of the results, but merely state that we considered two scenarios: those with and without a compensating oxygen vacancy in the system. It was noted that there was favorable reduction in energy (0.15 eV) gained by

constraining the nitrogen in the general vicinity of Nb, even when the former was in an interstitial position. During ionic relaxation, the cases we examined with the oxygen vacancy in the Nb octahedron showed that nitrogen relaxed into the oxygen vacancy position, effectively simplifying the chemical structure to the high symmetry scenario described in the main text. Given the latter results, where such scenarios with an oxygen vacancy merely favored the same N substitutional model, it is thus not necessary to further discuss the resulting electronic structures since they are identical to those discussed in the main text (Figure 3). However, the scenarios without oxygen vacancies generated a completely distinctive chemical and electronic structure characterized by the formation of N-O species with a short-bond length (1.455-1.472 Å) between a single nitrogen and oxygen. **Figure S4**a and b show two prominent examples of interstitial nitrogen near the equatorial and axial oxygen positions, respectively, of fully-occupied Nb-centered octahedra. In the two cases, the relaxed structure favored the reduction of a unique N-O distance to form an energetically favorable N-O configuration which cannot be easily rationalized on the basis of formal charges within the standard ionic model (*i.e.* it has a covalent character). The severe distortion of the nearby octahedra is a consequence of the awkward nitrogen interstitial location, and this is particularly apparent if one assumes the bonding remains dominated by a metal-oxygen bond. It is noteworthy, however, that the octahedra are barely distorted at all if one assumes a metal-[NO] bond to the average position of the NO species, favoring previous interpretations of significantly complicated electron density around the NO species. Further analysis of the local electronic density is underway, but beyond the scope of the present work. More importantly, **Figure S4**c shows the calculated density of states using the more accurate (but more expensive) mBJ functional to accurately predict the resulting bandgaps. It is immediately clear that the bandgap narrowing caused by the interstitial nitrogen in the [NO] configurations is much weaker (2.82 eV) than the scenarios where N is included substitutionally. Indeed, the latter match the experiment quite well (~2.4 eV) while the scenarios with [NO] species produce an electronic structure that is only weakly

perturbed compared to that of pure anatase (2.98 eV). We interpret this as a strong indicator that direct charge-transfer bonding between the N-Nb species is a prerequisite for enhanced photocatalytic performance.

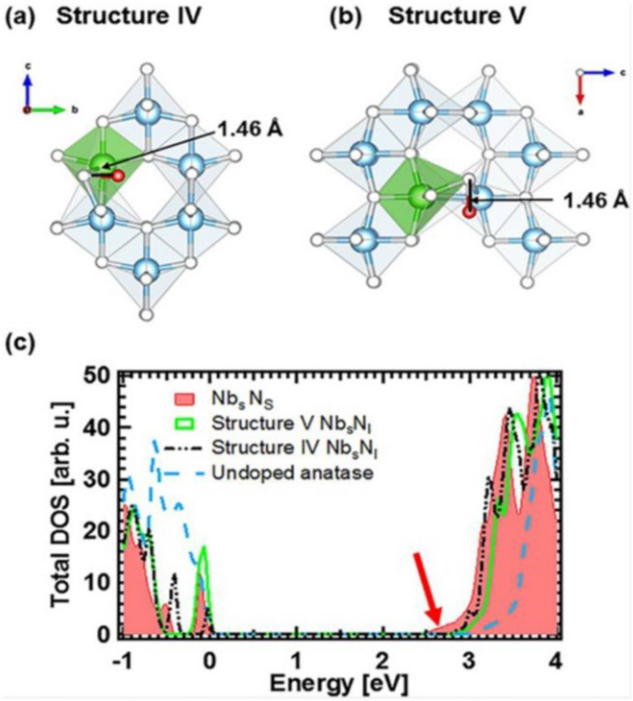

Figure S4. (a) Structure IV consists of a nitrogen positioned interstitially forming a N-O species connected with an oxygen in the equatorial position of the fully-occupied Nb-centered octahedron in the anatase structure. The black line highlights the short N-O bond formed with a single oxygen (1.46 Å). (b) Interstitially positioned nitrogen forming a N-O species with an oxygen at axial position. The green regions highlights the Nb-O octahedron which is distorted by the presence of nitrogen species under the assumption of conventional cation-anion bonding. (c) Total density of states for the case of substitutional Nb and N (Nb_SN_s) compared to that of un-doped anatase (dotted line) and scenarios with interstitial nitrogen near the equatorial/axial positions in Structure IV and V. The red arrow indicates the states introduced by the significant narrowing of bandgaps (~2.4 eV) which only occurs for the substitutional N.

References

[S1] P. E. Blöchl, *Phys. Rev. B* **1994**, *50*, 17953.

[S2] J. P. Perdew, K. Burke, M. Ernzerhof, *Phys. Rev. Lett.* **1996**, *77*, 3865.

[S3] G. Kresse, J. Furthmüller, *Comput. Mater. Sci.* **1996**, *6*, 15.

[S4] G. Kresse, J. Furthmüller, *Phy. Rev. B* **1996**, *54*, 11169.

[S5] C. Wang, Q. Li, R. -D. Wang, *Mater. Lett.* 2004, *58*, 1424.

[S6] S. Janitabar-Darzi, A. R. Mahjoub, A. Nilchi, *Physica E* **2009**, *42*, 176.

[S7] R. -A. Doong, S. -M. Chang, Y. -C Hunga, I. -L. Kao, *Sep. and Purifi. Technol.* **2007**, *58*, 192.

[S8] M. H. Habibin, R. Mokhtari, *J. Therm. Anal. Calorim.* **2013**, *112*, 1179.

[S9] A. Folli, I. Pochard, A. Nonat, U. H. Jakobsen, A. M. Shepherd, D. E. Macpheez, *J. Am. Ceram. Soc.* **2010**, *93*, 3360.

3.2 Trans-regime structural transition of (In^{3+}+Nb^{5+}) co-doped anatase TiO_2 nanocrystals under high pressure

I wrote the draft of this paper. I synthesized the (In^{3+}+Nb^{5+}) co-doped anatase TiO_2 nanocrystals and designed high pressure reaction experiments. I characterized the related samples using XRD, Raman spectroscopy, ICP-OES, HRTEM, SEM/EDS, XPS and others. I also analyzed the related results of DFT calculations performed by Terry J. Frankcombe and conducted high pressure reaction experiments with Larissa Q. Huston.

CRYSTAL GROWTH & DESIGN

Article

pubs.acs.org/crystal

Trans-Regime Structural Transition of (In^{3+} + Nb^{5+}) Co-Doped Anatase TiO_2 Nanocrystals under High Pressure

Qingbo Sun,[†] Larissa Q. Huston,[‡] Terry J. Frankcombe,[§] Jodie E. Bradby,[‡] Teng Lu,[†] Dehong Yu,[∥] Chao Zhou,[⊥] Zhenxiao Fu,[⊥] and Yun Liu*[,†]

[†]Research School of Chemistry and [‡]Research School of Physics and Engineering, the Australian National University, Canberra, Australian Capital Territory, 2601, Australia

[§]School of Physical, Environmental and Mathematical Sciences, University of New South Wales, Canberra, Australian Capital Territory, 2601, Australia

[∥]Australian Nuclear Science and Technology Organisation, Lucas Height, New South Wales, 2234, Australia

[⊥]Fenghua Advanced Technology Holding Co., Ltd., Zhaoqing, Guangdong, 526020, China

S *Supporting Information*

ABSTRACT: Chemical co-doping and high pressure reactions have been broadly used to synthesize novel materials or to tune the physicochemical properties of traditional materials. Here, we take In^{3+} and Nb^{5+} ions co-doped anatase TiO_2 nanocrystals as an example and report that a combination of both a chemical and a high pressure reaction route is more powerful for the preparation of metastable polymorphs. It is experimentally demonstrated that In^{3+} and Nb^{5+} co-doping significantly changes the high-pressure reaction behaviors of anatase TiO_2 nanocrystals (<10 nm) and leads to their trans-regime structural transition in terms of in situ Raman analysis, from an anatase to a baddeleyite-like phase under compressive pressures and then to an α-PbO_2-like structure under decompressive pressures. This abnormal phase transition is attributed to a defect-induced heterogeneous nucleation mechanism. Furthermore, the stiffness of co-doped TiO_2 nanocrystals is significantly enhanced due to the synergistic effects of co-dopants. This research not only proposes a potentially effective strategy to synthesize co-doped metastable polymorphic phases but also suggests one feasible method to improve the mechanical properties of anatase TiO_2 nanocrystals.

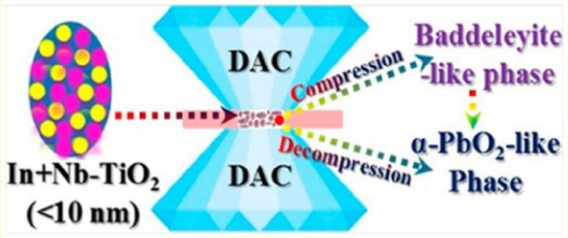

INTRODUCTION

Many traditional materials display abnormal physical behaviors under or after high pressure (HP) reactions as a consequence of the shrinkage of average interatomic distances and the densification of atomic/ionic packing. For example, pressurized titanium dioxide (TiO_2) can achieve ultrahardness comparable to diamond or cubic BN.[1−3] The band gap of TiO_2 can be narrowed to greatly improve photoreaction activity after HP treatment.[4,5] The superconductivity of Fe-based superconductors (e.g., $CaFe_2As_2$ or $BaFe_2As_2$) can also be controlled by applied pressure.[6,7] The HP reaction is thus not only a valid way to discover novel properties of normal materials but also a critical approach to synthesize new materials with higher coordination numbers.[8]

TiO_2 is a typical multiple polymorphic example and is now extensively used in the fields of photocatalysts, solar cells, cosmetics, and electronic devices. Anatase, rutile, and brookite are its three common phases and can be synthesized at ambient conditions. Other polymorphs of TiO_2 such as a baddeleyite-like structure or α-PbO_2-like phase can only be prepared under tens of gigapascals (GPa) pressures.[9−16] The hexagonal Fe_2P-type, fluorite and pyrite structures are either predicted theoretically or only observed under extreme HP conditions.[17−20] Previous HP investigations suggested that the structural transition of anatase TiO_2 was strongly dependent on its initial crystallite sizes, and smaller crystals kept anatase stable to higher pressures. Figure 1 shows the size-dependent compression and decompression phase diagrams of anatase TiO_2, summarized from the literature.[9−24] Three size regimes (<11 nm, 11−40 nm, and >40 nm) are categorized. (1) For those small nanocrystals with crystallite sizes less than 11 nm, pressurization-induced amorphization occurs at ∼24 GPa due to the crystal−liquid transformation. On depressurization, the HP disordered phase changes at ∼15 GPa from a high-density amorphous state (HDA) to a low-density amorphous structure (LDA). (2) For TiO_2 nanocrystals with crystallite sizes between 11 and 40 nm, a direct phase transformation from anatase to a monoclinic baddeleyite-like structure happens during compression at ∼16 GPa. This HP-induced baddeleyite-like structure then changes to an α-PbO_2-like phase at ∼10.5 GPa when the

Received: January 12, 2017
Revised: February 27, 2017
Published: March 27, 2017

DOI: 10.1021/acs.cgd.7b00055
Cryst. Growth Des. 2017, 17, 2529−2535

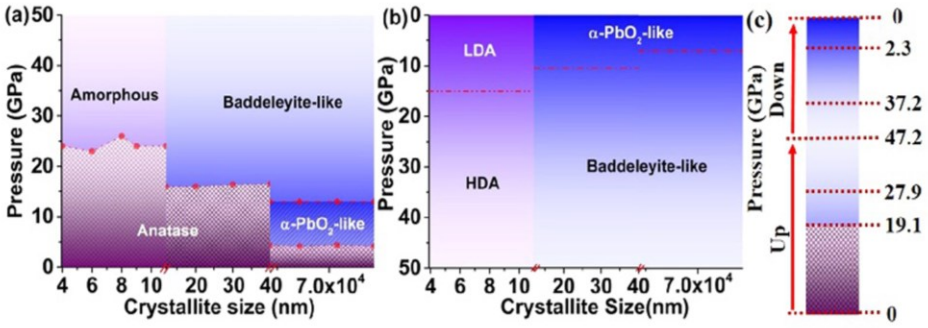

Figure 1. Size-dependent compression (a) and decompression (b) phase diagrams of undoped anatase TiO_2.[9−24] Three size regimes can be categorized. The dotted lines label the boundary of onset structural transition. H (L) DA means a high (low)-density amorphous state. (c) The structural transition of (5 atom % In^{3+} + 5 atom % Nb^{5+}) co-doped anatase TiO_2 nanocrystals (<10 nm) under pressurization (pressure up) and depressurization (pressure down) conditions.

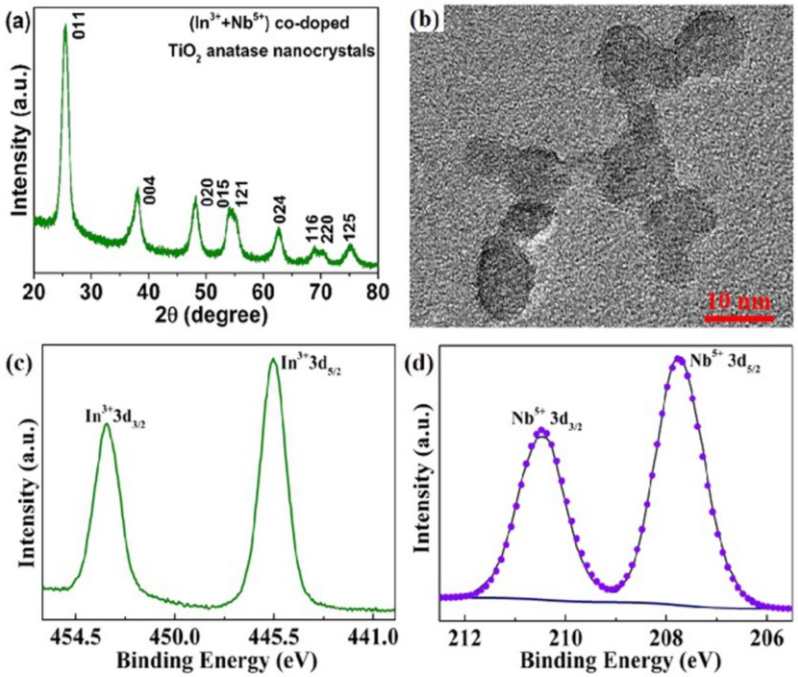

Figure 2. PXRD pattern (a), HRTEM image (b), and XPS data (c and d) of (5 atom % In^{3+} + 5 atom % Nb^{5+}) co-doped anatase TiO_2 nanocrystals used for high pressure reaction, indicating that they have In^{3+} and Nb^{5+} doped ions, anatase structure, quasi-spherical morphology as well as uniform size distribution of less than ~10 nm.

pressure is gradually released. (3) For TiO_2 nanocrystals with crystallite sizes over 40 nm, they transform from anatase to an α-PbO_2-like phase at ~4.5 GPa and then to a baddeleyite-like structure at ~13 GPa during compression. Similar to the 11−40 nm nanocrystals, the baddeleyite-like structure also becomes an α-PbO_2-like phase after decompression, but starts at a lower onset pressure of ~7 GPa. After the whole compression and decompression cycle, the anatase structure of TiO_2 cannot be recovered. The pressure values, which are applied on micro-/nanoparticles with a similar size range for structural transition, remain almost unchanged between two successive phases except for a small fluctuation caused by the pressure calibration method, the transmitting medium, or the original properties of anatase TiO_2.

Doping foreign ions/atoms into the crystal structures of host materials inevitably affects their macroscopic properties as it strategically changes the chemical environment of doped sites and thus varies structural stability. Some dopants (e.g., Mn in ZnO nanowires[25] or Sc/Y in AlN nanoprisms[26]) drastically reduce the onset formation pressure of related new polymorphs, while other dopants such as Mg in lanthanum silicate[27] significantly elevate the critical pressure of phase transition. Our recent study indicated that co-doping In^{3+} and Nb^{5+} ions introduced defect clusters into rutile TiO_2 and thus enabled the localization of electrons in certain regions through creating electron pinned defect dipoles for colossal permittivity.[28] Given the complicated pressure-induced phase transition scenarios of anatase TiO_2, the simultaneous introduction of In^{3+} and Nb^{5+} ions into their crystal structures might also affect high pressure reaction dynamics and possibly generate special polymorphs of co-doped TiO_2. Moreover, the ionic radius of In^{3+} ions is significantly larger than that of host Ti^{4+} ions. The introduction of large-size dopants would result in the great distortion of the local crystal structure and thus change the

DOI: 10.1021/acs.cgd.7b00055
Cryst. Growth Des. 2017, 17, 2529−2535

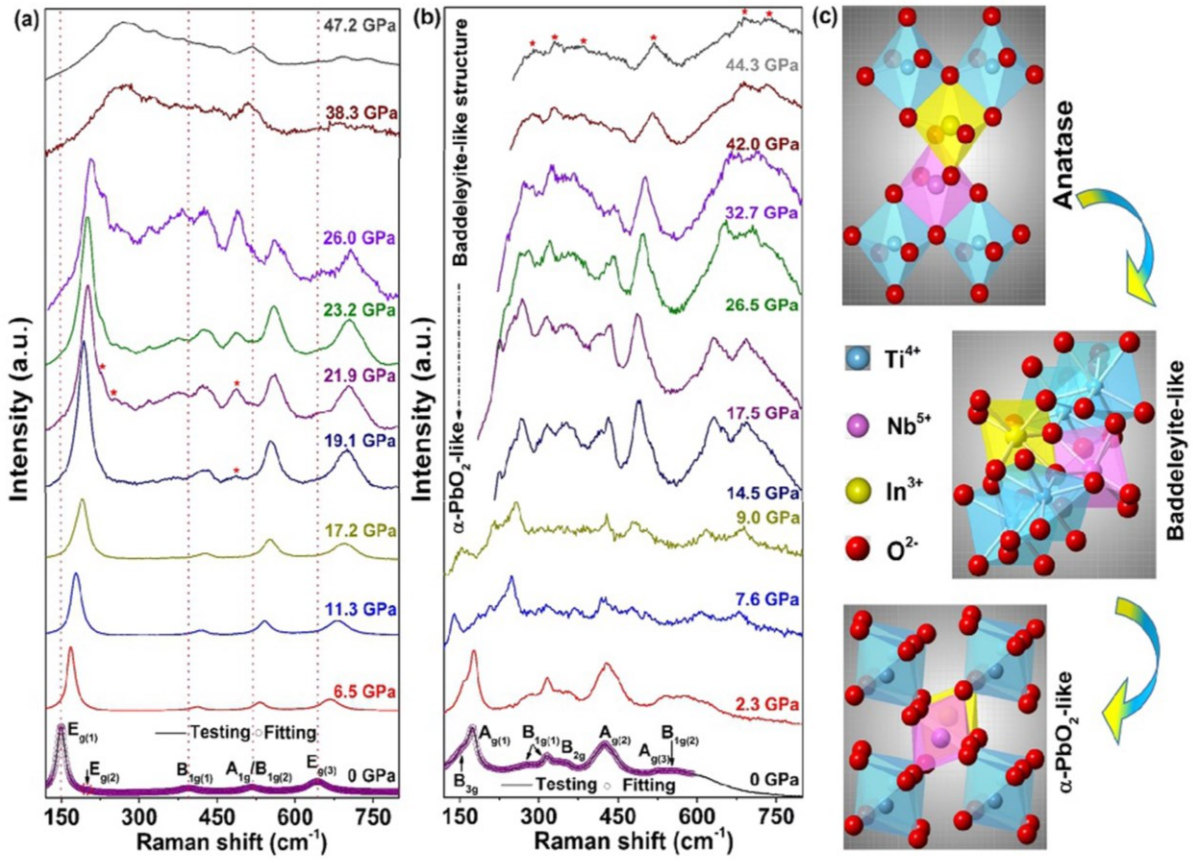

Figure 3. Raman spectra of (5 atom % In^{3+} + 5 atom % Nb^{5+}) co-doped anatase TiO_2 nanocrystals collected under compression (a) and decompression (b) conditions. Their crystallographic evolution followed the sequence of anatase → baddeleyite-like phase (compression) → α-PbO_2-like structure (decompression). (c) Polyhedral structures of three co-doped TiO_2 polymorphs obtained in this work.

stiffness of host TiO_2 materials in a similar way to the well-known Y stabilized ZrO_2. Here, we experimentally design an effective approach to cooperatively introduce In^{3+} and Nb^{5+} ions (~5 atom %, compared to titanium ions) into small anatase TiO_2 nanocrystals (<10 nm). High pressure reaction behavior of co-doped nanocrystals is systematically investigated by in situ Raman spectroscopy. The enhanced stiffness (incompressibility) by co-doping is analyzed, and the associated mechanism for the abnormal structural transition behavior is also discussed based on defect-induced heterogeneous nucleation mechanism.

■ EXPERIMENTAL SECTION

Materials. (In^{3+} + Nb^{5+}) co-doped anatase TiO_2 nanocrystals were synthesized by a solvothermal method and were directly used for high pressure reactions. Detailed information about the preparation of these co-doped nanocrystals is described elsewhere.[29]

High Pressure Process. A diamond anvil cell with a cullet size of 400 μm was employed to conduct the high pressure reaction. A steel gasket of 30 μm in thickness was drilled at the center to form a 200 μm diameter hole. It served as the sample chamber. (In^{3+} + Nb^{5+}) co-doped anatase TiO_2 nanopowders and two small ruby balls were loaded into the above chamber. A mixture of ethanol and methanol (4:1) were used as a pressure transmitting medium. Samples were carefully loaded to the maximum pressure of 47.2 GPa in small steps.

Characterization Methods. Powder X-ray diffraction patterns (PXRD) were collected by PANalytical's X-ray diffractometers with Cu Kα radiation (λ = 1.5406 Å). A field-emission transmission electron microscope (TEM, JEOL-2100F) was utilized to analyze their microscopic morphology and crystallite sizes. The chemical valences and doping levels of In^{3+} and Nb^{5+} ions were analyzed by X-ray photoelectron spectroscopy (XPS), energy dispersive spectroscopy (EDS) of scanning electron microscope (SEM), and inductively coupled plasma optical emission spectrometer (ICP-OES). The pressure inside the diamond cell was determined by the pressure dependent shift of the ruby fluorescence R_1 line.[30] In situ Raman measurement was taken using a Renishaw Raman System (532 nm laser).

■ RESULTS AND DISCUSSION

Figure 2a shows the PXRD pattern of solvothermal products. All diffraction peaks are assigned to the tetragonal phase with space group symmetry $I4_1/amd$. We experimentally demonstrate the nature of pure anatase phase for the synthesized solvothermal products. Their crystallite size is estimated to be about 6.8 nm according to the calculation using the Scherrer equation[31] and further confirmed by the direct observation from a high resolution TEM image (ranging from 4.7 nm to 10.8 nm and having an average crystallite size of ~6.4 nm, Figure 2b). Moreover, most of the co-doped TiO_2 nanocrystals present a quasi-spherical shape. The respective chemical valences of indium and niobium in the quasi-spherical nanoparticles are +3 and +5, respectively, and that of titanium are composed of +3 and +4, as shown by XPS analysis (Figure 2c,d). The total doping concentration of In^{3+} (In/Ti) and Nb^{5+} ions (Nb/Ti) is found to be very close to ~10 atom %, and their individual one is ~5 atom % in terms of the results of

DOI: 10.1021/acs.cgd.7b00055
Cryst. Growth Des. 2017, 17, 2529−2535

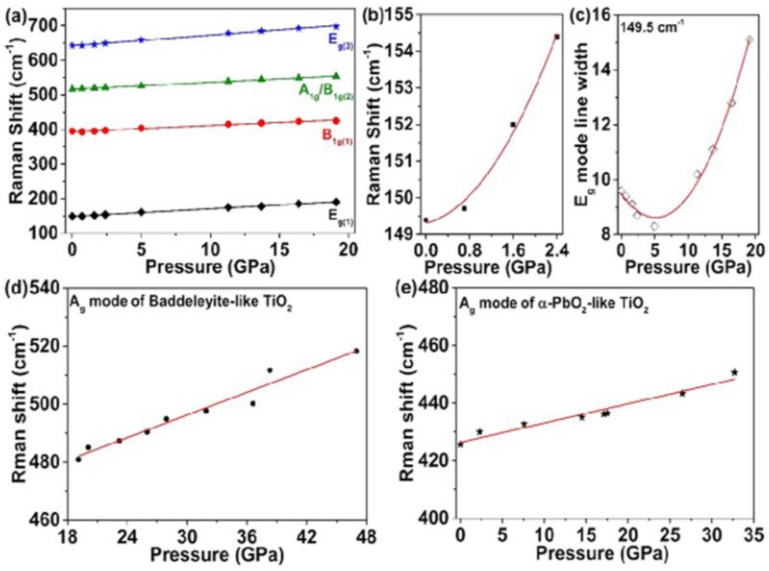

Figure 4. Raman frequencies of different active modes as a function of compression or decompression pressure for co-doped anatase (a), baddeleyite-like (d), and α-PbO_2-like (e) nanocrystals. (b) Enlarged pressure-Raman frequency curve of $E_{g(1)}$ mode of co-doped anatase TiO_2 nanocrystals at lower pressures (<2.4 GPa). (c) Pressure-dependent Raman line width of $E_{g(1)}$ mode of co-doped anatase TiO_2 nanocrystals. The experimental data were labeled by different symbols, while the linear fitting data were labeled by the solid lines.

XPS, EDS of SEM, and ICP-OES measurement (Supporting Information, Table S1). It is thus claimed that the (In^{3+} + Nb^{5+}) co-doped TiO_2 nanocrystals used as HP reactants of this work have the respective doping concentration of 5 atom %, anatase phase, quasi-spherical morphology, and the average crystallite sizes of less than 10 nm.

To investigate the high pressure reaction behavior of (In^{3+} + Nb^{5+}) co-doped anatase TiO_2 nanocrystals, their Raman spectra were collected in situ under compression and decompression conditions. Tetragonal anatase TiO_2 normally has six Raman active modes ($1A_{1g}$ + $2B_{1g}$ + $3E_g$).[32,33] Only five of them are detected here when fitting the room temperature and ambient Raman spectrum (0 GPa curve of Figure 3a). Three Raman bands around 149.5, 199.6, and 642.4 cm^{-1} are assigned to different E_g modes, while the other two peaks centering at 394.3 and 516.4 cm^{-1} are ascribed to the B_{1g} and A_{1g}/B_{1g} active modes. The Raman signal at 199.6 cm^{-1} is very weak, and two different modes (A_{1g} or B_{1g}) at 516.4 cm^{-1} cannot be distinguished unambiguously. These phenomena are common for nanoscale TiO_2 and are caused by their strong size effects.[34,35]

When the achieved co-doped anatase TiO_2 nanocrystals are gradually pressurized to 47.2 GPa in a diamond anvil cell, the shift of Raman peaks and the detailed process for forming a baddeleyite-like phase are observed. Below 19.1 GPa, the four prominent Raman peaks of co-doped TiO_2 all shift to higher wavenumbers with increasing pressures. Above 19.1 GPa, a typical A_g mode of baddeleyite-like TiO_2 begins to appear at 480.2 cm^{-1} (it is labeled by a "*" symbol). This onset pressure for phase transition is much lower than that of undoped TiO_2 with similar crystal sizes (~24 GPa, Figure 1), but is slightly higher than that of Nb^{5+} single-doped anatase nanoparticles (~18 GPa).[36] Further increasing the external pressures, the A_g peak intensity at 480.2 cm^{-1} continuously increases, and the other Raman peaks of baddeleyite-like TiO_2 become more prominent (see the Raman spectra collected at, e.g., 21.9 and 26.0 GPa). It suggests a gradual phase transition from anatase to a baddeleyite-like structure with these two phases coexisting in the transitional region. At ~ 27.9 GPa, the baddeleyite-like phase completely forms and remains stable up to the maximum pressure (47.2 GPa, Supporting Information, Figure S1). Comparing with the amorphization of undoped anatese TiO_2 nanocrystals with a similar size distribution (Figure 1), the phase transition behavior of co-doped anatese TiO_2 is significantly changed due to the introduction of In^{3+} and Nb^{5+} ions.

The formed baddeleyite-like structure can only exist under HP conditions. It gradually changes to an α-PbO_2-like phase when the pressure is reduced to 32.7 GPa (i.e., the Raman peak of an α-PbO_2-like phase appears at ~446.8 cm^{-1}, Figure 3b). The phase transition from a baddeleyite-like to an α-PbO_2-like structure completes at ~2.3 GPa, and then the α-PbO_2-like structure remains stable even when the pressure is completely released. The co-doped α-PbO_2-like TiO_2 synthesized thereof shows $3A_g$ (175.3, 426.1, and 531.9 cm^{-1}), $3B_{1g}$ (280.6, 317.0, and 567.3 cm^{-1}), $1B_{2g}$ (346.2 cm^{-1}), and $1B_{3g}$ (156.0 cm^{-1}) Raman active modes.

For one compression and decompression cycle, (In^{3+} + Nb^{5+}) co-doped anatase TiO_2 nanocrystals experience the phase transition in the sequence of (1) anatase → baddeleyite-like phase (compression) → α-PbO_2-like structure (decompression, Figure 3c). This structural transition scenario differs from the pressure-induced amorphization of undoped TiO_2 nanoparticles with the similar crystallite sizes (<11 nm), but is more closely analogous to that of large-sized ones (11−40 nm, Figure 1). Trans-regime structural transition is thus activated by co-doping In^{3+} and Nb^{5+} ions.

From a structural perspective, anatase and α-PbO_2-like TiO_2 are both composed of TiO_6 octahedra. The octahedral arrangements, however, are quite different between them (Figure 3c). TiO_6 octahedra form zigzag chains along *a* and *b* directions, and each octahedron shares four edges in anatase TiO_2 while they form the planar chains sharing edges in a zigzag arrangement along the *c* direction in an α-PbO_2-like

DOI: 10.1021/acs.cgd.7b00055
Cryst. Growth Des. 2017, 17, 2529−2535

Table 1. Pressure Coefficients ($d\nu/dp$) of Different Raman Active Modes of (In^{3+} + Nb^{5+}) Codoped, Nb^{5+} Single-Doped and Undoped Anatase, Baddeleyite-like, α-PbO_2-like TiO_2 Nanocrystals

crystal structures	Raman modes	$d\nu/dp$ ($cm^{-1}\cdot GPa^{-1}$)	samples	references
anatase	E_g (149.5 cm^{-1})	2.20 (±0.05)	5 atom % In^{3+} + 5 atom % Nb^{5+}	this work
		2.58 (±0.22)	undoped	ref 12
		2.81	(10 atom % Nb^{5+}) single-doped	ref 36
	B_{1g} (394.3 cm^{-1})	1.76 (±0.08)	5 atom % In^{3+} + 5 atom % Nb^{5+}	this work
		2.7	undoped	ref 23
		~2.8	(10 atom % Nb^{5+}) single-doped	ref 36
	A_{1g}/B_{1g} (516.4 cm^{-1})	1.98 (±0.03)	5 atom % In^{3+} + 5 atom % Nb^{5+}	this work
		2.7	undoped	ref 23
		~2.6	(10 atom % Nb^{5+}) single-doped	ref 36
	E_g (642.4 cm^{-1})	3.03 (±0.09)	5 atom % In^{3+}+5 atom % Nb^{5+}	this work
		3.1	undoped	ref 23
		~4.2	(10 atom % Nb^{5+}) single-doped	ref 36
baddeleyite	A_g (480.2 cm^{-1})	1.30 (±0.10)	5 atom % In^{3+} + 5 atom % Nb^{5+}	this work
		1.65 (±0.21)	undoped	ref 12
α-PbO_2	A_g (426.1 cm^{-1})	0.67 (±0.06)	5 atom % In^{3+} + 5 atom % Nb^{5+}	this work
		~3.1	(5 atom % Nb^{5+}) single-doped	ref 36

crystal structure.[20] Meanwhile, the baddeleyite-like phase is constructed by TiO_7 decahedra, and the coordination number of Ti^{4+} cations also changes from six to seven. Hence, the structural transition of (In^{3+} + Nb^{5+}) co-doped anatase TiO_2 nanocrystals is complicated under HP conditions and accompanied by the breaking and reassembling of M−O chemical bonds (M represents In, Nb, and Ti ions and O is oxygen).

In order to quantatively describe the shift of Raman peaks, pressure (p) dependent Raman frequency (ν) is plotted and fitted for different active modes of co-doped TiO_2 nanocrystals (Figure 4a,d,e). The pressure coefficient ($d\nu/dp$) is about 2.20 $cm^{-1}\cdot GPa^{-1}$ for the $E_{g(1)}$ Raman mode of co-doped anatase TiO_2. It is about 12% lower than that of undoped (2.58 ± 0.22 $cm^{-1}\cdot GPa^{-1}$)[12] and about 22% smaller than that of 10 atom % Nb^{5+} single-doped TiO_2 (2.81 $cm^{-1}\cdot GPa^{-1}$),[36] meaning that M−O chemical bonds of co-doped nanocrystals are more incompressible than the latter two samples. The $d\nu/dp$ values of other Raman modes are also lower and present similar trends as that of $E_{g(1)}$ mode. Table 1 summarizes the pressure coefficients of (In^{3+} + Nb^{5+}) co-doped/Nb^{5+} single-doped/undoped anatase, baddeleyite-like and α-PbO_2-like TiO_2 nanocrystals. It is obvious that Nb^{5+} ions single-doping results in larger $d\nu/dp$ values and actually softens anatase TiO_2 nanoparticles.[36] However, In^{3+} and Nb^{5+} co-doping leads to an opposite variation and should harden their co-doped nanocrystals (i.e., enhancing their stiffness).[10,13,16] In addition, we also find a small dip in the enlarged pressure-Raman frequency curve of below 0.8 GPa (Figure 4b) due to the pressure difference between interior and exterior of co-doped TiO_2 nanoparticles.[10,12] This pressure difference further results in a steep decrement and then a continuous increment of Raman line widths on both sides of ~5 GPa (Figure 4c).

The stiffening of co-doped TiO_2 nanocrystals should be physically attributed to the synergic effects of In^{3+} and Nb^{5+} co-dopants. The Pauling ionic radii of In^{3+} ions are 94 pm in the six-coordinated octahedra and are much larger than that of Ti^{4+} (74.5 pm) or Nb^{5+} (78 pm) ions. Bond-valence-sum (BVS) calculations[37−39] show that In^{3+} ions (5 atom %) are strongly overbonded in anatase TiO_2 with the global instability index (GII) of 1.2402 v.u., while Nb^{5+} ions (5 atom %) are slightly overbonded with GII = 0.3540 v.u. In−O chemical bonds become more incompressible than Ti−O or Nb−O bonds due to the large-size of overbonded In^{3+} ions and thus leads to the enhanced stiffness of co-doped TiO_2. However, the mono-doping level of In^{3+} ions in TiO_2 is very low and usually less than 1 atom %, which is impossible to achieve 5 atom % without phase segregation.[40] Nb^{5+} ions co-doping thus prompts the dissolution of In^{3+} ions and their associated synergistic effects enhance the stiffness of anatase nanocrystals. On the basis of (In^{3+} + Nb^{5+}) co-doped bulk crystals, density functional theory (DFT) calculations were performed (Supporting Information, S3). The results show that co-doped bulk crystals become soft and are contrary to that of nanocrystals since three-dimensional (3D) confinement of finite-sized nanoparticles cannot be considered for the DFT calculations.

The synergistic effects of In^{3+} and Nb^{5+} ions also determine the trans-regime structural transition of co-doped nanocrystals under HP conditions. Doping introduces different defect states into host materials, and these intentionally introduced defects can act as heterogeneous nucleation centers of crystal−crystal transition.[41−43] Classical nucleation theory points out that the energy barrier (ΔG^*) of heterogeneous nucleation is always lower than that of homogeneous nucleation. It is thus energically favorable to activate the structural transition of co-doped TiO_2 nanoparticles using a smaller pressure than that of undoped TiO_2. Experimentally, the critical pressure of phase transition from anatase to a baddeleyite-like structure is ~19.1 GPa, which is much lower than that of undoped samples (~24 GPa). During decompression, similar results can also be obtained. Therefore, defect-induced heterogeneous nucleation mechanism is responsible for the observed trans-regime structural transition of co-doped nanocrystals.

Figure 5 shows a schematic of defect-induced heterogeneous nucleation mechanism. Crystal fields and chemical bonds around In^{3+} and Nb^{5+} co-doped sites are different from that of titanium and result in a nonuniform pressure distribution within co-doped TiO_2 nanoparticles under HP conditions. Locally, the crystal structure surrounding doped sites first distorts because the defect positions have higher energy. In−O or Nb−O chemical bonds then break down and reassemble into the basic MO_7 units of a baddelyite-like structure. During this process, the introduced defects through co-doping In^{3+} and Nb^{5+} ions serve as the nucleation centers of new polymorphs.

DOI: 10.1021/acs.cgd.7b00055
Cryst. Growth Des. 2017, 17, 2529−2535

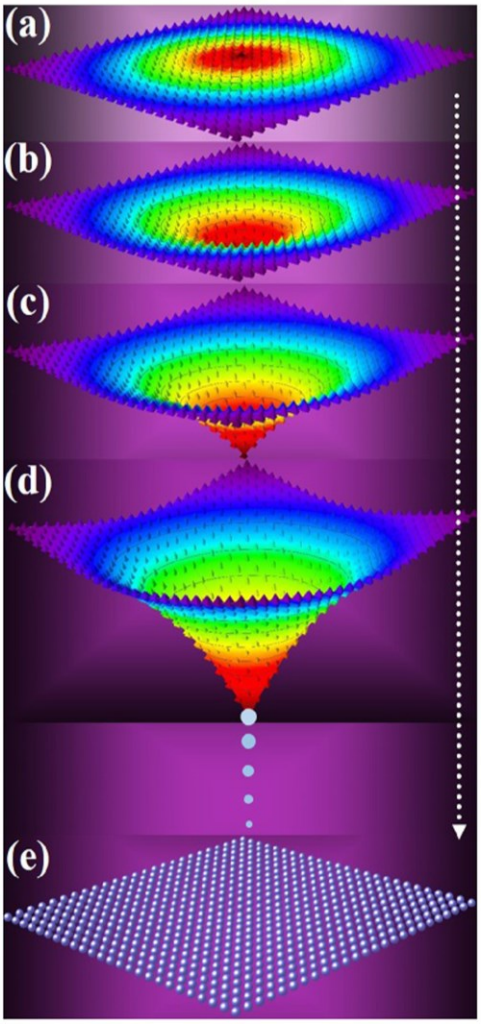

Figure 5. A schematic of the defect-induced heterogeneous nucleation mechanism. (a) Nonuniform pressure distribution among MO_6 octahedra due to their different local crystal chemistry environments (the red color represents the position of defect induced by co-doping). (b, c) Distortion of local crystal structure under high pressure. (d) The formation of crystal nuclei of new phase after the breaking and reassembling of In−O, Nb−O chemical bonds. (e) The growth of new crystal nuclei into co-doped baddeleyite-like or α-PbO_2-like TiO_2 nanocrystals.

Once the crystal nuclei are shaped, they consume other smaller ones and gradually grow into nanoparticles following the Ostwald ripening process until all co-doped anatase TiO_2 changes to a baddelyite-like phase. This crystal growth process is supported by the appearance of NbO nanoclusters during the phase transition of Nb^{5+} single-doped TiO_2 nanoparticles from anatase to rutile,[41] and it is also supported by a study on the preparation of silicon nanoparticles.[44] A similar scenario also happens in the phase transition from a baddeleyite-like to an α-PbO_2-like structure. However, it should be pointed out that the driving force for phase transition at the compression stage is quite different from that of decompression process. The former comes from the external pressure, while the latter is from the interiors of nanoparticles.

CONCLUSION

High pressure reaction behaviors of (In^{3+} + Nb^{5+}) co-doped anatase TiO_2 nanocrystals (<10 nm) were investigated by in situ Raman spectroscopy. In^{3+} and Nb^{5+} ions co-doping not only induces trans-regime structural transition of anatase TiO_2 nanocrystals but also enhances their stiffness or incompressibility due to the synergistic effects of co-dopants. The crystallographic evolution of co-doped TiO_2 is demonstrated to follow the sequence of anatase to a baddeleyite-like phase (under compression) and then to an α-PbO_2-like structure (under decompression). This abnormal trans-tregime structural transition is determined by a defect-induced heterogeneous nucleation mechanism. The combination of high pressure and co-doping strategy is thus critical for the synthesis of other co-doped metastable polymorphic nanomaterials, and it is also significant to optimize the physicochemical properties of traditional materials.

ASSOCIATED CONTENT

Supporting Information

The Supporting Information is available free of charge on the ACS Publications website at DOI: 10.1021/acs.cgd.7b00055.

Table S1, the doping concentration of In^{3+} and Nb^{5+} ions in co-doped anatase TiO_2 nanocrystals; Figure S1. Raman spectrum of (In^{3+} + Nb^{5+}) co-doped anatase TiO_2 nanocrystals; SI-3. Density functional theory (PDF)

AUTHOR INFORMATION

Corresponding Author

*E-mail: Yun.liu@anu.edu.au.

ORCID

Qingbo Sun: 0000-0003-3546-0018
Terry J. Frankcombe: 0000-0001-9791-5394
Yun Liu: 0000-0002-5404-3909

Author Contributions

Q.S., Y.L., L.Q.H., J.E.B., and T.J.F. made the main contribution to the preparation of this manuscript. Y.L. initiated this research, and planned and coordinated all experimental and theoretical work. Q.S. synthesized the nanopowders. Q.S. and L.Q.H. designed high pressure reaction experiments with the supervision of J.E.B. T.J.F. performed the theoretical work collaborated with Y.L., Q.S., T.L., D.Y. conducted HRTEM, SEM/EDS, XPS analysis with the collaboration of C.Z. and Z.F. All authors were involved in the data analysis and discussion as well as the manuscript preparation.

Notes

The authors declare no competing financial interest.

REFERENCES

(1) McMillan, P. F. *Chem. Soc. Rev.* **2006**, *35*, 855−857.
(2) McMillan, P. F. *Nat. Mater.* **2002**, *1*, 19−25.
(3) Sato, H.; Endo, S.; Sugiyama, M.; Kikegawa, T.; Shimomura, O.; Kusaba, K. *Science* **1991**, *251*, 786−788.
(4) Carini, G., Jr.; Parrino, F.; Palmisano, G.; Scandura, G.; Citro, I.; Calogero, G.; Bartolotta, A.; Di Marco, G. *Photochem. Photobiol. Sci.* **2015**, *14*, 1685−1693.
(5) Kuo, M.-Y.; Chen, C.-L.; Hua, C.-Y.; Yang, H.-C.; Shen, P. *J. Phys. Chem. B* **2005**, *109*, 8693−8700.
(6) Kimber, S. A. J.; Kreyssig, A.; Zhang, Y.-Z.; Jeschke, H. O.; Valentí, R.; Yokaichiya, F.; Colombier, E.; Yan, J.; Hansen, T. C.;

DOI: 10.1021/acs.cgd.7b00055
Cryst. Growth Des. 2017, 17, 2529−2535

Chatterji, T.; McQueeney, R. J.; Canfield, P. C.; Goldman, A. I.; Argyriou, D. N. *Nat. Mater.* **2009**, *8*, 471−475.
(7) Torikachvili, M. S.; Bud'ko, S. L.; Ni, N.; Canfield, P. C. *Phys. Rev. Lett.* **2008**, *101*, 057006.
(8) San-Miguel, A. *Chem. Soc. Rev.* **2006**, *35*, 876−889.
(9) Cai, Y.; Zhang, C.; Feng, Y. P. *Phys. Rev. B: Condens. Matter Mater. Phys.* **2011**, *84*, 094107.
(10) Swamy, V.; Kuznetsov, A.; Dubrovinsky, L. S.; Caruso, R. A.; Shchukin, D. G.; Muddle, B. C. *Phys. Rev. B: Condens. Matter Mater. Phys.* **2005**, *71*, 184302.
(11) Swamy, V.; Dubrovinsky, L. S.; Dubrovinskaia, N. A.; Langenhorst, F.; Simionovici, A. S.; Drakopoulos, M.; Dmitriev, V.; Weber, H.-P. *Solid State Commun.* **2005**, *134*, 541−546.
(12) Hearne, G. R.; Zhao, J.; Dawe, A. M.; Pischedda, V.; Maaza, M.; Nieuwoudt, M. K.; Kibasomba, P.; Nemraoui, O.; Comins, J. D.; Witcomb, M. J. *Phys. Rev. B: Condens. Matter Mater. Phys.* **2004**, *70*, 134102.
(13) Swamy, V.; Dubrovinsky, L. S.; Dubrovinskaia, N. A.; Simionovici, A. S.; Drakopoulos, M.; Dmitriev, V.; Weber, H.-P. *Solid State Commun.* **2003**, *125*, 111−115.
(14) Haines, J.; Léger, J. M. *Phys. B* **1993**, *192*, 233−237.
(15) Sekiya, T.; Ohta, S.; Kamei, S.; Hanakawa, M.; Kurita, S. *J. Phys. Chem. Solids* **2001**, *62*, 717−721.
(16) Arlt, T.; Bermejo, M.; Blanco, M. A.; Gerward, L.; Jiang, J. Z.; Olsen, J. S.; Recio, J. M. *Phys. Rev. B: Condens. Matter Mater. Phys.* **2000**, *61*, 14414−14419.
(17) Zhu, T.; Gao, S.-P. *J. Phys. Chem. C* **2014**, *118*, 11385−11396.
(18) Fu, Z.; Liang, Y.; Wang, S.; Zhong, Z. *Phys. Status Solidi B* **2013**, *250*, 2206−2214.
(19) Dubrovinskaia, N. A.; Dubrovinsky, L. S.; Ahuja, R.; Prokopenko, V. B.; Dmitriev, V.; Weber, H.-P.; Osorio-Guillen, J. M.; Johansson, B. *Phys. Rev. Lett.* **2001**, *87*, 275501.
(20) Muscat, J.; Swamy, V.; Harrison, N. M. *Phys. Rev. B: Condens. Matter Mater. Phys.* **2002**, *65*, 224112.
(21) Pischedda, V.; Hearne, G. R.; Dawe, A. M.; Lowther, J. E. *Phys. Rev. Lett.* **2006**, *96*, 035509.
(22) Swamy, V.; Kuznetsov, A.; Dubrovinsky, L. S.; McMillan, P. F.; Prakapenka, V. B.; Shen, G.; Muddle, B. C. *Phys. Rev. Lett.* **2006**, *96*, 135702.
(23) Wang, Z.; Saxena, S. K. *Solid State Commun.* **2001**, *118*, 75−78.
(24) Wang, Z.; Saxena, S. K.; Pischedda, V.; Liermann, H. P.; Zha, C. S. *J. Phys.: Condens. Matter* **2001**, *13*, 8317−8323.
(25) Yan, X.; Gu, Y.; Zhang, X.; Huang, Y.; Qi, J.; Zhang, Y.; Fujita, T.; Chen, M. *J. Phys. Chem. C* **2009**, *113*, 1164−1167.
(26) Cong, R.; Zhu, H.; Wu, X.; Ma, C.; Yin, G.; Xie, X.; Cui, Q. *J. Phys. Chem. C* **2013**, *117*, 4304−4308.
(27) Yin, G.; Yin, H.; Wang, X.; Sun, M.; Zhong, L.; Cong, R.; Zhu, H.; Gao, W.; Cui, Q. *J. Alloys Compd.* **2014**, *611*, 24−29.
(28) Hu, W.; Liu, Y.; Withers, R. L.; Frankcombe, T. J.; Norén, L.; Snashall, A.; Kitchin, M.; Smith, P.; Gong, B.; Chen, H.; Brink, F.; Schiemer, J.; Wong-Leung, J. *Nat. Mater.* **2013**, *12*, 821−826.
(29) Liu, Y.; Fu, Z.; Sun, Q.; Withers, R. L.; Norén, L.; Zhou, C. C. *N. Patent* 201610288912, May 3, 2016.
(30) Dewaele, A.; Torrent, M.; Loubeyre, P.; Mezouar, M. *Phys. Rev. B: Condens. Matter Mater. Phys.* **2008**, *78*, 104102.
(31) Sun, Q.; Zeng, Y.; Jiang, D. *CrystEngComm* **2012**, *14*, 713−718.
(32) Frank, O.; Zukalova, M.; Laskova, B.; Kürti, J.; Koltai, J.; Kavan, L. *Phys. Chem. Chem. Phys.* **2012**, *14*, 14567−14572.
(33) Ohsaka, T.; Izumi, F.; Fujiki, Y. *J. Raman Spectrosc.* **1978**, *7*, 321−324.
(34) Tian, F.; Zhang, Y.; Zhang, J.; Pan, C. *J. Phys. Chem. C* **2012**, *116*, 7515−7519.
(35) Sahoo, S.; Arora, A. K.; Sridharan, V. *J. Phys. Chem. C* **2009**, *113*, 16927−16933.
(36) Lü, X.; Yang, W.; Quan, Z.; Lin, T.; Bai, L.; Wang, L.; Huang, F.; Zhao, Y. *J. Am. Chem. Soc.* **2014**, *136*, 419−426.
(37) Brown, I. D. *Acta Crystallogr., Sect. B: Struct. Sci.* **1992**, *48*, 553−572.
(38) Brown, I. D. *Acta Crystallogr., Sect. B: Struct. Sci.* **1997**, *53*, 381−393.
(39) For the detailed Bond valence sum calculation, please refer to the below website: http://www.softbv.net/indexconv.html.
(40) Atanacio, A. J.; Bak, T.; Nowotny, J. *ACS Appl. Mater. Interfaces* **2012**, *4*, 6626−6634.
(41) Arbiol, J.; Cerdà, J.; Dezanneau, G.; Cirera, A.; Peiró, F.; Cornet, A.; Morante, J. R. *J. Appl. Phys.* **2002**, *92*, 853−861.
(42) Beck, H. P.; Kaliba, C. *Mater. Res. Bull.* **1991**, *26*, 145−152.
(43) Hanaor, D. A. H.; Sorrell, C. C. *J. Mater. Sci.* **2011**, *46*, 855−874.
(44) Kang, M.-K.; Kim, S. J.; Kim, H. J. *Nanoscale* **2013**, *5*, 3266−3271.

DOI: 10.1021/acs.cgd.7b00055
Cryst. Growth Des. 2017, 17, 2529−2535

Trans-regime Structural Transition of (In^{3+} + Nb^{5+}) Co-doped Anatase TiO_2 Nanocrystals under High Pressure

Qingbo Sun,[†] Larissa Q. Huston,[‡] Terry J. Frankcombe,[§] Jodie E. Bradby,[‡] Teng Lu,[†] Dehong Yu,[∥] Chao Zhou,[⊥] Zhenxiao Fu,[⊥] and Yun Liu[*,†]

[†]Research School of Chemistry, [‡]Research School of Physics and Engineering, the Australian National University, Canberra, Australian Capital Territory, 2601, Australia

[§]School of Physical, Environmental and Mathematical Sciences, University of New South Wales, Canberra, Australian Capital Territory, 2601, Australia

[∥]Australian Nuclear Science and Technology Organisation, Lucas Height, New South Wales, 2234, Australia

[⊥]Fenghua Advanced Technology Holding Co., Ltd., Zhaoqing, Guangdong, 526020, China

SI-1. The doping concentration of In^{3+} and Nb^{5+} ions in co-doped anatase TiO_2 nanocrystals

Table S1, the doping concentration of In^{3+} and Nb^{5+} ions in co-doped anatase TiO_2 nanocrystals.

Measurement methods	In/Ti (at.%)	Nb/Ti (at.%)
XPS	6.49	5.71
EDS of SEM	5.02	4.98
ICP-OES	4.73	4.95

From Table S1, it can be found that the respective doping concentrations of In^{3+} (In/Ti) and Nb^{5+} ions (Nb/Ti) in the co-doped nanocrystals is very close to ~5at.%. It should be pointed out that nanoparticles are directly analyzed by XPS and ICP-OES. The sintered ceramic pellets, which are composed of nanopowders are used for EDS of SEM analysis. These ceramic pellets are prepared by pressing the nanoparticles into pellets and then sintered at 1400 °C for 12 hours. After that, their surface is polished

and coated by carbon. Though XPS, EDS of SEM and ICP-AES are three different analytical techniques, their results are found to be in reasonable consistency with each other.

SI-2. Raman spectrum of (In^{3+}+Nb^{5+}) co-doped baddeleyite-like TiO_2 nanocrystals

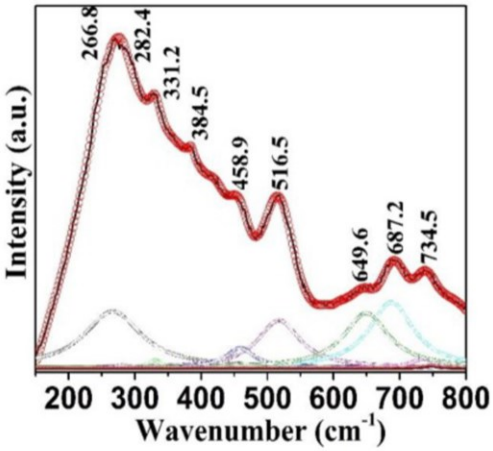

Figure S1. Raman spectrum of (In^{3+}+Nb^{5+}) co-doped anatase TiO_2 nanocrystals pressurized at 47.2 GPa. All of their Raman peaks are consistent to that of a baddeleyite-like TiO_2 structure.

SI-3. Density Functional Theory

DFT calculations were performed using the VASP code.[S1] The projector-augmented wave (PAW) method was used. Atomic pseudopotentials were used to represent the [Ne], [He], [Kr] and [Ar] $4s^2$ $4p^6$ electronic cores of the Ti, O, In and Nb ions, respectively. A plane wave cutoff of 500 eV was used throughout with the PBE+U functional. On-site (+U) corrections were applied in the rotationally-invariant approach of Dudarev, with the *U-J* parameter being 7.4 eV for Ti, In and Nb *d* electrons and 5.4 eV for O *p* electrons. For the In and Nb co-doped crystals, 3×3×1 and 2×2×2 supercells were constructed for the anatase and α-PbO_2-like structures, respectively. In these supercells, four Ti ions were replaced with two In and two Nb ions and an oxygen ion was removed, yielding 5.56% and 6.25% doping for the anatase and α-PbO_2-like structures, respectively. 2×2×2 Γ-centred grids were used for *k*-point sampling for the supercell calculations. All calculations were spin polarised.

A wide range of configurations for the substituted ions were tested. The presence of Ti^{3+} and/or Nb^{4+} ions was analysed by examining the spin density within spheres around each ion. The total energy of the crystal supercells was found to depend strongly on the configuration of the substituted ions. In both the anatase and α-PbO_2-like structures the lowest energies were given by configurations exhibiting the "triangle" motif previously identified in (In+Nb) co-doped rutile TiO_2. This configuration was charaterised by In^{3+} ions in adjacent octagedra, with one of the shared oxygen ions removed for local charge balance. An Nb^{5+} ion would be in a nearby octahedron such that a Ti ion across the oxygen vacancy from the In ions was reduced to Ti^{3+}. Another Nb^{5+}-Ti^{3+} pair would be located within the supercell, with the lowest energies found when this pair was close to the $2In^{3+}$-V_O-Nb^{5+}-Ti^{3+} defect cluster.

The stiffness of the pure and doped crystals was evaluated by first relaxing the ionic positions and lattice vectors of the supercell. The cells were then scaled by ±1% and subjected to relaxation at a constant cell volume. A linear fit to the resulting calculated external pressures yields the bulk modulus. The fitting procedure gives an uncertainty in the calculated values estimated to be ±5 GPa.

In both the co-doped anatase and α-PbO_2-like TiO_2 phases, the most stable configurations of the ions were reminiscent of the $2In^{3+}$-V_O-Ti^{3+} "triangle" motif identified in (In^{3+}+Nb^{5+}) co-doped rutile TiO_2.[14] The DFT calculations predict the bulk moduli of the pure anatase and α-PbO_2-like TiO_2 phases to be 170 and 210 GPa, respectively, in acceptable agreement with the 179 and 258 GPa determined experimentally.[8h] For the most stable configurations of co-doped TiO_2 polymorphs, the calculated bulk moduli were 162 and 193 GPa, respectively, for the co-doped anatase and α-PbO_2-like phases. That is, the DFT calculations predict that the stiffness should *decrease* for the *bulk crystals*, in contradiction to the behavior observed by the Raman spectra of our co-doped TiO_2 *nanocrystals*. It may be because the Raman spectrum is sensitive to the three-dimentional confinement of phonons in finit-sized nanocrystals[8b]. Further consideration in theory is thus required to introduce such a confinement and achieve a theoretical explanation that is not contradictory to the experimental data.

References

[S1] (a) Kresse, G.; Hafner, J. *Phys. Rev. B* 1993, ***47***, 558-561. (b) Kresse, G.; Furthmüller, J. *Phys. Rev. B* 1996, ***54***, 11169-11186.

3.3 Bimetallic ions codoped nanocrystals: doping mechanism, defect formation, and associated structural transition

I wrote the draft of this paper. I synthesized the (In^{3+}+Nb^{5+}) co-doped anatase TiO_2 nanocrystals and designed high pressure reaction experiments. I systematically characterized the samples containing different co-doping levels using XRD, Raman spectroscopy, ICP-OES, HRTEM, SEM/EDS, XPS, HADDF-STEM and others. I also analyzed the related results of DFT calculations performed by Terry J. Frankcombe and conducted high pressure reaction experiments with Larissa Q. Huston. In addition, I also investigated the co-doping mechanisms for difficult-dopant In^{3+} and easy-dopants Nb^{5+} ions.

THE JOURNAL OF PHYSICAL CHEMISTRY Letters

Letter

pubs.acs.org/JPCL

Bimetallic Ions Codoped Nanocrystals: Doping Mechanism, Defect Formation, and Associated Structural Transition

Qingbo Sun,[†] Changlin Zheng,[∥] Larissa Q. Huston,[‡] Terry J. Frankcombe,[*,#] Hua Chen,[§] Chao Zhou,[▽] Zhenxiao Fu,[▽] Ray L. Withers,[†] Lasse Norén,[†] Jodie E. Bradby,[‡] Joanne Etheridge,[∥,⊥] and Yun Liu[*,†]

[†]Research School of Chemistry, [‡]Research School of Physics and Engineering, and [§]Centre for Advanced Microscopy, The Australian National University, Canberra, Australian Capital Territory 2601, Australia

[∥]Monash Centre for Electron Microscopy and [⊥]Department of Materials Science and Engineering, Monash University, Victoria 3800, Australia

[#]School of Physical, Environmental and Mathematical Sciences, University of New South Wales, Australian Capital Territory, Canberra 2601, Australia

[▽]Fenghua Advanced Technology Holding Co., Ltd., Zhaoqing, Guangdong 526020, China

Supporting Information

ABSTRACT: Ionic codoping offers a powerful approach for modifying material properties by extending the selection of potential dopant ions. However, it has been a major challenge to introduce certain ions that have hitherto proved difficult to use as dopants (called "difficult-dopants") into crystal structures at high concentrations, especially through wet chemical synthesis. Furthermore, the lack of a fundamental understanding of how codopants are incorporated into host materials, which types of defect structures they form in the equilibrium state, and what roles they play in material performance, has seriously hindered the rational design and development of promising codoped materials. Here we take In^{3+} (difficult-dopants) and Nb^{5+} (easy-dopants) codoped anatase TiO_2 nanocrystals as an example and investigate the doping mechanism of these two different types of metal ions, the defect formation, and their associated impacts on high-pressure induced structural transition behaviors. It is experimentally demonstrated that the dual mechanisms of nucleation and diffusion doping are responsible for the synergic incorporation of these two dopants and theoretically evidenced that the defect structures created by the introduced In^{3+}, Nb^{5+} codopants, their resultant Ti^{3+}, and oxygen vacancies are locally composed of both defect clusters and equivalent defect pairs. These formed local defect structures then act as nucleation centers of baddeleyite- and α-PbO_2-like metastable polymorphic phases and induce the abnormal trans-regime structural transition of codoped anatase TiO_2 nanocrystals under high pressure. This work thus suggests an effective strategy to design and synthesize codoped nanocrystals with highly concentrated difficult-dopants. It also unveils the significance of local defect structures on material properties.

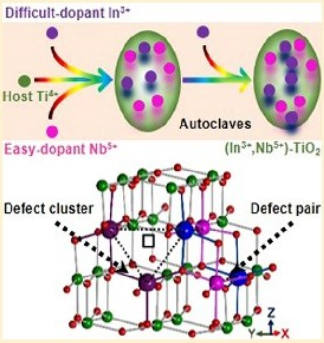

Ionic codoping is a general and effective strategy to significantly improve the macroscopic performances of host materials by tuning their local and average structures. By simultaneously incorporating two or more types of extrinsic ions into the substitutional or interstitial sites of crystal structures, the physicochemical properties of the host materials, such as their dielectric response, optical absorption, or magnetic spin, can be modified significantly. Typical cases can be found in titanium dioxide (TiO_2) due to its multifunctional nature and diverse applications. For instance, our previous work[1] suggested that codoping In^{3+} and Nb^{5+} ions into rutile TiO_2 ceramics enabled the achievement of both colossal permittivity ($>10^5$) and low dielectric loss (<5%) as a consequence of the formation of electron-pinned defect dipoles. Likewise, the simultaneous incorporation of both B^{3+} and N^{3-} ions into anatase TiO_2 microspheres narrowed the host bandgap and thereby enhanced the visible-light photocatalytic activity.[2] Theoretically, Cr and Mn ion codoping was predicted to greatly increase magnetic moments and thus induced abnormal ferromagnetism in paramagnetic TiO_2.[3] In other material systems including graphene, carbon nanotubes, tetrahedrites, and zinc sulfide, the ionic codoping strategy has also been broadly utilized to improve their electrocatalytic, thermoelectric, or fluorescence properties.[4−7]

The ionic codoping strategy also presents many advantages on the resultant chemical compositions of codoped materials. Ions, which on their own might be difficult to introduce into host materials, can be codoped at significantly higher concentrations due to the generation of synergistic effects with another dopant ion. For instance, <1 at% In^{3+} ions can be

Received: June 2, 2017
Accepted: June 29, 2017
Published: June 29, 2017

DOI: 10.1021/acs.jpclett.7b01384
J. Phys. Chem. Lett. 2017, 8, 3249−3255

dissolved into TiO_2 without phase segregation,[8] whereas the dissolution limit can approach ~5 at% if codoped with Nb^{5+} ions.[1] Under some scenarios, unwanted species such as oxygen vacancies in the case of N^{3-} single-doped TiO_2[9] or Ti^{3+} ions in the case of Nb^{5+} monodoped TiO_2,[10] which lead to a deterioration of photocatalytic properties by forming "trapping or recombination centers" of photogenerated electron−hole pairs, can also be efficiently avoided if another appropriate ion is introduced to couple with each other as well as to balance the overall charge of the whole codoped system (e.g., Nb^{5+}−N^{3-} codoping).[11]

From a structural perspective, ionic codoping also changes the local structures of the host materials. The selected codoped ions can exist as isolated point defects, bind together to form defect pairs, or form larger local defect clusters[1,5,12−14] depending upon the chemical compositions or synthesis route. We previously pointed out that codoping "too big" trivalent In^{3+} ions with Nb^{5+} ions was favorable to generate triangular- and diamond-shaped defect clusters in rutile TiO_2,[1] while codoping smaller Al^{3+} ions with Nb^{5+} ions locally produced an intergrown, intermediate, and metal-ion-rich structure.[15] In (B, N) codoped carbon nanotubes,[5] the B^{3+} and N^{3-} ions could either exist as isolated point defects or chemically bind together depending on their synthesis conditions. The resultant electrocatalytic properties of prepared (B, N) codoped carbon nanotubes, however, could only be enhanced by the former.

Although ionic codoping has been successfully used to tune the physicochemical properties of a wide range of host materials by slightly modifying the chemical composition or locally creating different defect states, their reliable wet chemical synthesis remains complicated and rather difficult to control. This is especially the case when the ions that are difficult to dope with (called "difficult-dopants") are involved because (1) the solubility of the initial reactants should be considered to guarantee enough ions to homogeneously distribute in the reaction solvent, (2) the precipitation of codopant ions should be coordinated to inhibit the generation of possible impurities during the reaction process, and (3) the ligands of the metal ions should be modified to achieve the expected doping concentrations in the resultant products. Furthermore, fundamental concerns regarding the synthesis and the resultant codoped materials themselves still remain unclear; for example, how codopants are introduced into the crystal structures of host materials during the chemical reaction process (i.e., doping mechanism), whether the same types of codopants create the same defect states in different polymorph of the same material (i.e., defect formation), and what roles these introduced local defect structures play on the macroscopic properties of the codoped host materials. Studies on the doping mechanism, the defect formation, and their associated impacts are rather important to both design and synthesize novel types of codoped materials as well as further understand the intrinsic structure−performance relationship.

We herein combine the easy- and difficult-dopant ions together in an attempt to effectively increase the doping levels of the latter. In^{3+} and Nb^{5+} codoped anatase nanocrystals are then synthesized to further demonstrate the effectiveness of the designed codoping strategies. The potential doping mechanisms of the two different types of metal ions (the In^{3+} difficult-dopant ions and the Nb^{5+} easy-dopant ions) are investigated under solvothermal reaction conditions. Through density functional theory (DFT) calculations, we present the local defect structures generated by the In^{3+}, Nb^{5+} codopants, the resultant Ti^{3+} ions, and oxygen vacancies. Furthermore, the influence of these intentionally introduced local defect structures on high-pressure reaction behaviors of synthesized codoped nanocrystals are analyzed.

In^{3+} and Nb^{5+} codoped anatase nanocrystals with a chemical formula of $(Ti^{4+}_{1-x-y-z}Ti^{3+}_{x}In^{3+}_{y}Nb^{5+}_{z})(O^{2-}_{2-(x+y+z)/2}\square_{y/2})$ are synthesized by a solvothermal method ($\square$ here represents oxygen vacancies and also labeled as $V_O^{\bullet\bullet}$). The x, y, and z values in the above chemical formula are experimentally determined to range from 0 up to 0.046 and are controlled by adjusting the concentrations of niobium pentachloride and indium acetate in ethanol solvent while fixing the added volume of titanium chloride. Detailed descriptions about the synthesis and characterization of these nanocrystals are given in the Supporting Information (SI-1 and SI-2). In^{3+} and Nb^{5+} ions are chosen as appropriate codopant ions because they enable charge compensating as well as produce a significant local structural change due to the bigger ionic radii of both codopants (94 pm for In^{3+} and 78 pm for Nb^{5+}) as compared with that of Ti^{4+} (74.5 pm). Such local structural variation induced the formation of defect clusters in the case of the analogous (In^{3+}+Nb^{5+}) codoped rutile TiO_2 ceramics[1] to "pin" electrons and thus resulted in an excellent dielectric performance.

In the current anatase case, the ionic radii of the In^{3+} ions are again significantly too large. The calculated apparent valence (AV) or bond valence sum (BVS) of an In^{3+} ion in anatase TiO_2 is 5.33 valence units (v.u.) instead of the ideal 3.00 v.u. estimated using the softBV program (SI-3, Supporting Information),[16−18] that is, ~78% overbonded! Without the removal of at least one of the surrounding oxygen ions and the addition of a further neighboring In^{3+} ion for charge balance, it is rather difficult to introduce In^{3+} ions into TiO_2 to achieve high doping levels by normal wet chemical reaction routes such as sol−gel or coprecipitation. A solvothermal method is thus attempted to combine the higher spontaneous pressure of ethanol with the comparatively higher heating temperature of sealed autoclaves. In contrast with the difficulty in In^{3+} doping, the ionic radii of Nb^{5+} ions are almost similar to that of Ti^{4+} with an AV of 5.37 v.u., only slightly overbonded by ~7.4% (SI-3, Supporting Information). The chemical doping of Nb^{5+} ions into anatase TiO_2 is thus relatively easy and can reach up to a concentration of ~14 at%[19] or more (called "easy-dopants"). Note, however, that charge balance associated with single doping of Nb^{5+} ions can only be achieved through generating an equal concentration of reduced Ti^{3+} ions.

Experimentally, we find that nearly all of the Nb^{5+} ions in the initial reaction solution can be doped into anatase TiO_2 nanocrystals (Figure 1a). Their doping concentrations are thus easily controlled through just tuning the added weight of starting materials like niobium pentachloride. By contrast, only a small proportion of In^{3+} ions in the reaction solution can be finally incorporated into TiO_2 to achieve a closely equivalent doping level as that of the Nb^{5+} ions (Figure 1b). For example, if ~5.0 at% In^{3+} ions (compared with total titanium ions, i.e., $y \approx 0.046$ in the above chemical formula) are designed in codoped TiO_2 nanocrystals, their actual concentration in the initial reaction solution should be up to ~90 at%. Most of the In^{3+} ions are left in the reaction solution and should be further separated from the synthesized nanoparticles through post-treatment process for reuse.

DOI: 10.1021/acs.jpclett.7b01384
J. Phys. Chem. Lett. 2017, 8, 3249−3255

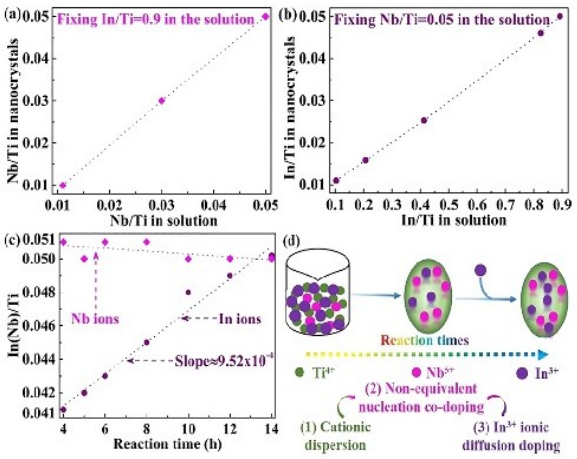

Figure 1. Ratio of Nb/Ti (a) and In/Ti (b) in the initial reaction solution (x axis) and in the resultant codoped anatase TiO_2 nanocrystals (y axis). These data points were collected at the reaction time of 14 h. It is found that almost all of the Nb ions but only a small proportion of the In ions in the reaction solution can be finally codoped into TiO_2. (c) Ratio of Nb/Ti and In/Ti at different reaction times, suggesting that dual mechanisms of nucleation and diffusion doping are responsible for the incorporation of the In^{3+} ions, while nucleation-only doping is observed for that of the Nb^{5+} ions. (d) Schematic illustrating the different doping mechanisms for the In^{3+} and Nb^{5+} codopants. Three critical steps should be involved during the synthesis: (1) cationic homogeneous distribution in the solution, (2) nonequivalent nucleation codoping of Nb^{5+} and In^{3+} ions, and (3) the further diffusion doping of the In^{3+} ions to achieve the equal doping concentrations as that of the Nb^{5+} ions.

In addition, we further found that the doping level of Nb^{5+} ions in the codoped TiO_2 nanocrystals remained virtually unchanged for reaction times between 4 and 14 h, while that of the In^{3+} ions increases almost linearly over the same reaction period (Figure 1c). For reaction times shorter than 4 h, it is difficult to collect any nanoparticles from the viscous and transparent reaction solution. In such short reaction times, nanoparticles perhaps are not formed or their particle size is too small to be separated for collection. After 14 h, the ratio of In/Ti and Nb/Ti in the nanocrystals does not obviously change. Clearly, the incorporation of Nb^{5+} ions is related to a typical nucleation doping. Although the major proportion of the doped In^{3+} ions (~4.1 at%, compared with total titanium ions) is also introduced together with Nb^{5+} ions through nucleation doping, the remaining proportion of them (~0.9 at%) is actually incorporated into TiO_2 through diffusion doping with a diffusion rate of $\sim 9.52 \times 10^{-4}$ molar per hour. Dual mechanisms (nucleation and diffusion doping) are thus proposed for the introduction of the In^{3+} ions, and nucleation-only doping is suggested for that of the Nb^{5+} ions. This understanding of doping mechanisms is critical for the controllable synthesis of other metal-ion-codoped nanomaterials and the desirable design of material properties.[20−22]

A schematic, which visually illustrates the two mechanisms of introducing In^{3+} and Nb^{5+} ions into TiO_2 nanocrystals, is shown in Figure 1d. Three critical steps are involved during synthesis, that is, (1) homogeneous distribution of all cations (Ti^{4+}, Nb^{5+}, and In^{3+}) in the ethanol solvent to form one transparent solution, (2) the nonequivalent nucleation codoping of almost all of the Nb^{5+} ions but only a proportion of the In^{3+} ions, which results in the lower doping concentrations of the In^{3+} ions relative to that of the Nb^{5+} ions, and (3) the diffusion doping of an additional proportion of In^{3+} ions to achieve equivalent doping levels of the In^{3+} and Nb^{5+} ions. It seems that the easy Nb^{5+} dopant ions create a synergistic environment for accommodating the more difficult In^{3+} dopant ions. The coupling of these two different types of doped ions is thus demonstrated to be an efficient method to significantly increase the doping concentration of difficult-dopants.

The synthesized (In^{3+}+Nb^{5+}) codoped TiO_2 nanocrystals were then investigated by X-ray powder diffraction (XRD). All diffraction peaks could be assigned to an average tetragonal anatase-type phase with space-group symmetry $I4_1/amd$ (SI-4, Supporting Information). This phase analysis was carefully done to be sure that all other analyses were conducted on the single-phase sample. The chemical compositions of the optimized, codoped anatase nanocrystals were then carefully analyzed via energy-dispersive X-ray spectroscopy (EDS) in a scanning electron microscope (SEM) and an inductively coupled plasma optical emission spectrometer (ICP-OES). The atomic ratio of indium to niobium is found to be about 1:1, and their respective doping concentrations nearly approach 0, 1.0, 3.0, and 4.6 at%, that is, $y \approx z \approx 0$, 0.010, 0.030, and 0.046 (SI-5, Supporting Information). With the gradual increase in the y and z values, there is a gradual shift of the (101) XRD peak, a linear expansion of the lattice parameters (***a***, ***b***, and ***c***) and of the unit-cell volume (***V***, SI-4, Supporting Information) due to the partial substitution of the smaller Ti^{4+} ions with the bigger In^{3+} and Nb^{5+} ions. These XRD results and the various microscopic characterization (to be discussed below) suggest the effective codoping of In^{3+} and Nb^{5+} ions into anatase TiO_2 nanoparticles. This is also confirmed by Raman spectra, which exhibit similar Raman peaks to the undoped anatase TiO_2 nanoparticles (SI-6, Supporting Information).[23] Furthermore, we do not detect any other Raman signals or additional XRD peaks even in the samples with $y \approx z \approx 0.046$ (i.e., a total doping concentration of ~9.2 at%) and thus believe that these (In^{3+}+Nb^{5+})-codoped TiO_2 nanocrystals represent a single-phase solid solution.

The chemical valence states of the cations in the codoped nanocrystals with $y \approx z \approx 0.046$ were subsequently analyzed by X-ray photoelectron spectroscopy (XPS, Figure 2a−c). As seen, the indium and niobium ions have the chemical valence of +3 and +5, respectively; that is, their chemical valences are the same as those of their starting materials. For the titanium ions, the XPS data show two separate peaks with individual binding energies of ~459.3 and 457.6 eV. These two XPS peaks correspond to Ti^{4+} and Ti^{3+}, respectively. The generation of Ti^{3+} ions can be ascribed to the reduction of a proportion of the Ti^{4+} ions induced by the Nb^{5+} ions. Their concentration is calculated to be ~3.5 at% by fitting to the XPS data (Figure 2c). The slight difference between the doping level of Ti^{3+} (3.5 at%) and that of the Nb^{5+} ions (4.6 at%) is attributed to the oxidization of partial surficial Ti^{3+} ions due to the high surface energy and high reaction activity of the nanoparticles. The presence of Ti^{3+} ions is also confirmed by the electron paramagnetic resonance (EPR) spectrum (Figure 2d). Two EPR signals at $g_1 = 1.97$ and $g_2 = 1.94$ should come from the paramagnetic resonances of Ti^{3+} with $3d^1$ electrons trapped on the lattices.[24] There is no Nb^{4+} observed in both XPS and EPR characterization. The prepared (In^{3+}+Nb^{5+}) codoped TiO_2 nanocrystals thus contain not only In^{3+} and Nb^{5+} codopants but also include induced Ti^{3+} ions and oxygen vacancies (to

DOI: 10.1021/acs.jpclett.7b01384
J. Phys. Chem. Lett. 2017, 8, 3249−3255

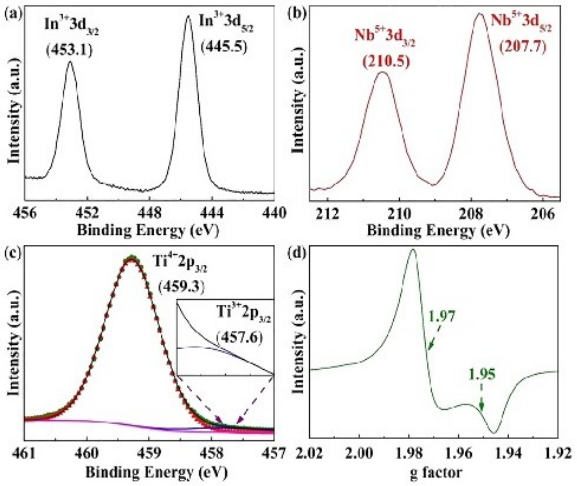

Figure 2. XPS (a–c) and room temperature EPR (d) spectra of the synthesized $(Ti^{4+}_{0.862}Ti^{3+}_{0.046}In^{3+}_{0.046}Nb^{5+}_{0.046})(O^{2-}_{1.977}\square_{0.023})$ anatase nanocrystals with $x \approx y \approx z \approx 0.046$, determining the chemical valence states of indium (+3) and niobium (+5) codopants as well as the titanium (+4 and +3).

balance the charge of the overall codoped TiO_2 material). The In^{3+}, Nb^{5+}, Ti^{3+}, and oxygen vacancies are labeled In'_{Ti}, $Nb^{\bullet}_{Ti}$, Ti'_{Ti}, and $V^{\bullet\bullet}_{O}$ using Kröger–Vink notation, respectively.

To further investigate In^{3+} and Nb^{5+} codoped anatase TiO_2 nanocrystals, aberration-corrected HAADF-STEM (high-angle annular dark-field scanning transmission electron microscopy) images of the synthesized $(Ti^{4+}_{0.862}Ti^{3+}_{0.046}In^{3+}_{0.046}Nb^{5+}_{0.046})(O^{2-}_{1.977}\square_{0.023})$ nanocrystals (i.e., $x \approx y \approx z \approx 0.046$) were taken (Figure 3). It is observed that

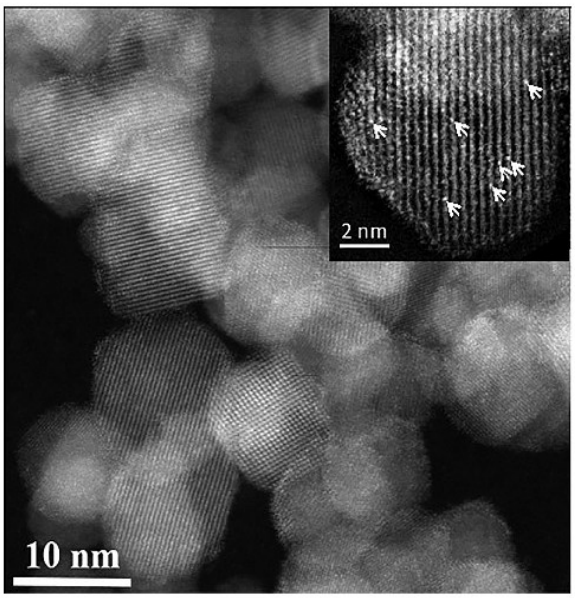

Figure 3. Typical aberration-corrected HAADF-STEM image of the synthesized anatase $(Ti^{4+}_{0.862}Ti^{3+}_{0.046}In^{3+}_{0.046}Nb^{5+}_{0.046})(O^{2-}_{1.977}\square_{0.023})$ nanocrystals with $x \approx y \approx z \approx 0.046$. The arrowed brighter dots in the inset show the presence of atomic columns with a greater density of heavier atoms (indium and/or niobium), indicating that the In^{3+} and Nb^{5+} ions are indeed codoped into TiO_2 host materials.

most of the nanocrystals have quasi-spherical shapes (in projection) with small average particle diameters of <10 nm. In atomic-resolution HAADF-STEM mode, an atomic column containing any indium (atomic number, $Z = 49$) or niobium atoms ($Z = 41$) substituting for the lighter Ti atoms ($Z = 22$) should lead to a noticeable local increase in the corresponding image intensity relative to a pure, unsubstituted Ti column (of the same thickness). The inset in Figure 3 shows a HAADF-STEM image of a nanoparticle exhibiting (011) lattice fringes (running vertically). The alternating bright and dark stripes correspond to double rows of metal ions (separated in the horizontal direction by 0.88 Å and clearly unresolved) and the complete absence of metal ions, respectively. Note that the arrowed bright dots in the inset always fall within the bright metal ion striped regions, suggesting that they represent local atomic columns with an increased density of substituted In and Nb atoms. Indeed, they may well represent individual In or Nb atoms. This directly demonstrates that In^{3+} and Nb^{5+} ions are indeed codoped into the crystal structures of anatase nanocrystals. In addition, the results of element mapping also indicate that In^{3+} and Nb^{5+} ions are really codoped into anatase TiO_2 nanocrystals and homogeneously distributed (SI-7, Supporting Information).

It also appears that most of the quasi-spherical nanocrystals achieved at the higher doping levels gradually evolve to nanocubes or nanocuboids with a decrease in the codopant concentration (SI-7, Supporting Information), consistent with results reported for Nb-monodoped TiO_2[19] and Mg-monodoped ZnO[25] nanoparticles and can be attributed to their changed average crystal structure after codoping (SI-4, Supporting Information). Additionally, the change of codoping concentration slightly modified the average particle size, and higher doping levels lead to smaller particle diameters, but they all remain <10 nm in terms of both the size calculated by the Scherrer equation[26,27] and that estimated via low-magnification TEM lattice imaging (SI-8, Supporting Information). These small nanoparticles potentially provide many practical applications, for example, to prepare thin films by directly depositing them onto substrates, to use as building blocks in constructing functional nanodevices, or to lower the sintering temperatures of related ceramics as raw materials/additives.

To gain further insight into possible local defect clusters created by the codoping of In^{3+} and Nb^{5+} ions, DFT calculations were carried out on our synthesized anatase compounds with the chemical formula of $(Ti^{4+}_{0.862}Ti^{3+}_{0.046}In^{3+}_{0.046}Nb^{5+}_{0.046})(O^{2-}_{1.977}\square_{0.023})$. The calculations were performed using the VASP code[28−31] and a $3 \times 3 \times 1$ supercell of the anatase TiO_2 structure. Four Ti^{4+} ions were substituted by two In^{3+} and two Nb^{5+} ions in various configurations. This yielded a respective doping level of 5.56 at%, which is very close to the experimental value (4.6 at% In^{3+} + 4.6 at% Nb^{5+}) of this work. More details of the calculation setup are given in SI-9 (Supporting Information).

The total energy of the codoped compounds is found to depend strongly on the configuration of the substituted ions. The lowest energy defect structure is provided by the configuration shown in Figure 4. The $2In'_{Ti} + V^{\bullet\bullet}_{O} + Ti'_{Ti}$ "triangle" motif, which was previously identified in the (In^{3+}+Nb^{5+}) codoped rutile TiO_2,[1] was also observed here. This configuration was characterized by In^{3+} ions located in adjacent octahedra, with one of the shared oxygen ions removed for local charge balance considerations. A Nb^{5+} ion would be in a nearby octahedron such that a Ti ion across the

DOI: 10.1021/acs.jpclett.7b01384
J. Phys. Chem. Lett. 2017, 8, 3249−3255

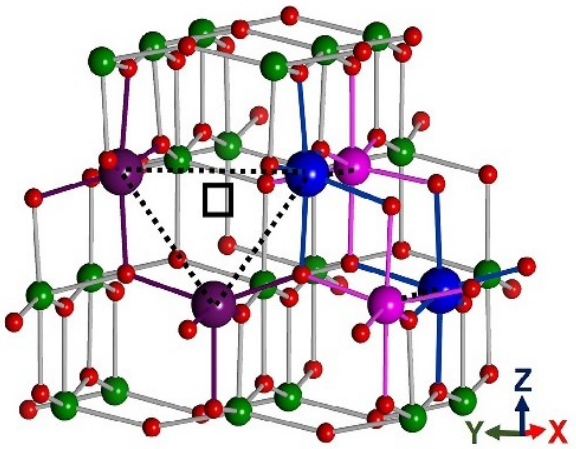

Figure 4. Motif of the lowest energy defect structures. Balls representing ions are colored according to In^{3+}: purple, Nb^{5+}; pink, Ti^{3+}; blue, Ti^{4+}; green, O^{2-}; red. Dashed lines indicate the $2In'_{Ti} + V_O^{\bullet\bullet} + Ti'_{Ti} + Nb^{\bullet}_{Ti}$ defect clusters and adjacent $Ti'_{Ti} + Nb^{\bullet}_{Ti}$ defect pairs.

oxygen vacancy from the indium ions was reduced to Ti^{3+}. In the low-energy configurations, one Nb^{5+} ion is connected to the triangular-shaped defect cluster to form a more complicated $2In'_{Ti} + V_O^{\bullet\bullet} + Ti'_{Ti} + Nb^{\bullet}_{Ti}$ defect complex. The other Nb^{5+} ion links with the second Ti^{3+} ion to form a $Ti'_{Ti} + Nb^{\bullet}_{Ti}$ defect pair. This defect pair would be located nearby within the supercell, with the lowest energies found when it was adjacent to the $2In'_{Ti} + V_O^{\bullet\bullet} + Ti'_{Ti} + Nb^{\bullet}_{Ti}$ defect clusters. Although these defect models also contain triangle-shaped defect complexes and are thus similar to that of (In^{3+}+Nb^{5+}) codoped rutile TiO_2,[1] they also exhibit their own special features with (1) the newly introduced $Ti'_{Ti} + Nb^{\bullet}_{Ti}$ defect pairs, which may be nearby but not adjacent to the triangular In-containing defect clusters, and (2) the triangle-shaped defect complexes is modified by one Nb^{5+} ion to form a more complicated $2In'_{Ti} + V_O^{\bullet\bullet} + Ti'_{Ti} + Nb^{\bullet}_{Ti}$ defect cluster. Two polymorphs of a single material can thus locally produce different defect models though the selected codopants are the same.

Figure 5 presents the high-pressure reaction behavior of these defect-cluster and defect-pair modified nanocrystals with $x \approx y \approx z \approx 0.010$. In situ Raman signals were collected under compression and decompression conditions. Detailed experimental processes are described in SI-10 (Supporting Information). A gradual phase transition from anatase to a baddeleyite-like structure can be observed under compression (Figure 5a). Subsequently, the newly formed baddeleyite-like structure transforms to an α-PbO_2-like phase under decompression (Figure 5b). During the entire compression and decompression cycle, the codoped anatase nanocrystals undergo an anatase → baddeleyite-like phase (~20.2 GPa, compression) → α-PbO_2-like structure (~33.0 GPa, decompression) phase-transition sequence. This structural transition sequence is inconsistent with the pressure-induced amorphization of undoped anatase TiO_2 nanocrystals having a similar crystal size[32−35] but is closely analogous to the phase-transition behavior of those pure TiO_2 nanocrystals with a larger particle size of 11 to 40 nm.[36−38] The anatase $(Ti^{4+}_{1-x-y-z}Ti^{3+}_{x}In^{3+}_{y}Nb^{5+}_{z})(O^{2-}_{2-(x+y+z)/2}\square_{y/2})$ nanocrystals thus possess an abnormal trans-regime structural transition behavior under high pressure. This abnormal phase evolution should be related to the intentionally introduced $2In'_{Ti} + V_O^{\bullet\bullet} + Ti'_{Ti} + Nb^{\bullet}_{Ti}$ defect clusters or $Ti'_{Ti} + Nb^{\bullet}_{Ti}$ defect pairs because they can act as nucleation centers of baddeleyite- or α-PbO_2-like metastable polymorphic phases and thus induce the crystallization of new crystal structures.

In conclusion, highly concentrated In^{3+} difficult-dopants are successfully introduced into TiO_2 crystal structures through the synergistic effects of the Nb^{5+} easy-dopants. It is found that the dual mechanisms of nucleation and diffusion doping are responsible for the incorporation of the difficult-dopant In^{3+} ions while nucleation-only doping is observed for that of the easy-dopant Nb^{5+} ions. The local defect structures generated by codoped In^{3+}, Nb^{5+} ions, their resultant Ti^{3+}, and oxygen vacancies are composed of both $2In'_{Ti} + V_O^{\bullet\bullet} + Ti'_{Ti} + Nb^{\bullet}_{Ti}$ defect clusters and equivalent $Ti'_{Ti} + Nb^{\bullet}_{Ti}$ defect pairs. These intentionally introduced defects would act as nucleation centers of baddeleyite- and α-PbO_2-like metastable polymorphic phases and thereby induce an abnormal trans-regime structural transition of codoped anatase TiO_2 nanocrystals under high

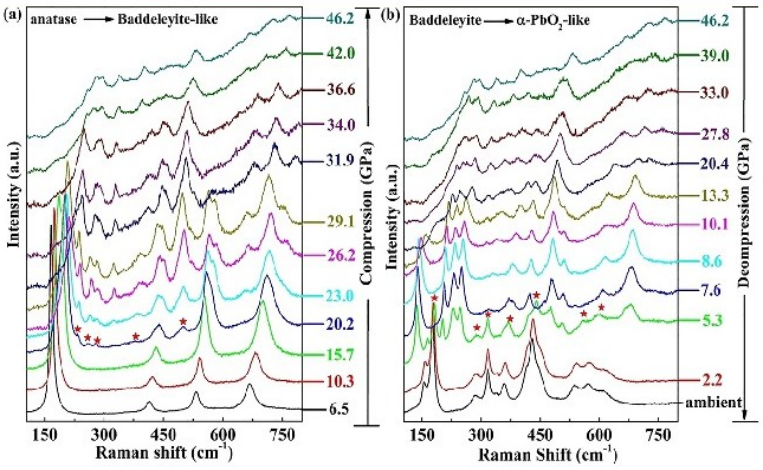

Figure 5. In situ Raman spectra of anatase $(Ti^{4+}_{0.970}Ti^{3+}_{0.010}In^{3+}_{0.010}Nb^{5+}_{0.010})(O^{2-}_{1.995}\square_{0.005})$ nanocrystals ($x \approx y \approx z \approx 0.010$) collected under compression (a) and decompression (b) conditions. Their crystallographic evolution follows the sequence of anatase → baddeleyite-like phase (compression) → α-PbO_2-like structure (decompression).

DOI: 10.1021/acs.jpclett.7b01384
J. Phys. Chem. Lett. 2017, 8, 3249−3255

pressure. We believe that this work provides new insight into the design and synthesis of other novel codoped materials with high concentrations of difficult-dopant ions, opens a new avenue to develop new codoping systems for developing new functional materials, and significantly advances local defect structures in solids.

■ ASSOCIATED CONTENT

Supporting Information

The Supporting Information is available free of charge on the ACS Publications website at DOI: 10.1021/acs.jpclett.7b01384.

Synthesis and characterization of anatase $(Ti^{4+}_{1-x-y-z}Ti^{3+}_{x}In^{3+}_{y}Nb^{5+}_{z})(O^{2-}_{2-(x+y+z)/2}\square_{y/2})$ nanocrystals, the analysis of their chemical compositions, average particle size. and other related properties. (PDF)

■ AUTHOR INFORMATION

Corresponding Authors

*Y.L.: E-mail: yun.liu@anu.edu.au.

*T.J.F.: E-mail: t.frankcombe@adfa.edu.au.

ORCID

Qingbo Sun: 0000-0003-3546-0018

Terry J. Frankcombe: 0000-0001-9791-5394

Yun Liu: 0000-0002-5404-3909

Author Contributions

Q.S., R.L.W., Y.L., and T.J.F. make the main contribution to the preparation of this manuscript. Y.L. initiated this research, planned, and coordinated all experimental and theoretical work. T.J.F. did the theoretical work collaborated with Y.L. Q.S. designed the approach for the fabrication of the samples with different compositions and synthetic conditions. Q.S., H.C., L.N., and R.L.W. conducted HRTEM, SEM/EDS, and XPS analysis. C. Z. and J. E. conducted the measurement of high-angle annular dark-field scanning transmission electron microscopy. Q.S. and L.Q.H. performed the high-pressure reaction experiments under the supervision of J.E.B. All authors were involved in the data analysis and discussion as well as the manuscript preparation.

Notes

The authors declare no competing financial interest.

■ ACKNOWLEDGMENTS

Q.S., Y.L., and T.J.F. acknowledge the support of the Australian Research Council (ARC) in the form of Discovery Projects. Y.L., T.J.F., and J.E.B. also appreciate the support from the ARC Future Fellowships program. We acknowledge the facilities and the scientific and technical assistance of the Australian microscopy and microanalysis research facility (AMMRF) at the Centre of advanced Microscopy, the Australian National University. We also appreciate Jie Gao (Shanghai Institute of Ceramics) for her assistance in ICP-OES analysis and Bill Gong (University of New South Wales) for his help in XPS characterization. The FEI Titan3 80-300 S/TEM instrument at the Monash Centre for Electron Microscopy was funded by ARC Grant LE0454166.

■ REFERENCES

(1) Hu, W.; Liu, Y.; Withers, R. L.; Frankcombe, T. J.; Norén, L.; Snashall, A.; Kitchin, M.; Smith, P.; Gong, B.; Chen, H.; et al. Electron-pinned defect-dipoles for high-performance colossal permittivity materials. *Nat. Mater.* **2013**, *12*, 821−826.

(2) Liu, G.; Yin, L.-C.; Wang, J.; Niu, P.; Zhen, C.; Xie, Y.; Cheng, H.-M. A red anatase TiO_2 photocatalyst for solar energy conversion. *Energy Environ. Sci.* **2012**, *5*, 9603−9610.

(3) Zarhri, Z.; Benyoussef, A.; El Kenz, A. E. Theoretical study of TiO_2 doped with single and double impurities. *J. Supercond. Novel Magn.* **2014**, *27*, 1323−1328.

(4) Ito, Y.; Cong, W.; Fujita, T.; Tang, Z.; Chen, M. High catalytic activity of nitrogen and sulfur co-doped nanoporous graphene in the hydrogen evolution reaction. *Angew. Chem., Int. Ed.* **2015**, *54*, 2131−2136.

(5) Zhao, Y.; Yang, L.; Chen, S.; Wang, X.; Ma, Y.; Wu, Q.; Jiang, Y.; Qian, W.; Hu, Z. Can boron and nitrogen co-doping improve oxygen reduction reaction activity of carbon nanotubes? *J. Am. Chem. Soc.* **2013**, *135*, 1201−1204.

(6) Wu, P.; Yan, X.-P. Doped quantum dots for chemo/biosensing and bioimaging. *Chem. Soc. Rev.* **2013**, *42*, 5489−5521.

(7) Lu, X.; Morelli, D. T.; Xia, Y.; Ozolins, V. Increasing the thermoelectric figure of merit of tetrahedrites by co-doping with nickel and zinc. *Chem. Mater.* **2015**, *27*, 408−413.

(8) Atanacio, A. J.; Bak, T.; Nowotny, J. Effect of indium segregation on the surface versus bulk chemistry for indium-doped TiO_2. *ACS Appl. Mater. Interfaces* **2012**, *4*, 6626−6634.

(9) Rumaiz, A. K.; Woicik, J. C.; Cockayne, E.; Lin, H. Y.; Jaffari, G. H.; Shah, S. I. Oxygen vacancies in N doped anatase TiO_2: experiment and first-principles calculations. *Appl. Phys. Lett.* **2009**, *95*, 262111.

(10) Kong, L.; Wang, C.; Zheng, H.; Zhang, X.; Liu, Y. Defect-induced yellow color in Nb-doped TiO_2 and its impact on visible-light photocatalysis. *J. Phys. Chem. C* **2015**, *119*, 16623−16632.

(11) Sun, Q.; Cortie, D.; Zhang, S.; Frankcombe, T. J.; She, G.; Gao, J.; Sheppard, L. R.; Hu, W.; Chen, H.; Zhuo, S.; et al. The formation of defect-pairs for highly efficient visible-light catalysts. *Adv. Mater.* **2017**, *29*, 1605123.

(12) Gai, Y.; Li, J.; Li, S.-S.; Xia, J.-B.; Wei, S.-H. Design of narrow-gap TiO_2: a passivated codoping approach for enhanced photoelectrochemical activity. *Phys. Rev. Lett.* **2009**, *102*, 036402.

(13) Breault, T. M.; Bartlett, B. M. Composition dependence of TiO_2:$(Nb,N)_{-x}$ compounds on the rate of photocatalytic methylene blue dye degradation. *J. Phys. Chem. C* **2013**, *117*, 8611−8618.

(14) Dong, W.; Hu, W.; Berlie, A.; Lau, K.; Chen, H.; Withers, R. L.; Liu, Y. Colossal dielectric behavior of Ga+Nb co-doped rutile TiO_2. *ACS Appl. Mater. Interfaces* **2015**, *7*, 25321−25325.

(15) Hu, W.; Lau, K.; Liu, Y.; Withers, R. L.; Chen, H.; Fu, L.; Gong, B.; Hutchison, W. Colossal dielectric permittivity in (Nb+Al) codoped rutile TiO_2 ceramics: compositional gradient and local structure. *Chem. Mater.* **2015**, *27*, 4934−4942.

(16) Brown, I. D. Chemical and steric constraints in inorganic solids. *Acta Crystallogr., Sect. B: Struct. Sci.* **1992**, *48*, 553−572.

(17) Brown, I. D. Influence of chemical and spatial constraints on the structures of inorganic compounds. *Acta Crystallogr., Sect. B: Struct. Sci.* **1997**, *53*, 381−393.

(18) For the detailed Bond Valence Sum calculation, please see http://www.softbv.net/indexconv.html.

(19) De Trizio, L.; Buonsanti, R.; Schimpf, A. M.; Llordes, A.; Gamelin, D. R.; Simonutti, R.; Milliron, D. J. Nb-doped colloidal TiO_2 nanocrystals with tunable infrared absorption. *Chem. Mater.* **2013**, *25*, 3383−3390.

(20) Norris, D. J.; Efros, A. L.; Erwin, S. C. Doped nanocrystals. *Science* **2008**, *319*, 1776−1779.

(21) Buonsanti, R.; Milliron, D. J. Chemistry of doped colloidal nanocrystals. *Chem. Mater.* **2013**, *25*, 1305−1317.

(22) Vlaskin, V. A.; Barrows, C. J.; Erickson, C. S.; Gamelin, D. R. Nanocrystal diffusion doping. *J. Am. Chem. Soc.* **2013**, *135*, 14380−14389.

(23) Naldoni, A.; Allieta, M.; Santangelo, S.; Marelli, M.; Fabbri, F.; Cappelli, S.; Bianchi, C. L.; Psaro, R.; Dal Santo, V. D. Effect of nature and location of defects on bandgap narrowing in black TiO_2 nanoparticles. *J. Am. Chem. Soc.* **2012**, *134*, 7600−7603.

(24) Khomenko, V. M.; Langer, K.; Rager, H.; Fett, A. Electronic absorption by Ti^{3+} ions and electron delocalization in synthetic blue rutile. *Phys. Chem. Miner.* **1998**, *25*, 338−346.
(25) Yang, Y.; Jin, Y.; He, H.; Wang, Q.; Tu, Y.; Lu, H.; Ye, Z. Dopant-induced shape evolution of colloidal nanocrystals: the case of zinc oxide. *J. Am. Chem. Soc.* **2010**, *132*, 13381−13394.
(26) Folli, A.; Pochard, I.; Nonat, A.; Jakobsen, U. H.; Shepherd, A. M.; Macphee, D. E. Engineering photocatalytic cements: understanding TiO_2 surface chemistry to control and modulate photocatalytic performances. *J. Am. Ceram. Soc.* **2010**, *93*, 3360−3369.
(27) Sun, Q.; Zeng, Y.-P.; Jiang, D. High magnetic field inducing magnetic transitions of Fe^{3+} and Ni^{2+} doped In_2O_3 nanocubes. *Solid State Commun.* **2011**, *151*, 1220−1205.
(28) Kresse, G.; Hafner, J. Ab initio molecular dynamics for liquid metals. *Phys. Rev. B: Condens. Matter Mater. Phys.* **1993**, *47*, 558.
(29) Kresse, G.; Furthmüller, J. Efficient iterative schemes for ab initio total-energy calculations using a plane-wave basis set. *Phys. Rev. B: Condens. Matter Mater. Phys.* **1996**, *54*, 11169−11184.
(30) Hacene, M.; Anciaux-Sedrakian, A.; Rozanska, X.; Klahr, D.; Guignon, T.; Fleurat-Lessard, P. Accelerating VASP electronic structure calculations using graphic processing units. *J. Comput. Chem.* **2012**, *33*, 2581−2589.
(31) Hutchinson, M.; Widom, M. VASP on a GPU: application to exact-exchange calculations of the stability of elemental boron. *Comput. Phys. Commun.* **2012**, *183*, 1422−1426.
(32) Wang, Z.; Saxena, S. K. Raman spectroscopic study on pressure-induced amorphization in nanocrystalline anatase (TiO_2). *Solid State Commun.* **2001**, *118*, 75−78.
(33) Dubrovinskaia, N. A.; Dubrovinsky, L. S.; Ahuja, R.; Prokopenko, V. B.; Dmitriev, V.; Weber, H.-P.; Osorio-Guillen, J. M.; Johansson, B. Experimental and theoretical identification of a new high-pressure TiO_2 polymorph. *Phys. Rev. Lett.* **2001**, *87*, 275501.
(34) Pischedda, V.; Hearne, G. R.; Dawe, A. M.; Lowther, J. E. Ultrastability and enhanced stiffness of ~ 6 nm TiO_2 nanoanatase and eventual pressure-induced disorder on the nanometer scale. *Phys. Rev. Lett.* **2006**, *96*, 035509.
(35) Swamy, V.; Kuznetsov, A.; Dubrovinsky, L. S.; McMillan, P. F.; Prakapenka, V. B.; Shen, G.; Muddle, B. C. Muddle, B. C. Size-dependent pressure-induced amorphization in nanoscale TiO_2. *Phys. Rev. Lett.* **2006**, *96*, 135702.
(36) Hearne, G. R.; Zhao, J.; Dawe, A. M.; Pischedda, V.; Maaza, M.; Nieuwoudt, M. K.; Kibasomba, P.; Nemraoui, O.; Comins, J. D.; Witcomb, M. J. Effect of grain size on structural transitions in anatase TiO_2: a Raman spectroscopy study at high pressure. *Phys. Rev. B: Condens. Matter Mater. Phys.* **2004**, *70*, 134102.
(37) Swamy, V.; Kuznetsov, A.; Dubrovinsky, L. S.; Caruso, R. A.; Shchukin, D. G.; Muddle, B. C. Muddle, B. C. Finite-size and pressure effects on the Raman spectrum of nanocrystalline anatase TiO_2. *Phys. Rev. B: Condens. Matter Mater. Phys.* **2005**, *71*, 184302.
(38) Swamy, V.; Dubrovinsky, L. S.; Dubrovinskaia, N. A.; Simionovici, A. S.; Drakopoulos, M.; Dmitriev, V.; Weber, H.-P. Compression behavior of nanocrystalline anatase TiO_2. *Solid State Commun.* **2003**, *125*, 111−115.

DOI: 10.1021/acs.jpclett.7b01384
J. Phys. Chem. Lett. 2017, 8, 3249−3255

Bimetallic Ions Codoped Nanocrystals: Doping Mechanism, Defect Formation, and Associated Structural Transition

Qingbo Sun,[†] Changlin Zheng,[∥] Larissa Q. Huston,[‡] Terry J. Frankcombe,[**,#] Hua Chen,[§] Chao Zhou,[▽] Zhenxiao Fu,[▽] Ray L. Withers,[†] Lasse Norén,[†] Jodie E. Bradby,[‡] Joanne Etheridge,[∥,⊥] and Yun Liu[*,†]

[†]Research School of Chemistry, [‡]Research School of Physics and Engineering, and [§]Centre for Advanced Microscopy, The Australian National University, Canberra, Australian Capital Territory 2601, Australia

[∥]Monash Centre for Electron Microscopy and [⊥]Department of Materials Science and Engineering, Monash University, Victoria 3800, Australia

[#]School of Physical, Environmental and Mathematical Sciences, University of New South Wales, Australian Capital Territory, Canberra 2601, Australia

[▽]Fenghua Advanced Technology Holding Co., Ltd., Zhaoqing, Guangdong 526020, China

Supporting Information

SI-1. The synthesis of anatase ($Ti^{4+}_{1-x-y-z}Ti^{3+}_{x}In^{3+}_{y}Nb^{5+}_{z}$)($O^{2-}_{2-(x+y+z)/2}\square_{y/2}$) nanocrystals

Anatase ($Ti^{4+}_{1-x-y-z}Ti^{3+}_{x}In^{3+}_{y}Nb^{5+}_{z}$)($O^{2-}_{2-(x+y+z)/2}\square_{y/2}$) nanocrystals were synthesized under solvothermal conditions. For example, to prepare the codoped nanocrystals with x≈y≈z≈0.046, 0.68 mL $TiCl_4$, 0.092 g $NbCl_5$ and 1.6406 g $In(C_2H_3O_2)_3$ were separately added into 120 mL ethanol solvent to form one transparent solution. This transparent solution was firstly stirred at room temperature for 2 hours and then transferred into an autoclave with the inner volume of about 200 mL. After the sealed autoclave was heated to 200 °C and kept at this temperature for 14 h, the solid product formed in the solution was centrifuged, washed with ethanol and distilled water, and finally dried at 60 °C for 12 h. Following this reaction condition and powder collection route, other ($Ti^{4+}_{1-x-y-z}Ti^{3+}_{x}In^{3+}_{y}Nb^{5+}_{z}$)($O^{2-}_{2-(x+y+z)/2}\square_{y/2}$) anatase nanocrystals with different x≈y≈z values such as 0, 0.010 and 0.030 were also synthesized by adjusting the added weight of $NbCl_5$ and $In(C_2H_3O_2)_3$. The detailed mixed ratios of various raw materials are listed in the **Table S1**.

Table S1. The mixed ratios of various raw materials used to synthesize anatase ($Ti^{4+}_{1-x-y-z}Ti^{3+}_{x}In^{3+}_{y}Nb^{5+}_{z}$)($O^{2-}_{2-(x+y+z)/2}\square_{y/2}$) nanocrystals with different doping concentrations.

($Ti^{4+}_{1-x-y-z}Ti^{3+}_{x}In^{3+}_{y}Nb^{5+}_{z}$)($O^{2-}_{2-(x+y+z)/2}\square_{y/2}$)	$NbCl_5$ (g)	$In(C_2H_3O_2)_3$ (g)	$TiCl_4$ (mL)	CH_3CH_2OH (mL)
x=y=z=0	0	0	0.68	120
x≈y≈z≈0.010	0.039	0.446	0.68	120
x≈y≈z≈0.030	0.053	0.855	0.68	120
x≈y≈z≈0.046	0.092	1.641	0.68	120

SI-2. The characterization of anatase ($Ti^{4+}_{1-x-y-z}Ti^{3+}_{x}In^{3+}_{y}Nb^{5+}_{z}$)($O^{2-}_{2-(x+y+z)/2}\square_{y/2}$) nanocrystals

Anatase ($Ti^{4+}_{1-x-y-z}Ti^{3+}_{x}In^{3+}_{y}Nb^{5+}_{z}$)($O^{2-}_{2-(x+y+z)/2}\square_{y/2}$) nanocrystals synthesized by the solvothermal method were characterized by a X-ray powder diffractometer (XRD, PANalytical's X-ray diffractometer with CuKα radiation, the step size of 0.013° and the time per step of 300s) to confirm their crystal structures. Field-emission transmission electron microscope (TEM, JEOL-2100F) was used to measure their microscopic morphologies and further estimate their average particle sizes. Raman spectra of the resultant powders were collected using a Renishaw Raman System with 532 nm laser. The chemical valences and atomic percentages of cations in the codoped nanocrystals were tested by X-ray photoelectron spectroscopy (XPS). More accurately, the chemical compositions were further carefully confirmed by the scanning electron microscopy (SEM, Hitachi-S4300) attached with the energy dispersive X-ray spectroscopy (EDS) and an inductively coupled plasma optical emission spectrometer (ICP-OES, Vista AX). In addition, the EPR signals of codoped samples were also collected

at room temperature through the electron paramagnetic resonance equipment (EPR, a Bruker ER200D spectrometer), which shows the existence of Ti^{3+} ions. In order to further demonstrate that In^{3+} and Nb^{5+} ions are indeed codoped into nanocrystals, the high-angle annular dark-field scanning transmission electron microscopy (HAADF-STEM, Double-corrected FEI Titan^3 80-300 FEGTEM) were thus taken to characterize the codoping information at the atomic scale.

SI-3. The Bond valence sum calculation of the synthesized $(Ti^{4+}_{1-x-y-z}Ti^{3+}_{x}In^{3+}_{y}Nb^{5+}_{z})(O^{2-}_{2-(x+y+z)/2}\square_{y/2})$ nanocrystals with x=y=z=0.046

The Bond valence sum (BVS) calculation[16-18] was performed for (In^{3+}+Nb^{5+}) codoped anatase TiO_2 with the respective doping concentrations of about 4.6 at% (*i.e.* x≈y≈z≈0.046). The original CIF file of un-doped anatase TiO_2 for the BVS calculation comes from Ref. S1. The calculated results show that the global instability index (GII) value of anatase $(Ti^{4+}_{1-x-y-z}Ti^{3+}_{x}In^{3+}_{y}Nb^{5+}_{z})(O^{2-}_{2-(x+y+z)/2}\square_{y/2})$ with x≈y≈z≈0.046 is about 0.97 v.u. Such a high GII value means that the codoping of In^{3+} and Nb^{5+} ions into anatase TiO_2 is not easy experimentally. Meanwhile, the apparent valence of In^{3+} ions is ~5.33 v.u. and their BVS deviation is ~2.33 v.u. In^{3+} ions are thus about 78% over-bonded if they substitute Ti^{4+} ions of anatase TiO_2 (called "difficult-dopants"). However, the apparent valence of Nb^{5+} ions is ~5.37 v.u. and their BVS deviation is ~0.37 v.u., which indicates that Nb^{5+} ions are only slightly over-bonded (~7.4%). Therefore, the chemical doping of Nb^{5+} ions into anatase TiO_2 should be experimentally much easier (called "easy-dopants") than that of In^{3+} ions.

SI-4. XRD patterns of anatase $(Ti^{4+}_{1-x-y-z}Ti^{3+}_{x}In^{3+}_{y}Nb^{5+}_{z})(O^{2-}_{2-(x+y+z)/2}\square_{y/2})$ nanocrystals

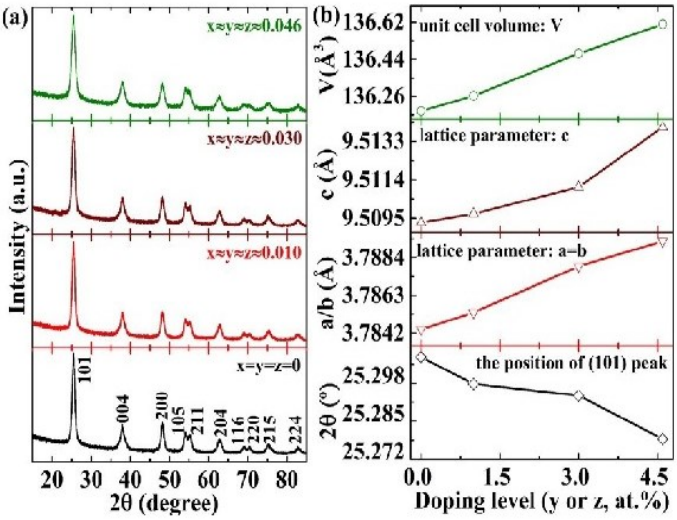

Figure S1. XRD patterns of anatase $(Ti^{4+}_{1-x-y-z}Ti^{3+}_{x}In^{3+}_{y}Nb^{5+}_{z})(O^{2-}_{2-(x+y+z)/2}\square_{y/2})$ nanocrystals with x≈y≈z≈0, 0.010, 0.030 and 0.046, respectively (a). (b) is the changes of their (101) diffraction peak position, lattice parameter (***a***=***b***, ***c***) and unite cell volume (***V***) with the increment of In^{3+} and Nb^{5+} doping levels.

XRD patterns of the synthesized anatase $(Ti^{4+}_{1-x-y-z}Ti^{3+}_{x}In^{3+}_{y}Nb^{5+}_{z})(O^{2-}_{2-(x+y+z)/2}\square_{y/2})$ nanocrystals are shown in **Figure S1**a. All of their diffraction peaks can be assigned to the tetragonal phase with space group symmetry $I4_1/amd$. It is experimentally confirmed that they have the anatase structure. Furthermore, their (101) diffraction peak gradually shifts to lower (2θ) angles with increasing the doping levels of In^{3+} and Nb^{5+} ions (Figure S1b). This shift should be attributed to the bigger ionic radii of In^{3+} (94 pm) and Nb^{5+} (78 pm) ions than that of Ti^{4+} (74.5 pm), partially reflecting that the metal ions are indeed codoped into the host materials. In addition, their lattice parameters (***a***, ***b*** and *c*) and unit cell volumes (***V***) increase almost linearly with the increment of doping levels. For example, comparing with the un-doped samples (i.e. x=y=z=0), ***a*** and ***b*** increase by ~0.13%; ***c*** increases by ~0.05% and ***V*** is up to ~0.31% at x≈y≈z≈0.046. These XRD results not only confirm that the synthesized anatase $(Ti^{4+}_{1-x-y-z}Ti^{3+}_{x}In^{3+}_{y}Nb^{5+}_{z})(O^{2-}_{2-(x+y+z)/2}\square_{y/2})$ nanocrystals are monophasic and have the anatase crystal structure but also provide evidence that In^{3+} and Nb^{5+} ions are codoped into TiO_2 host materials.

SI-5. The chemical compositions of anatase ($Ti^{4+}_{1-x-y-z}Ti^{3+}_{x}In^{3+}_{y}Nb^{5+}_{z}$)($O^{2-}_{2-(x+y-z)/2}\square_{y/2}$) nanocrystals

Table S2. The measured doping levels of In^{3+} and Nb^{5+} ions in ($Ti^{4+}_{1-x-y-z}Ti^{3+}_{x}In^{3+}_{y}Nb^{5+}_{z}$)($O^{2-}_{2-(x+y-z)/2}\square_{y/2}$) nanocrystals by EDS of SEM and ICP-OES.

Samples	The ratio of dopants (In^{3+} and Nb^{5+} ions) to total cations			
($Ti^{4+}_{1-x-y-z}Ti^{3+}_{x}In^{3+}_{y}Nb^{5+}_{z}$)($O^{2-}_{2-(x+y-z)/2}\square_{y/2}$)	EDS of SEM		ICP-OES	
	y (=In/cation, at%)	z (=Nb/cation, at%)	y (=In/cation, at%)	z (=Nb/cation, at%)
x≈y≈z≈0.01	0.011	0.010	0.010	0.010
x≈y≈z≈0.03	0.029	0.030	0.028	0.029
x≈y≈z≈0.046	0.046	0.046	0.043	0.045

The EDS of SEM and ICP-OES are both used to analyze the chemical compositions of the synthesized anatase ($Ti^{4+}_{1-x-y-z}Ti^{3+}_{x}In^{3+}_{y}Nb^{5+}_{z}$)($O^{2-}_{2-(x+y-z)/2}\square_{y/2}$) nanocrystals. Prior to the EDS measurement, ($Ti^{4+}_{1-x-y-z}Ti^{3+}_{x}In^{3+}_{y}Nb^{5+}_{z}$)($O^{2-}_{2-(x+y-z)/2}\square_{y/2}$) nanopowders were firstly pressed into pellets and then sintered at 1400 °C for 20 h in order to achieve dense ceramic pellets. Subsequently, the ceramic pellets were polished to obtain a very smooth surface, following carbon coating to avoid the discharging, which is important to assure the accuracy of the EDS results. In^{3+} and Nb^{5+} codopants were analyzed and presented in terms of their ratios to the total cations. For ICP-OES measurement, the synthesized nanopowders are directly used. The detailed experimental results are listed in **Table S2**. It can be found that the analytic results of the two methods are consistent though different samples are used (i.e. nanopowders for ICP-OES analysis and ceramic pellets for EDS of SEM measurement).

SI-6. Raman spectra of anatase ($Ti^{4+}_{1-x-y-z}Ti^{3+}_{x}In^{3+}_{y}Nb^{5+}_{z}$)($O^{2-}_{2-(x+y-z)/2}\square_{y/2}$) nanocrystals

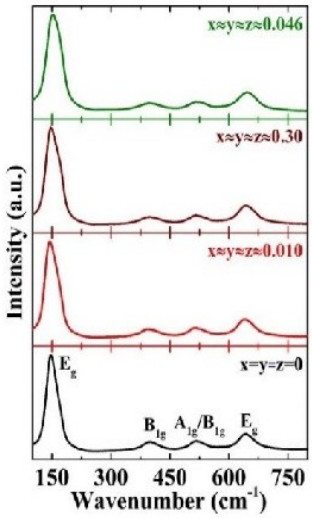

Figure S2. Raman spectra of anatase ($Ti^{4+}_{1-x-y-z}Ti^{3+}_{x}In^{3+}_{y}Nb^{5+}_{z}$)($O^{2-}_{2-(x+y-z)/2}\square_{y/2}$) nanocrystals with x≈y≈z≈0, 0.010, 0.030 and 0.046, respectively, were collected at ambient pressure.

Raman spectra of anatase ($Ti^{4+}_{1-x-y-z}Ti^{3+}_{x}In^{3+}_{y}Nb^{5+}_{z}$)($O^{2-}_{2-(x+y-z)/2}\square_{y/2}$) nanocrystals are presented in **Figure S2**. Four prominent Raman peaks are observed at different x≈y≈z values. They locate at ~149, 397, 517 and 642 cm^{-1}, respectively. These Raman peaks are assigned to different E_g, B_{1g} and A_{1g} active modes, respectively, which is reasonably in agreement with the reported results of un-doped anatase TiO_2 nanoparticles.[23] There is no additional Raman peak found even in the highly-doped samples (*i.e.* y≈z≈0.046), again, suggesting that these anatase ($Ti^{4+}_{1-x-y-z}Ti^{3+}_{x}In^{3+}_{y}Nb^{5+}_{z}$)($O^{2-}_{2-(x+y-z)/2}\square_{y/2}$) nanocrystals are pure phase.

SI-7. Phase contrast TEM lattice images and element mapping of anatase ($Ti^{4+}_{1-x-y-z}Ti^{3+}_{x}In^{3+}_{y}Nb^{5+}_{z}$)($O^{2-}_{2-(x+y+z)/2}\square_{y/2}$) nanocrystals

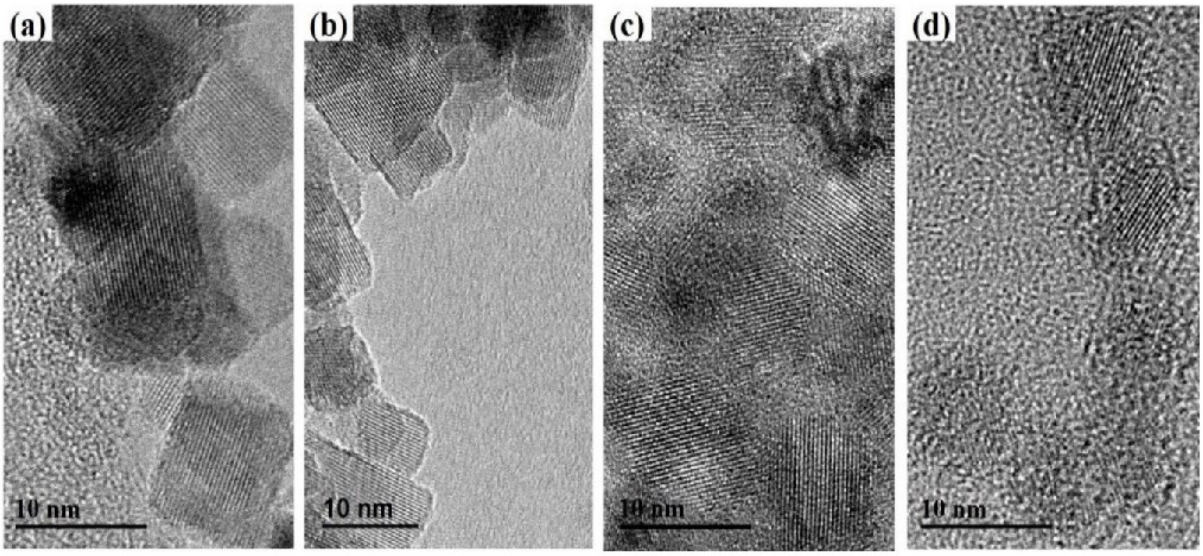

Figure S3. Phase contrast TEM lattice images of anatase ($Ti^{4+}_{1-x-y-z}Ti^{3+}_{x}In^{3+}_{y}Nb^{5+}_{z}$)($O^{2-}_{2-(x+y+z)/2}\square_{y/2}$) nanocrystals with x≈y≈z≈0 (a), 0.010 (b), 0.030 (c) and 0.046 (d), respectively.

Phase contrast TEM lattice images of the synthesized anatase ($Ti^{4+}_{1-x-y-z}Ti^{3+}_{x}In^{3+}_{y}Nb^{5+}_{z}$)($O^{2-}_{2-(x+y+z)/2}\square_{y/2}$) nanocrystals are presented in **Figure S3**. Two different types of morphologies can be observed when the doping concentrations increase from 0 to 4.6 at%. At lower doping levels such as x≈y≈z≈0 or 0.010, they are mainly composed of nanocubes or nanocuboids (Figure S3a and Figure S3b). At higher codoping levels such as x≈y≈z≈0.030 or 0.046, most of nanocubes or nanocuboids change to quasi-spherical shapes (Figure S3c and Figure S3d). Since the codoping of In^{3+} and Nb^{5+} ions affects the crystal structure of anatase TiO_2 by greatly prolonging the lengths of ***a/b*** direction but almost keeping that of ***c*** direction un-changed (Figure S1b), this is a decisive factor for their morphological evolution at different codoping concentrations (i.e. different y or z values). In addition, Figure S3 also presents that the average particle size of these codoped nanocrystals slightly changes at different codoping levels (the higher doping levels, the smaller particle sizes), but remain less than 10 nm. The detailed information about their average particle size are listed in the **Table S3**.

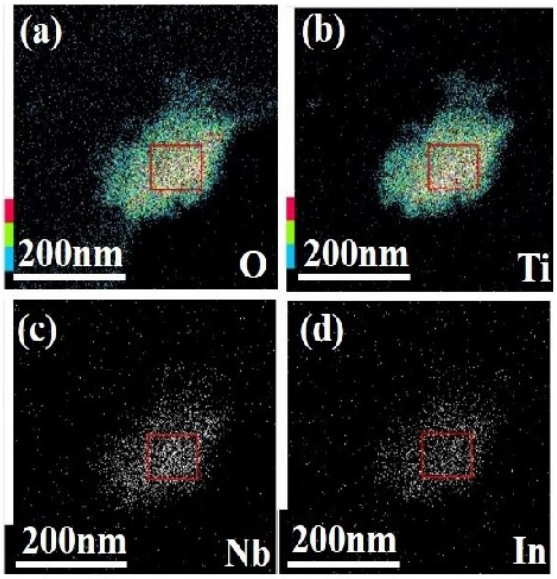

Figure S4. The element mapping of anatase ($Ti^{4+}_{0.862}Ti^{3+}_{0.046}In^{3+}_{0.046}Nb^{5+}_{0.046}$)($O^{2-}_{1.977}\square_{0.023}$) nanocrystals with the highest doping levels of codopants using the STEM mode.

To investigate the homogeneous distribution and the effective incorporation of codopants (In^{3+}+Nb^{5+}), the elemental mapping, *i.e.* Ti, O, In and Nb, was conducted in the $(Ti^{4+}_{0.862}Ti^{3+}_{0.046}In^{3+}_{0.046}Nb^{5+}_{0.046})(O^{2-}_{1.977}\square_{0.023})$ nanocrystal experimentally with the highest doping level (**Figure S4**). It is noticed that the element mapping is technologically difficult in one single nanoparticle since (1) the crystallite size of our synthesized nanoparticles are too small (less than 10 nm); and (2) the weak signals are generated by In^{3+}, Nb^{5+}, Ti^{4+} and O^{2-} ions. Instead, the elements were mapped in agglomerated nanoparticles. It seems that the In^{3+} and Nb^{5+} codopants are homogeneously distributed in codoped nanoparticles, suggesting that our synthesized nanoparticles are (In^{3+}+Nb^{5+}) codoped anatase TiO_2 nanocrystals other than the simple mixture of impurities and TiO_2.

SI-8. The average crystallite size of anatase $(Ti^{4+}_{1-x-y-z}Ti^{3+}_{x}In^{3+}_{y}Nb^{5+}_{z})(O^{2-}_{2-(x+y+z)/2}\square_{y/2})$ nanocrystals

Table S3. The average crystallite size of anatase $(Ti^{4+}_{1-x-y-z}Ti^{3+}_{x}In^{3+}_{y}Nb^{5+}_{z})(O^{2-}_{2-(x+y+z)/2}\square_{y/2})$ nanocrystals calculated by the Scherrer equation and estimated according to their TEM lattice images.

Samples	XRD Results			TEM Results
$(Ti^{4+}_{1-x-y-z}Ti^{3+}_{x}In^{3+}_{y}Nb^{5+}_{z})(O^{2-}_{2-(x+y+z)/2}\square_{y/2})$	2θ (°)	β	D (nm)	D (nm)
x=y=z=0	25.31	1.00	8.15	8.55
x≈y≈z≈0.010	25.30	1.00	8.15	7.75
x≈y≈z≈0.030	25.29	1.04	7.83	8.01
x≈y≈z≈0.046	25.28	1.26	6.46	6.40

Table S3 shows the average particle size of the synthesized $(Ti^{4+}_{1-x-y-z}Ti^{3+}_{x}In^{3+}_{y}Nb^{5+}_{z})(O^{2-}_{2-(x+y+z)/2}\square_{y/2})$ nanocrystals calculated by the Scherrer equation and more accurately estimated by their TEM pictures of **Figure S3**. For the Scherrer equation $D=K\lambda/(\beta\cos\theta)$, D is the average particle size, K is a dimensionless shape factor (0.9), λ is the wavelength of Cu Kα X-ray (0.154056 nm), β is the line broadening at half the maximum intensity (FWHM) and θ is the Bragg angle. Here, the Bragg angles of the (101) diffraction peak are used since they are the strongest peak. θ and β values come from the refinement of their XRPD patterns by Jana 2006.[S2]

SI-9. DFT calculations

DFT calculations were performed with the PAW method as implemented in VASP. The DFT+U approach was used with the PBE functional and effective U-J parameters of 7.4 eV and 5.4 eV applied to the d and p electrons of the metal ions and oxygen ions, respectively. The PAW potentials for Ti, O, In and Nb treated 12, 6, 13 and 13 electrons as valance, respectively. The plane wave energy cutoff was 500 eV and a 2×2×2 Γcentred grid was used for k-point sampling with the tetrahedron method. All calculations were spin polarized and the presence of Ti^{3+} ions was analyzed by examining the spin density within spheres around each ion. Both ionic coordinates and lattice parameters were relaxed to determine the energies of each considered defect structure.

SI-10. High-pressure reaction

A diamond anvil cell with a cullet size of 400 μm was employed to investigate the high-pressure behavior. A stainless steel gasket was indented to a thickness of 30 μm and a 200 μm diameter hole was drilled at the center. It served as the sample chamber. (In^{3+}+Nb^{5+}) codoped anatase TiO_2 nanopowders and two small ruby balls were loaded into the above chamber. The mixture of 4 parts of ethanol and one part of methanol were used as the pressure transmitting medium within the cell. The sample was carefully loaded to 46.2 GPa in small steps. The pressure inside the diamond cell was determined by the pressure dependent shift of the ruby fluorescence R1 line.[S3] In situ Raman measurements were taken using a Renishaw inVia Reflex Spectrometer System (532 nm laser).

References

[S1] Djerdj, I.; Tonejc A. M. Structural investigations of nanocrystalline TiO_2 samples. *J. Alloys Compd.* **2006**, *413*, 159-174.

[S2] The related information about Jana 2006 software for the refinement of XRD patterns is available in the website of http://jana.fzu.cz/.

[S3] Dewaele, A.; Torrent, M.; Loubeyre, P.; Mezouar, M. Compression curves of transition metals in the Mbar range: experiments and projector augmented-wave calculations. *Phys. Rev. B Condens. Matter Mater. Phys.* **2008**, *78*, 104102.

3.4 Highly efficient visible light catalysts driven by Ti^{3+}-V_O-2Ti^{4+}-N^{3-} defect clusters

I wrote the draft of this paper. I developed an approach for synthesizing TiO_2 samples containing N^{3-} and Ti^{3+} ions. I characterized the related samples using XRD, Raman spectroscopy, HRTEM, SEM/EDS, XPS, UV-VIS, N-O determinator, TGA-DSC and others. I also analyzed the related results of DFT calculations performed by Terry J. Frankcombe and David Cortie, and the results of photocatalytic measurement conducted by Shaoyang Zhang.

Highly Efficient Visible Light Catalysts Driven by Ti^{3+}-V_O-2Ti^{4+}-N^{3-} Defect Clusters

Qingbo Sun[a], Shaoyang Zhang[b], David Cortie[a,c], Terry J. Frankcombe[d], Jie Gao[e], Hua Chen[f], Ray L. Withers[a], Felipe Kremer[f], Dehong Yu[c], Frank Brink[f], Wensheng Shi[b] and Yun Liu[a,*]

[a] Research School of Chemistry, [f] Centre for Advanced Microscopy, The Australian National University, Canberra, Australian Capital Territory, 2601, Australia.

[b] Technical Institute of Physics and Chemistry, Chinese Academy of Sciences, Beijing, 100190, China.

[c] The Australian Nuclear Science and Technology Organisation, Lucas Height, New South Wales, 2234, Australia.

[d] School of Physical, Environmental and Mathematical Sciences, University of New South Wales, Canberra, Australian Capital Territory, 2601, Australia.

[e] Analysis and Testing Centre for Inorganic Materials, Shanghai Institute of Ceramics, Chinese Academy of Sciences, Shanghai, 200050, China.

Keywords: Defect cluster, Doping, TiO_2, Visible light catalysts, Solvothermal reaction.

Abstract. Local defect structures play significant roles on material properties, but they are seriously neglected in the design, synthesis, and development of highly efficient TiO_2-based visible light catalysts. Here, we take (Ti^{3+}, N^{3-}) co-doped anatase TiO_2 nanocrystals with the complicated chemical formula of $(Ti^{4+}_{1-x}Ti^{3+}_x)(O^{2-}_{2-y-z}N^{3-}_y\square_z)$ as an example and point out that the formation of Ti^{3+}-V_O-2Ti^{4+}-N^{3-} local defect clusters is a key missing step for significantly enhancing visible light catalytic properties of host TiO_2 nanocrystals. Experimental and theoretical investigations also demonstrate the emergent behaviours of these intentionally introduced defect clusters for developing highly efficient visible light catalysts. This research thus not only provides highly efficient visible light catalysts for various practical applications but also addresses the significance of local defect structures

* Corresponding author: Professor Yun Liu; E-mail: yun.liu@anu.edu.au.

on modifying material properties.

Introduction

The development of highly efficient visible light catalysts (VLCs) can help to alleviate
the serious environmental pollution and overcome the current energy crisis since they can directly harness visible light from the solar spectrum to drive a range of catalytic reactions such as generating hydrogen from water, degrading organic pollutants or removing hazardous chemicals in wastewater and air. To develop highly efficient TiO_2-based VLCs, various strategies are attempted to date, for instance, cation/anion mono-doping,[1,2] cation-cation/cation-anion/anion-anion co-doping,[3-5] noble metal element modifying[6,7] as well as multi-compositional mixing.[8,9] The former two chemically incorporate dopants or co-dopants into host TiO_2 crystal structures while the latter two physically add another species on material surfaces. The improved VLC properties are then attributed to either the adjustment of the band structure of materials, or the generation of surface plasma resonance effects, or the introduction of secondary species themselves. Although these strategies represent a substantial progress in the research and development of TiO_2-based VLCs, most of them are only active in a certain solar spectral region or only moderately improve VLC properties.

More recent efforts for achieving highly efficient VLCs have been made on N^{3-} mono-doped or Ti^{3+} self-doped TiO_2 materials since it is generally believed that the hybridization of N 2*p* and O 2*p*, or Ti^{4+} 3*d* and Ti^{3+} 3*d* orbitals enables narrowing the bandgap, extending light absorption and thus enhancing VLC efficiency.[1,10-14] However, the results are not consistent. Some researchers reported that N^{3-} ions mono-doping or Ti^{3+} ions self-doping significantly enhanced VLC efficiency[1,10-12] while others found that they were only slightly effective or even completely ineffective.[13,14] Furthermore, the mechanisms underlying VLC effects are also ambiguous. The formation of isolated states between forbidden bands,[14,15] multiple light reflections from material hierarchical structures,[12] the introduction of oxygen vacancies,[13] the optical intragap absorption,[5] as well as the appearance of a diamagnetic cluster[16] were all suggested as potential mechanisms for those observed photocatalytic phenomena. From a structural perspective, N^{3-} mono-doping or Ti^{3+} self-doping will concurrently introduce oxygen vacancies into TiO_2

for charge balance and then inevitably deteriorate photocatalytic performances through forming "recombination centres" to trap photo-excited carriers. To achieve higher VLC performances, special material structural designs, for example, lattice-disorder engineering of nanocrystalline surfaces,[10] deliberately surficial doping,[12] passivated co-doping,[17] and compositional gradient distribution of dopant ions[4] are normally further required and thus lead to a technological difficulty in their controllable preparation.

Simultaneous incorporation of Ti^{3+} and N^{3-} ions into TiO_2 is an effective and promising way to prepare novel TiO_2-based VLCs. This is because (1) additional cationic dopants are not involved in contrast to other (cation, N^{3-}) co-doping methods; (2) N^{3-} doping levels may be increased significantly by generating some synergistic effects with Ti^{3+} ions; (3) special material structural designs are not required to effectively separate photo-generated charge carriers; and (4) VLC performances of resultant materials can be enhanced exponentially compared to their respective mono-doping cases. Although the simultaneous introduction of Ti^{3+} and N^{3-} into TiO_2 has so many potential advantages, its chemical synthesis is still technologically difficult. Hydrogenation and nitridation co-treatment of rutile TiO_2 nanowire arrays,[18] calcination and subsequent vacuum activation of amorphous precipitates pre-prepared by a sol-gel technique,[19] and direct solvothermal reaction synthesis using diethylentriamine as a nitrogen source[20] were all attempted. These routes not only need complex experimental processes or long reaction periods but also result in a low N^{3-} doping level ($\leq$ 2at.%), a non-equivalent Ti^{3+}/N^{3-} ratio or an inhomogeneous distribution of Ti^{3+} and N^{3-} ions. This leaves an uncertainty as to whether the improved photocatalytic activity is really determined or dominated by the introduction of Ti^{3+} and N^{3-} ions. Our recent work on the development of highly efficient TiO_2-based VLCs demonstrated the significance of introducing a high but equal concentration of (N^{3-}, Nb^{5+}) defect pairs for outstanding photocatalytic properties.[21] This, in combination with our previous research on (In^{3+}, Nb^{5+}) and (Al^{3+}, Nb^{5+}) co-doped rutile TiO_2 ceramics with excellent dielectric properties,[22,23] suggests the complexity of ionic co-doping in structurally strongly correlated oxides. The introduced extrinsic ions may stay as isolated point defects in host materials and may also form defect-pairs or clusters coupled with the host ions and local crystal structures. The former presents an additive effect of point defects while the latter leads to significant synergistic behaviours. The defect formation strongly depends on the selection of extrinsic ions, the preparation conditions and the methods used for material synthesis.

Here, we strategically design a new approach to simultaneously incorporate Ti^{3+} and N^{3-} ions into TiO_2 with high and nearly equal concentrations for a real synergistic interaction between the introduced cations and anions. That is, Ti^{3+} and N^{3-} ions are simultaneously introduced into TiO_2 crystal structures under solvothermal reaction conditions using concentrated nitric acid as a nitrogen source, titanium tetrachloride as the initial source of Ti^{4+} and Ti^{3+} ions, and ethanol as solvent. The vigorous chemical reaction of concentrated nitric acid with ethanol not only releases significantly high energy to the reaction system but also yields the high N^{3-} doping levels. This route also enables related chemical reactions to occur in a close, high pressure and relatively low temperature environment, directly achieves crystalline TiO_2 materials, and effectively prevents nitrogen loss from unnecessary post-treatments. The solvothermal products synthesized thereof were then characterized as VLCs for purifying wastewater using Rhodamine B as a model pollutant. Density functional theory (DFT) calculations were performed to understand the observed photocatalytic effects and the related mechanisms arising from the formation of local defect clusters. This research demonstrates the importance of local defect structures on material performances and provides a novel route to design and develop visible light catalysts for highly efficient conversion of solar energy.

MATERIALS AND METHODS

(Ti^{3+}, N^{3-}) co-doped anatase TiO_2 nanocrystals with the complex chemical formula of $(Ti^{4+}_{1-x}Ti^{3+}_{x})(O^{2-}_{2-y-z}N^{3-}_{y}\square_{z})$ were synthesized by a solvothermal method. In details, $TiCl_4$ (0.68 mL) was first added into ethanol (120 mL) solvent to form a transparent solution under magnetically stirring. Concentrated HNO_3 (69%, 4 mL) were then added into the transparent solution in order to effectively introduce a nitrogen source into the reaction solution. After the above mixture was stirred for two hours at room temperature, it was transferred into an autoclave with an inner volume of about 200 mL. The autoclave was sealed and heated at 200 °C for 12 h in an oven. When the autoclave cooled down to room temperature, the solvothermal product synthesized in the reaction solution was separated by a centrifuge (20,000 rpm), washed with ethanol and distilled water for five times, and finally dried at 60 °C for 12 h. The optimized chemical compositions are x≈0.0381, y≈0.0305 and z≈0.0343, respectively [*i.e.* $(Ti^{4+}_{0.9619}Ti^{3+}_{0.0381})(O^{2-}_{1.9352}N^{3-}_{0.0305}\square_{0.0343})$]. Note: the volume of ethanol should be far more than that of concentrated HNO_3 and only the latter can be slowly added into the former under magnetically stirring in order to effectively prevent their too vigorous reaction.

(Ti^{3+}, N^{3-}) co-doped anatase TiO_2 nanocrystals synthesized thereof were analysed by X-ray diffractometer (XRD, PANalytical's X-ray diffractometer with CuKα radiation at the voltage of 45 V, the current of 40 mA, the step size of 0.013° as well as the time per step of 300s), high-resolution transmission electron microscope (HRTEM, JEOL-2100F at the acceleration voltage of 200 kV), and UV-Vis-NIR spectrophotometer (Varian, Cary 5G with the average time of 0.1s, the data interval of 1 nm and the scan rate of 600 nm per minute). The chemical valence and atomic percentage of N and Ti in the prepared nanocrystals were carefully analysed by X-ray photoelectron spectroscopy (XPS, Thermo ESCALAB250Xi) and electron paramagnetic resonance spectrometer (EPR, a Bruker ER200D spectrometer). Moreover, a Nitrogen/Oxygen (N/O) determinator (TC-600, LECO in Helium gas with the flowing velocity of 450 mL per minute) was also used to estimate the nitrogen doping levels. The thermogravimetric (TG) data were collected by STA 8000 (PerkinElmer) with a heating rate of 5 °C per minute in the flowing air (20 mL per minute) to understand the stability and doping concentrations of nitrogen in the samples. The specific surface area was measured through the Brunauer-Emmett-Teller (B.E.T.) method with a QuadraSorb SI-MP instrument. Prior to the measurement, the samples were degassed in vacuum at 423 K for 8 hours. The nitrogen adsorption-desorption data were then recorded at a liquid nitrogen temperature (~77 K). In addition, organic groups on the surfaces of synthesized nanocrystals were carefully measured by a Fourier transform infrared spectroscopy (FT-IR, PerkinElmer) after the achieved samples were buried into KBr pellets.

Rhodamine B (RhB) was chosen as a model organic compound to evaluate the photocatalytic activities of our synthesized (Ti^{3+}, N^{3-}) co-doped anatase TiO_2 nanocrystals. RhB solution (20 mg L^{-1}) was prepared by mixing RhB (20 mg) with distilled water (1 L). Then, (Ti^{3+}, N^{3-}) co-doped TiO_2 photocatalysts were added into the RhB solution with a mass concentration of 1 g L^{-1}. A 500 W Xe lamp with a 400 nm cut-off filter provided visible light irradiation for photocatalytic measurement. The solution containing RhB and photocatalysts was stirred for 30 minutes in dark to reach RhB adsorption/desorption equilibrium on the surfaces of synthesized anatase TiO_2 nanocrystals, after which the photocatalytic reaction was initiated by illumination (time=0). The decomposition of RhB was characterized by a UV-Vis-NIR spectrometer based on a typical RhB peak at ~552 nm.

Projector-augmented wave (PAW) calculations were performed using the VASP code.[24,25] A plane wave cutoff of 500 eV was used, with PAW potentials[26] that treat

12, 6 and 5 electrons as valence for Ti, O and N, respectively. Hubbard corrections (DFT+U) were applied with effective U parameters of 7.4 eV for Ti d electrons and 5.4 eV for O and N p electrons. All calculations were spin polarised. Oxidation states were identified by examining angular momentum resolved spin densities in spheres centred on the nuclei. Calculations were performed on a 3×3×1 supercell of the anatase crystallographic unit cell (108 atoms). A 2×2×2 Γ-centred k-point grid was used. The lattice was kept fixed at that optimised for pure anatase using the same computational procedure (a=3.8783 Å, c=9.7701 Å). All results are reported for relaxed ionic positions with no constraints. After structural relaxation, the densities of electronic states were calculated using an accurate all-electron method as implemented in the WIEN2K software.[27] Spin polarised calculations were performed to account for the local moment found on certain Ti atoms. The atomic sphere sizes were set to 1.85, 1.69 and 1.59 atomic units (A.U.) for Ti, O and N, respectively. A 5x5x7 Γ-centred k-point grid was used. Owing to the large size of the supercell cell (71 unique atoms), the plane wave basis was constrained to the maximum value within available memory (RKMax=6.1). Convergence tests on smaller systems using RKMax between 6 and 8 indicate that the lower value is reasonable since the gap is accurate to within 0.1 eV. For the final electronic structure, calculations were made using the sophisticated modified-Becke-Johnson (mBJ) potential that allows a parameter-free method to accurately predict experimental bandgaps, which substantially improves on the Kohn-Shan bandgaps predicted by standard DFT methods.[28] The optical absorption coefficient was then calculated using the joint density of states for both the spin-up and spin-down component, weighted by the respective dipole matrix elements.[29] Only inter-band contributions were considered. The absorption coefficient was calculated from the real and imaginary dielectric constant of the Kramers-Kronig transformation.

RESULTS AND DISCUSSION

The XRD pattern of Figure 1a shows that the synthesized solvothermal products have an anatase phase with space group symmetry *I*41/*amd*. Their diffraction peaks are very broad, suggesting the feature of small particle sizes. The calculated results of the Scherrer equation[30] further demonstrate this small feature of synthesized nanoparticles with an average crystal size of ~7.7 nm (Supporting Information, SI-1), which is reasonably consistent to the estimated results of HRTEM lattice images (Figure 1b and SI-2). From the optical photograph in the insert of Figure 1a, we find that the synthesized

nanoparticles are pale yellow. This colour indicates the underlying visible light absorption (as discussed below). From a $\langle 11\bar{1} \rangle$ oriented HRTEM lattice image (Figure 1b), it is found that the exposed crystal faces of synthesized nanocrystals are (011), (101) and (112) facets, respectively. In addition, these nanoparticles have a specific surface area of 122.7 m^2/g in terms of the result of nitrogen absorption and desorption experiment (SI-3).

The TGA curve in Figure 1c shows that the weight of synthesized nanoparticles firstly decreases (~0.54 wt.%) as the temperature increases from 450 to 727 °C and then continuously increases (~0.22 wt.%) in the temperature range of 727 and 1100 °C. Prior to 450 °C, their weight drops significantly (~13.7 wt.%, SI-4). Such a large low temperature weight loss comes from the removal of physically adsorbed water and/or ethanol, chemically bonded hydroxyl and other organic groups, as confirmed by the FT-IR spectroscopy (SI-5). The small weight loss at higher temperatures (450-727°C), however, should be related to the release of chemically doped nitrogen ions since (1) un-doped TiO_2 normally has no or negligible weight variation in this temperature range;[31-34] and (2) organic groups chemically bonded on nanoparticle surfaces generally do not survive at such a high temperature. Meanwhile, a ~0.54 wt.% nitrogen content corresponds to an atomic percentage of ~3.05 at.% (i.e. y≈0.0305) and is in reasonable consistency with the measurement result of a Nitrogen/Oxygen determinator (~2.99 at.%). Further XPS analysis also confirms the existence of N^{3-} dopants through their N 1*s* XPS peak (Figure 1e). Above 727 °C, the 0.22 wt.% weight increase can be attributed to the incorporated oxygen ions at the initial lattice sites of oxygen vacancies or the newly formed positions due to nitrogen release. The O 1*s* XPS peak at ~530.3 eV also reflects a lower oxygen content (~1.9352) in contrast to the standard stoichiometric ratio 2 of un-doped TiO_2 (Figure 1f). This is consistent with the TGA results (Figure 1c) and suggests that oxygen vacancies are produced for charge balance (~3.43 at.%, z≈0.0343). Additionally, we detect the XPS signal of Ti^{3+} ions with a concentration of ~3.81 at.% (x≈0.0381, Figure 1d). The presence of Ti^{3+} ions is also confirmed by EPR (electron paramagnetic resonance, SI-6). It is thus evident that the nanocrystals have a chemical formula of $(Ti^{4+}_{0.9619}Ti^{3+}_{0.0381})(O^{2-}_{1.9352}N^{3-}_{0.0305}\square_{0.0343})$. The slightly higher N^{3-} doping level achieved here than N^{3-} mono-doping samples should benefit from the synergistic roles of Ti^{3+} ions and the designed solvothermal reaction route.

Figure 2a shows the optical absorption spectra of $(Ti^{4+}_{0.9619}Ti^{3+}_{0.0381})(O^{2-}_{1.9352}N^{3-}_{0.0305}\square_{0.0343})$ anatase nanocrystals. Their light absorption

range is very broad and covers the entire visible light regime from 400 nm to 800 nm. Their bandgap calculated through the Tauc plot is ~2.63 eV (the insert of Figure 2a) and becomes narrower than the previously reported (Ti^{3+}, N^{3-}) co-doped nanomaterials.[18-20] These phenomena demonstrate the significance of introducing highly concentrated Ti^{3+} and N^{3-} ions into TiO_2 crystal structures. Visible light catalytic efficiency is then evaluated by measuring the decomposition rate of Rhodamine B (RhB), using a 500W Xe lamp with a cutoff wavelength of 400 nm. RhB is one type of potential carcinogen and cannot self-degrade under visible light irradiation (SI-7). It is also difficult to quickly decompose using the commercial P25-TiO_2 photocatalysts (SI-7). The $(Ti^{4+}_{0.9619}Ti^{3+}_{0.0381})(O^{2-}_{1.9352}N^{3-}_{0.0305}\square_{0.0343})$ nanocrystals, however, show an excellent visible light catalytic activity (Figure 2b). As seen, it only takes about 20 minutes to accomplish nearly complete decomposition after an initial adsorption/ desorption equilibrium in dark conditions (the adsorption amount of RhB is ~10%, stabilizing within 30 minutes). They show a high catalytic efficiency and are about 13.4 times faster in contrast to P25 (Table 1). It is thus claimed that the simultaneous introduction of Ti^{3+} and N^{3-} ions is an effective strategy to improve the visible light catalytic activity of host TiO_2 materials.

To understand the electronic structure of the $(Ti^{4+}_{0.9619}Ti^{3+}_{0.0381})(O^{2-}_{1.9352}N^{3-}_{0.0305}\square_{0.0343})$ material or the potential mechanisms of their enhanced VLC performance, DFT calculations were performed using the VASP code in a 3×3×1 supercell. One O^{2-} anion in the anatase TiO_2 crystal structure was substituted by one N^{3-} ion and an additional oxygen vacancy created in various configurations, giving a N^{3-} doping level of 2.78 at.%, which is close to the experimental value of this work (3.05 at.%). Figure 3a shows the lowest energy defect structure among various configurations (structure 1, ST-1). It is composed of one Ti^{3+}, two penta-coordinated Ti^{4+}, one V_O left after the removal of O as well as one N^{3-} binding to one of the two penta-coordinated Ti^{4+} cations. Ti^{3+}-V_O-2Ti^{4+}-N^{3-} defect clusters are then formed locally in anatase TiO_2 crystal structure. Structure 2 (ST-2) of Figure 3b also presents the similar defect clusters as ST-1, but its N^{3-} ion just bridges two penta-coordinated Ti^{4+} cations, leading to a ~0.058 eV higher total energy than structure 1. Other configurations either lie at too high total energy to be present in significant numbers experimentally or do not match the chemical composition of our samples (e.g. Ti^{3+} ions cannot be found in the

calculation of the scenario of interstitial nitrogen.). Therefore, they are not discussed here.

These two different defect structures significantly modify the electronic structure of TiO_2. Figure 3c exhibits the calculated total density of states (DOS) for ST-1 and ST-2. Their bandgaps are both narrowed to about 2.79 eV in contrast to 2.98 eV of un-doped anatase TiO_2 and are in reasonable accordance with their results of optical absorption measurement (Figure 2a). However, we further find one newly formed mid-gap energy level in the bandgaps. It is shallower in ST-1 and locates ~0.38 eV above the top of valence band, but slightly deeper in ST-2 and locates ~0.75 eV above the top of valence band. The narrowed bandgap and newly introduced mid-gap energy level result in the visible light absorption of the $(Ti^{4+}_{0.9619}Ti^{3+}_{0.0381})(O^{2-}_{1.9352}N^{3-}_{0.0305}\square_{0.0343})$ nanocrystals.

In addition, we have calculated the optical absorption coefficient in an attempt to directly observing the enhanced visible light absorption by introducing Ti^{3+}-V_O-$2Ti^{4+}$-N^{3-} defect clusters (Figure 3d). Two absorption tensor components (xx and zz) demonstrate their finite absorption into the visible light regions. Moreover, ST-2 has a stronger visible light absorption ability than ST-1, though the latter is thermodynamically preferred. It is thus clear that the introduction of Ti^{3+}-V_O-$2Ti^{4+}$-N^{3-} defect clusters in anatase TiO_2 host materials is critical to enhance visible light absorption of TiO_2 and is then necessary for outstanding visible light catalytic performances.

CONCLUSION

In conclusion, Ti^{3+} and N^{3-} ions are successfully incorporated into anatase TiO_2 crystal structure through a novel solvothermal reaction route. These introduced extrinsic ions and associated oxygen vacancies locally generate Ti^{3+}-V_O-$2Ti^{4+}$-N^{3-} defect clusters for narrowing the bandgap, forming midgap energy level and thus enhancing VLC properties of host TiO_2 materials. The concept, design strategy and synthesis method of highly efficient visible light catalysts driven by defect clusters will provide a guidance for the further development of other photocatalytic materials and also brings new insights for the significance of local defect structures on modifying material properties.

ACKNOWLEDGEMENTS

Q. Sun, D. Cortie, T. J. Frankcome and Y. Liu acknowledge the supports of the Australian Research Council in the form of Discovery Projects and the ARC Future Fellowships program. S. Zhang and W. Shi thank the support from CAS (XDB17030000) and MOST of China (2016YFA0200800). The authors acknowledge the facilities, the scientific, technical assistance of the Australian microscopy and microanalysis research facility at the Centre of advanced Microscopy (ANU).

AUTHORS' CONTRIBUTION

QS, DCo, YL, WS and TJF make the main contribution to the preparation of this manuscript. YL initiated this research, planned and coordinated all experimental and theoretical work. WS and TJF supervised the photocatalytic and theoretical work collaborated with YL. QS developed the approach for the fabrication of the samples with different compositions and synthetic conditions. SZ and QS conducted the photocatalytic experiment. DCo conducted theoretical calculation, collaborated with YL and TJF. QS, RLW, FK and FB conducted HRTEM, SEM/EDS, XPS and light absorption with the assistance of HC and DY. JG and QS conducted the chemical composition analysis relevant to nitrogen. All authors were involved in the data analysis and discussion as well as manuscript preparation.

REFERENCES

[1] Asahi, R., Morikawa, T., Ohwaki, T., Aoki, K. & Taga, Y. Visible-light photocatalysis in nitrogen-doped titanium oxides. *Science* **293**, 269-271 **(2001)**.

[2] Liu, B., Chen, H. M., Liu, C., Andrews, S. C., Hahn, C. & Yang, P. Large-scale synthesis of transition-metal-doped TiO_2 nanowires with controllable overpotential. *J. Am. Chem. Soc.* **135**, 9995-9998 (2013).

[3] Kato, H. & Kudo, A. Visible-light-response and photocatalytic activities of TiO_2 and $SrTiO_3$ photocatalysts codoped with antimony and chromium. *J. Phys. Chem. B* **106**, 5029-5034 (2002).

[4] Liu, G., Yin, L.-C., Wang, J., Niu, P., Zhen, C., Xie, Y. & Chen, H.-M. A red anatase TiO_2 photocatalyst for solar energy conversion. *Energy Environ. Sci.* **5**, 9603-9610 (2012).

[5] Asahi, R., Morikawa, T., Irie, H. & Ohwaki, T. Nitrogen-doped titanium dioxide as visible-light-sensitive photocatalyst: designs, developments, and prospects. *Chem. Rev.* **114***,* 9824-9852 (2014).

[6] Ansari, S. A. & Cho, M. H. Highly visible light responsive, narrow band gap TiO_2 nanoparticles modified by elemental red phosphorus for photocatalysis and photoelectrochemical applications. *Sci. Rep.* **6**, 25405 (2016).

[7] Méndez-Medrano, M. G., Kowalska, E., Lehoux, A., Herissan, A., Ohtani. B., Rau, S., Colbeau-Justin, C., Rodríguez-López, J. L. & Remita, H. Surface modification of TiO_2 with Ag nanoparticles and CuO nanoclusters for application in photocatalysis. *J. Phys. Chem. C* **120**, 25010-25022 (2016).

[8] Xiang, Q., Yu, J. & Jaroniec, M. Synergetic effect of MoS_2 and graphene as cocatalysts for enhanced photocatalytic H_2 production activity of TiO_2 nanoparticles. *J. Am. Chem. Soc.* **134**, 6575-6578 (2012).

[9] Lee, J. S., You, K. H. & Park, C. B. Highly photoactive, low bandgap TiO_2 nanoparticles wrapped by graphene. *Adv. Mater.* **24**, 1084-1088 (2012).

[10] Chen, X. & Mao, S. S. Titanium dioxide nanomaterials: synthesis, properties, modifications, and applications. *Chem. Rev.* **107**, 2891-2959 (2007).

[11] Cong, Y., Zhang, J., Chen, F. & Anpo, M. Synthesis and characterization of nitrogen-doped TiO_2 Nnanophotocatalyst with high visible light activity. *J. Phys. Chem. C* **111**, 6976-6982 (2007).

[12] Ren, R., Wen, Z., Cui, S., Hou, Y., Guo, X. & Chen, J. Facile synthesis of defective TiO_{2-x} nanocrystals with high surface area and tailoring bandgap for visible-light photocatalysis. *Sci. Rep.* **5**, 10714-10724 (2015).

[13] Nakano, Y., Morikawa, T., Ohwaki, T. & Taga, Y. Deep-level optical spectroscopy investigation of N-doped TiO_2 films. *Appl. Phys. Lett.* **86**, 132104 (2005).

[14] Kumar, R., Govindarajan, S., Janardhana, R. K. S. K., Rao, T. N., Joshi, S. V. & Anandan, S. Facile one-step route for the development of in situ cocatalyst-modified Ti^{3+} self-doped TiO_2 for improved visible-light photocatalytic activity. *ACS Appl. Mater. Interfaces* **8**, 27642-27653 (2016).

[15] Liu, M., Qiu, X., Miyauchi, M. & Hashimoto, K. Cu(II) oxide amorphous nanoclusters grafted Ti^{3+} self-doped TiO_2: an efficient visible light photocatalyst. *Chem. Mater.* **23**, 5282-5286 (2011).

[16] Zhang, Z., Wang, X., Long, J., Gu, Q., Ding, Z. & Fu, X. Nitrogen-doped titanium dioxide visible light photocatalyst: spectroscopic identification of photoactive centers. *J. Cataly.* **276**, 201-214 (2010).

[17] Gai, Y. Q., Li, J. B., Li, S. S., Xia, J. B. & Wei, S. H. Design of narrow-gap TiO_2: a passivated codoping approach for enhanced photoelectrochemical activity. *Phys. Rev. Lett.* **102**, 036402 (2009).

[18] Hoang, S., Berglund, S. P., Hahn, N. T., Bard, A. J. & Mullins, C. B. Enhancing visible light photo-oxidation of water with TiO_2 nanowire arrays via cotreatment with H_2 and NH_3: synergistic effects between Ti^{3+} and N. *J. Am. Chem. Soc.* **134**, 3659-3662 (2012).

[19] Zhou, Y., Liu, Y., Liu, P., Zhang, W., Xing, M. & Zhang, J. A facile approach to further improve the substitution of nitrogen into reduced TiO_{2-x} with an enhanced photocatalytic activity. *Appl. Catal. B: Environmental* **170**, 66-73 (2015).

[20] Li, G.; Li, J.; Li, G.; Jiang, G. N and Ti^{3+} co-doped 3D anatase TiO_2 superstructures composed of ultrathin nanosheets with enhanced visible light photocatalytic activity. *J. Mater. Chem. A* **3**, 22073-22080 (2015).

[21] Sun, Q. et al. The formation of defect-pairs for highly efficient visible-light catalysts. *Adv. Mater.* **29**, 1605123 (2017).

[22] Hu, W. Et al. Electron-pinned defect-dipoles for high-performance colossal permittivity materials. *Nat. Mater.* **12**, 821-826 (2013).

[23] Hu, W., Lau, K., Liu, Y., Withers, R. L., Chen, H., Fu, L., Gong, B. & Hutchison, W. Colossal dielectric permittivity in (Nb+Al) codoped rutile TiO_2 ceramics: compositional gradient and local structure. *Chem. Mater.* **27**, 4934-4942 (2015).

[24] Hacene, M., Anciaux-Sedrakian, A., Rozanska, X., Klahr, D., Guignon, T. & Fleurat-Lessard, P. Accelerating VASP electronic structure calculations using graphic processing units. *J. Comput. Chem.* **33**, 2581-2589 (2012).

[25] Hutchinson, M. & Widom, M. VASP on a GPU: application to exact-exchange calculations of the stability of elemental boron. *Comput. Phys. Commun.* **183**, 1422-1426 (2012).

[26] Kresse, G. & Joubert, J. From ultrasoft pseudopotentials to the projector augmented-wave method. *Phys. Rev. B.* **59**, 1758 (1999).

[27] Blaha, P., Schwarz, K., Madsen, G. K. H., Kvasnicka, D. & Luitz, J. *WIEN2k: an augmented plane wave + local orbitals program for calculating crystal properties*, 2001, Techn. Universität, Wien, AT.

[28] Tran, F. & Blaha, P. Accurate band gaps of semiconductors and insulators with a semilocal exchange-correlation potential. *Phys. Rev. Lett.* **102**, 226401 (2009).

[29] Ambrosch-Draxi, C. & Sofo, J. O. Linear optical properties of solids within the full-potential linearized augmented planewave method. *Comput. Phys. Commun.* 175, 1-14 (2006).

[30] Sun, Q. et al. Bimetallic ions codoped nanocrystals: doping mechanism, defect formation, and associated structural transition. *J. Phys. Chem. Lett.* **8**, 3249-3255 (2017).

[31] Wang, C., Li, Q. & Wang, R.-D. Synthesis and characterization of mesoporous TiO_2 with anatase wall. *Mater. Lett.* **58**, 1424-1426 (2004).

[32] Janitabar-Darzi, S., Mahjoub, A. R. & Nilchi, A. Investigation of structural, optical and photocatalytic properties of mesoporous TiO_2 thin film synthesized by sol-gel templating technique. *Physica E: Low-dimensional Systems and Nanostructures* **42**, 176-181 (2009).

[33] Doong, R.-A., Chang, S.-M., Hunga, Y.-C. & Kao, I.-L. Preparation of highly ordered titanium dioxide porous films: characterization and photocatalytic activity. *Sep. and Purifi. Technol.* **58**,192-199 (2007).

[34] Habibin, M. H. & Mokhtari, R. Thermal properties of undoped, S-doped, Nb-doped, and S, Nb co-doped titania nanoparticles prepared by sol–gel method. *J. Therm. Anal. Calorim.* **112**, 1179-1183 (2013).

[35] Li, X., Liu, P., Mao, Y., Xing, M. & Zhang, J. Preparation of homogeneous nitrogen-doped mesoporous TiO_2 spheres with enhanced visible-light photocatalysis. *Appl. Cataly. B: Environmental* **164**, 352-360 (2015).

[36] Yin, H. Y., Wang, X. L., Wang, L., Na, Q. L. & Zhao, H. T. Self-doped TiO_2 hierarchical hollow spheres with enhanced visible-light photocatalytic activity. *J. Alloys and Compoud.* **640**, 68-74 (2015).

Figures

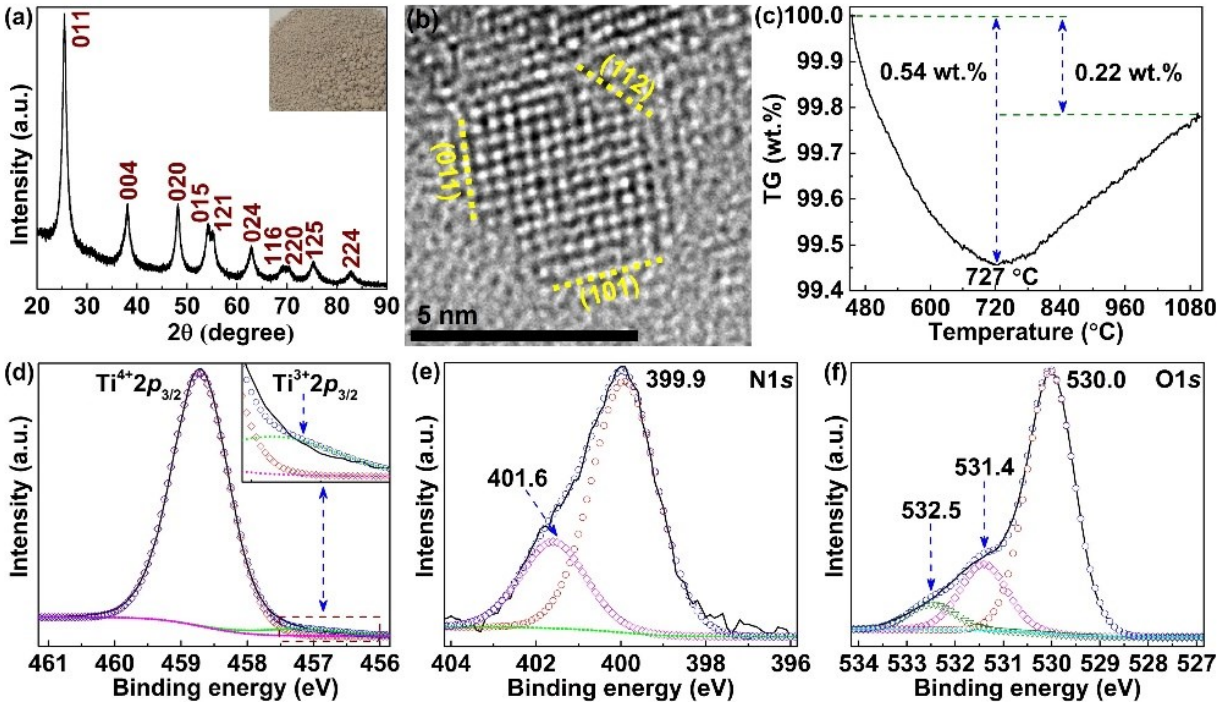

Figure 1, The XRD pattern (a), HRTEM lattice image (b), TGA curve (c) and XPS data (d-f) of the synthesized anatase ($Ti^{4+}_{0.9619}Ti^{3+}_{0.0381}$)($O^{2-}_{1.9352}N^{3-}_{0.0305}\square_{0.0343}$) nanocrystals. The inset of (a) is their optical photograph.

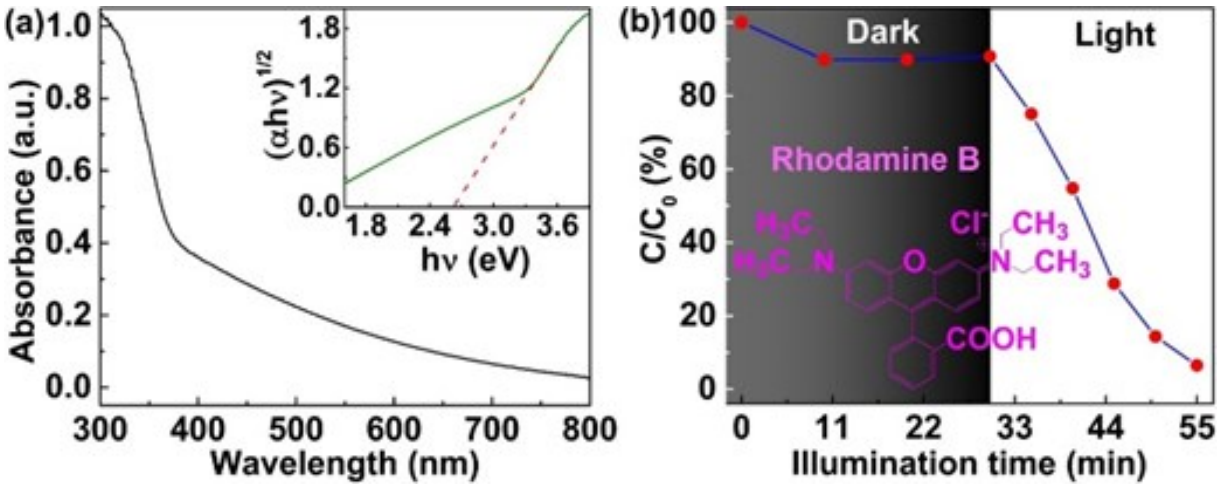

Figure 2, The UV-Vis absorption spectrum (a) and associated Tauc plot of the synthesized ($Ti^{4+}_{0.9619}Ti^{3+}_{0.0381}$)($O^{2-}_{1.9352}N^{3-}_{0.0305}\square_{0.0343}$) nanocrystals. (b) is the photocatalytic degradation of RhB under visible light irradiation ($\lambda \geq 400$ nm) using them as visible light catalysts. Here, "dark" means no light irradiation for achieving an adsorption/desorption equilibrium of RhB on nanoparticle surfaces. "C_0" is the initial RhB solution concentration while "C" indicates the remaining concentration at selected reaction time.

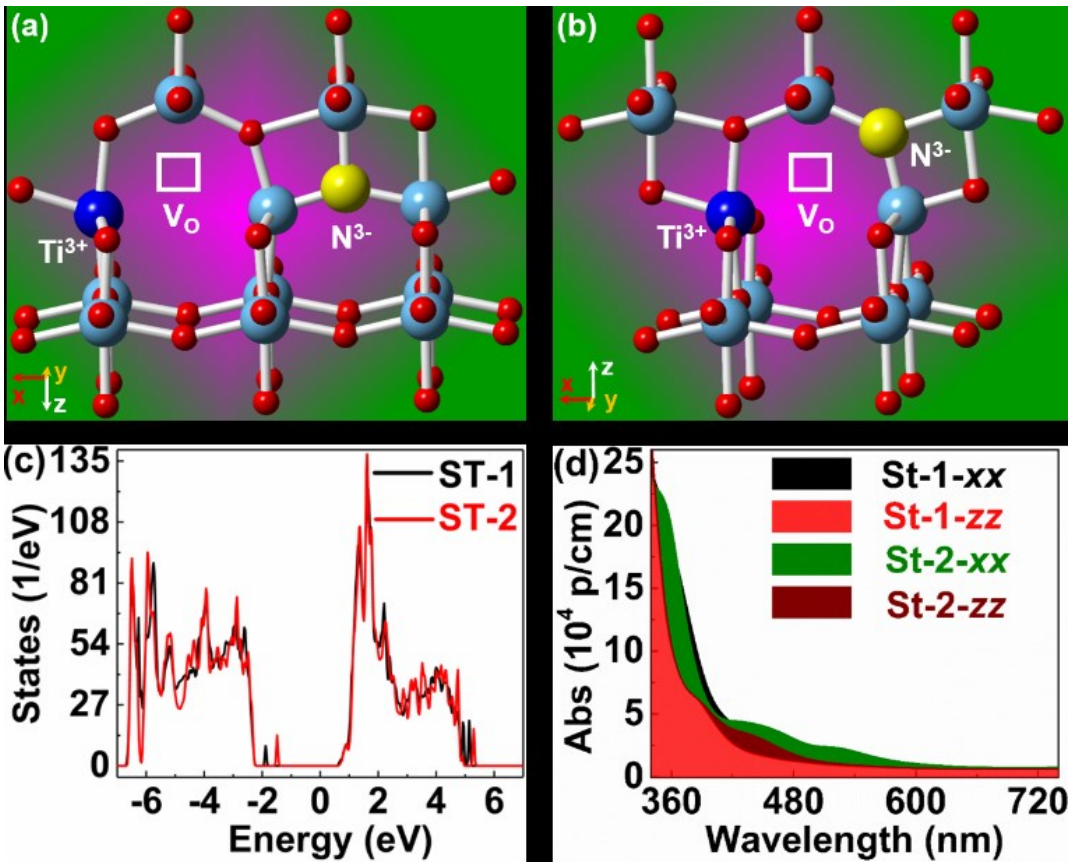

Figure 3, Ball and stick model of two local Ti^{3+}-V_O-$2Ti^{4+}$-N^{3-} clusters formed in anatase TiO_2 crystal structure with lower total energy (a is Structure 1, ST-1 and b is Structure 2, ST-2). (c) is the total density of states of the two different defect structures calculated using the mBJ potential, with E=0 corresponding to the Fermi energy. (d) is the calculated optical absorption coefficient from ST-1 and ST-2 for two components (xx, zz) of the anisotropic optical tensor, showing their light absorption into the entire region (400-700 nm) depicted by the overlaid spectra.

Table 1. The measurement conditions of photocatalytic reaction and the compared photocatalytic efficiency between our defect clusters modified samples and commercial Degussa-P25.

Photocatalysts	Measurement Conditions	VLCs concentration	RhB concentration	VLC efficiency
Our samples	Xe lamp (500 W, 400 nm cutoff)	1 g/L	20 mg/L	~94%@25min
Degussa-P25	Xe lamp	1 g/L	20 mg/L	~7%@25min

(500 W, 400 nm cutoff)

Highly Efficient Visible Light Catalysts Driven by Ti^{3+}-V_O-$2Ti^{4+}$-N^{3-} Defect Clusters

Qingbo Sun[a], Shaoyang Zhang[b], David Cortie[a,c], Terry J. Frankcombe[d], Jie Gao[e], Hua Chen[f], Ray L. Withers[a], Felipe Kremer[f], Dehong Yu[c], Frank Brink[f], Wensheng Shi[b] and Yun Liu[a*]

[a] Research School of Chemistry, [f] Centre for Advanced Microscopy, The Australian National University, Canberra, Acton, 2601, Australia.

[b] Technical Institute of Physics and Chemistry, Chinese Academy of Sciences, Beijing, 100190, China.

[c] The Australian Nuclear Science and Technology Organisation, Lucas Height, New South Wales, 2234, Australia.

[d] School of Physical, Environmental and Mathematical Sciences, The University of New South Wales, Canberra, ACT, 2601, Australia.

[e] Analysis and Testing Centre for Inorganic Materials, Shanghai Institute of Ceramics, Chinese Academy of Sciences, Shanghai, 200050, China.

Keywords: Defect Cluster, Doping, TiO_2, Visible light Catalysts, Solvothermal Reaction.

Supporting Information

SI-1, The crystallite sizes of (Ti^{3+}, N^{3-}) co-doped TiO_2 nanocrystals

The Scherrer equation (**Equation S1**) is used to calculate the average particle size of (Ti^{3+}, N^{3-}) co-doped anatase TiO_2 nanocrystals, where the Bragg angles (θ, 25.27°) and the line broadening at half the maximum intensity (β, 1.05) come from the strongest (101) diffraction peak; D is the average particle size; λ is the X-ray wavelength of CuKα

* Corresponding author: Professor Yun Liu; E-mail: yun.liu@anu.edu.au.

radiation (0.15418 nm) and K is a dimensionless shape factor (~0.9). The calculated results show that their average crystalline size is only 7.7 nm.

$$D = \frac{K\lambda}{\beta cos\theta} \qquad \text{Equation S1}$$

SI-2, A low magnification TEM image of (Ti^{3+}, N^{3-}) co-doped TiO_2 nanocrystals

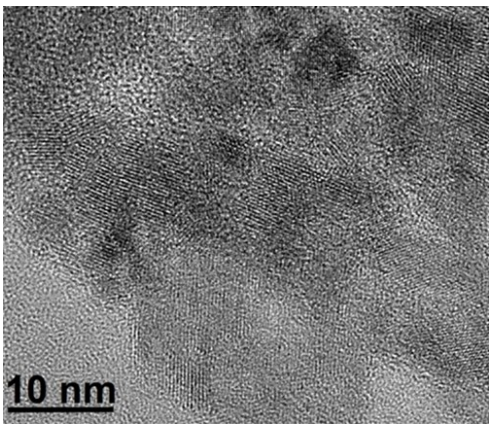

Figure S1, A low magnification TEM image of (Ti^{3+}, N^{3-}) co-doped anatase TiO_2 nanocrystals.

The lattice image of Figure S1 shows that the particle size of the prepared (Ti^{3+}, N^{3-}) co-doped TiO_2 nanocrystals is small and most of them are below 10 nm. This result is also in consistency with the calculation of the Scherrer equation.

SI-3, The specific surface area of (Ti^{3+}, N^{3-}) co-doped TiO_2 nanocrystals

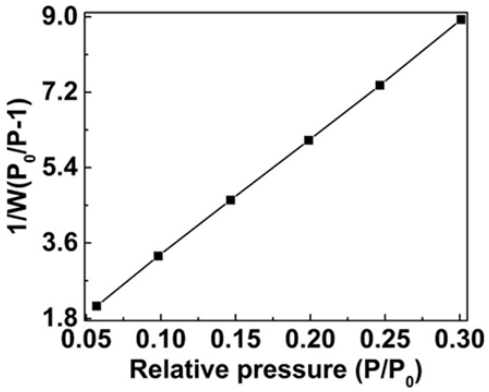

Figure S2, The curve of $1/[W(P_0/P-1)]$ versus P/P_0 for (Ti^{3+}, N^{3-}) co-doped TiO_2 nanocrystals

The specific surface area of (Ti^{3+}, N^{3-}) co-doped TiO_2 nanocrystals was measured through the Brunauer-Emmett-Teller (B.E.T.) method at liquid nitrogen temperature (~77 K). The B.E.T. surface area is calculated through **Equation S2**. In this equation, "*S*" stands for

the specific surface area of samples; "V_m" is the monolayer capacity; "L_{av}" is the Avagadro's number (6.022×10^{23}); "A_m" is the cross-sectional area (1.62×10^{-19} m^2) and "W_t" is the molecular weight of N_2 (28.01 g/mol).

$$S = \frac{(V_m \times L_{av} \times A_M)}{W_t} \qquad \text{Equation S2}$$

The V_m value in the Equation S2 is calculated through the slope (27.864) and intercept (0.5253) of the curve of Figure S2. The calculated result shows that (Ti^{3+}, N^{3-}) co-doped nanocrystals have the B.E.T. surface area of about 122.7 m^2/g.

SI-4, The TGA curve of (Ti^{3+},N^{3-}) co-doped TiO_2 nanocrystals below 450°C

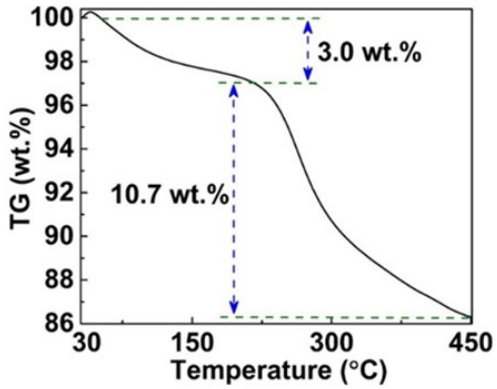

Figure S3, TGA curve of (Ti^{3+}, N^{3-}) co-doped TiO_2 nanocrystals from 30 °C to 450 °C.

Figure S3 shows the TGA curve of (Ti^{3+}, N^{3-}) co-doped anatase TiO_2 nanocrystals between 30°C and 450°C. It is found that the total weight loss in this temperature range is ~13.7 wt.%. Such a substantial loss generally comes from physically/chemically bonded chemicals on material surfaces such as physically adsorbed H_2O, chemically bonded -OH, $-CH_3$ and other organic groups. The further analysis of those chemicals on nanoparticle surfaces is shown in their FT-IR spectrum (please see SI-5).

SI-5, FT-IR spectrum of (Ti^{3+}, N^{3-}) co-doped TiO_2 nanocrystals

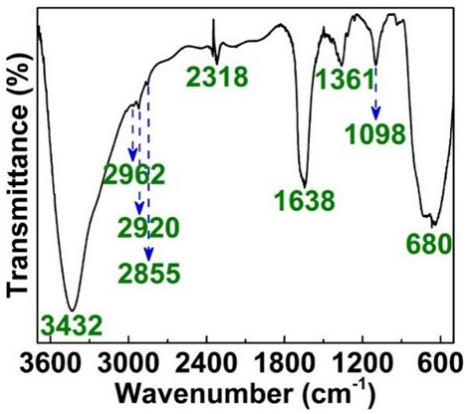

Figure S4. FT-IR spectrum of (Ti^{3+}, N^{3-}) co-doped anatase TiO_2 nanocrystals.

In order to analyse the origin of the ~13.7 wt.% weight loss below 450 °C, FT-IR spectrum of (Ti^{3+}, N^{3-}) co-doped anatase TiO_2 strongest absorption peak at about 3432 cm^{-1} comes from the stretching vibration of hydroxyl groups physically adsorbed or chemically bonded on (Ti^{3+},N^{3-}) co-doped TiO_2 surfaces including water and/or ethanol while the sharp peak at about 1638 cm^{-1} is related to their bending vibration. The absorption bands in the region of 2850-2962 cm^{-1} are assigned to different C-H stretching vibration modes such as -CH_2, -CH_3 and others. The small peak at 2318 cm^{-1} is caused by absorbed CO_2 while the peak at 1361 cm^{-1} originates in the bending vibration of C-H bonds. The stronger peak at 1098 cm^{-1} should be related to the vibration of C-C bonds. The broad peak at about 680 cm^{-1} belongs to the characterized absorption peak of Ti-O chemical bonds. The removal of these surficial groups results in their large weight loss at lower temperatures.

SI-6, The EPR spectrum of (Ti^{3+}, N^{3-}) co-doped anatase TiO_2 nanocrystals

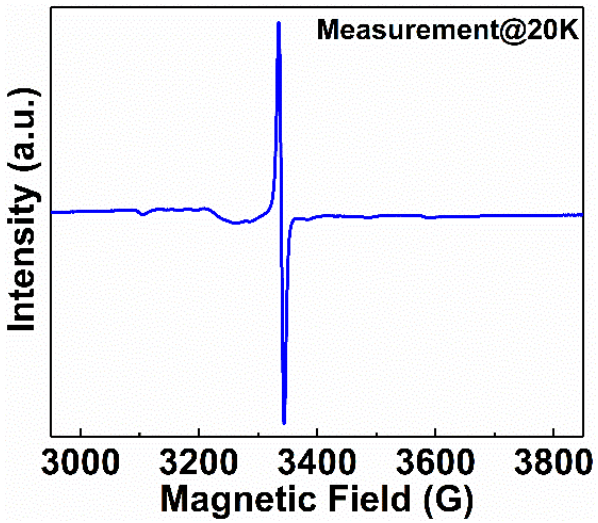

Figure S5, The EPR spectrum of (Ti^{3+}, N^{3-}) co-doped anatase TiO_2 nanocrystals collected at 20 K temperature condition.

The EPR spectrum of (Ti^{3+}, N^{3-}) co-doped anatase TiO_2 nanocrystals is shown in Figure S5. An EPR peak appears at about 3330 Gauss and represents the presence of Ti^{3+} ions in the samples. This result is consistent to that of XPS.

SI-7, The decomposition of Rhodamine B under direct light illumination and using commercial P25 as visible light catalysts.

From Figure S6, it can be found that RhB itself cannot decompose at our experimental condition even prolonging the reaction time to 60 minutes. Meanwhile, the commercial Degussa-P25 presents very low photocatalytic efficiency for RhB with the C/C0 value of up to ~93% at 25 minutes and ~60% at 60 minutes. This also demonstrates that the excellent photocatalytic property of (Ti^{3+}, N^{3-}) co-doped anatase TiO_2 nanocrystals should be attributed to the introduction of highly concentrated Ti^{3+}-V_O-$2Ti^{4+}$-N^{3-} defect clusters.

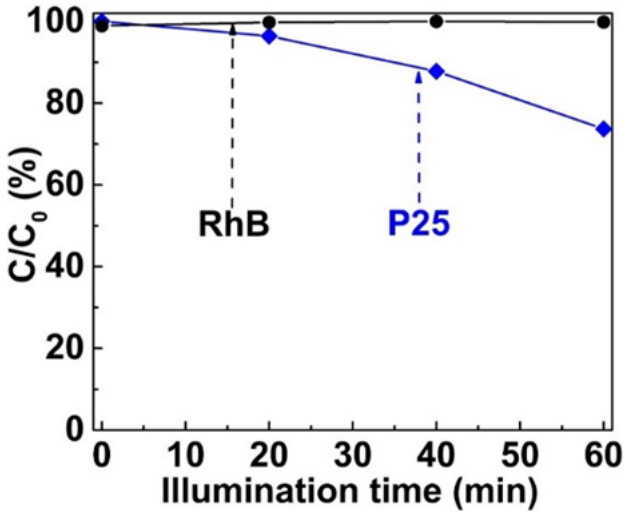

Figure S6. Photocatalytic degradation of Rhodamine B under direct light irradiation (λ≥400 nm) using the commercial Degussa-P25 as visible-light-catalysts or no catalysts.

3.5 (N^{3-}, M^{5+}) co-doping strategies for the development of TiO_2-based visible light catalysts

I wrote this review paper under the guidance of prof. Yun Liu.

Research & Reviews in Electrochemistry
ISSN: 0974-7540

Research and Reviews in Electrochemistry

Review | Vol 8 Iss 1

(N^{3-}, M^{5+}) Co-Doping Strategies for the Development of TiO_2-Based Visible Light Catalysts

Qingbo Sun, Bethany R McBride and Yun Liu*

Research School of Chemistry, The Australian National University, Canberra, Australian Capital Territory, 2601, Australia.

***Corresponding author:** Yun Liu, Research School of Chemistry, The Australian National University, Canberra, Australian Capital Territory, 2601, Australia, Tel: 61261251124; E-mail: yun.liu@anu.edu.au

Received: April 07, 2017; **Accepted:** June 22, 2017; **Published:** June 30, 2017

Abstract

(N^{3-}, M^{5+}) co-doping is an efficient strategy to activate the visible light catalytic behavior of TiO_2 for broad use in wastewater purification, air cleaning, hydrogen generation, and sterilization. Here, we briefly review the recent progress of (N^{3-}, M^{5+}) co-doping strategies for the development of TiO_2-based visible light catalysts. The designed synthesis methods, the characterized material properties, the measured photocatalytic activity and the introduced local defect structures are summarized. It is expected that this mini review can build up a general framework for future/current research into (N^{3-}, M^{5+}) co-doped TiO_2 materials and provide a direction for the further development of TiO_2-based visible light catalysts.

Keywords: Photocatalysis; Solar energy; Doping

Introduction

The development of TiO_2-based visible light catalysts (VLCs) is significant to enhance the utilization efficiency of clean/renewable solar energy, and to remedy the current state of environmental pollution by directly harnessing sunlight to drive a range of chemical reactions. These chemical reactions include generating hydrogen from water, removing organic/toxic compounds in wastewater or air, automatically decomposing plastic rubbish, and even sterilization. In principle, the light energy absorbed by TiO_2-based VLC materials is used to generate electrons and holes. These photo-excited carriers subsequently migrate to the surfaces of VLC materials and chemically react with various targets. This simple photocatalytic process depends on three critical steps: (1) the light absorption ability of TiO_2-based VLCs. It determines how much photo-energy can be efficiently utilized by VLCs; (2) the efficient separation of electron-hole pairs. This dictates the numbers of active reductants/oxidants available for final chemical reactions; and (3) the migration distance and the lifetime of photo-excited carriers. Longer distances and shorter lifetimes are obviously undesirable for achieving excellent photocatalytic efficiency.

To meet the above criteria, N^{3-} and M^{5+} (M=Nb, V, Ta) co-doping strategies were designed to develop TiO_2-based VLCs. That is, N^{3-} and M^{5+} ions are simultaneously incorporated into TiO_2 crystal structures by substituting a proportion of the Ti^{4+} and O^{2-} host ions. The atomic orbitals of these extrinsic co-dopant ions will hybridize with that of Ti^{4+}, O^{2-} or each other to extend the light absorption of TiO_2 towards the visible light regime, to reduce the recombination of electron-hole pairs, and finally to enhance VLC efficiencies.

The cation-anion co-doping, in this case N^{3-} and M^{5+} co-doping, leads to the appearance of the third generation of TiO_2-based

Citation: Sun Q, McBride BR, Liu Y. (N^{3-}, M^{5+}) Co-Doping Strategies for the Development of TiO_2-Based Visible Light Catalysts. Res Rev Electrochem. 2017;8(1):106.

photocatalysts. Prior to this, the first generation was designed based on intrinsic TiO_2. Through tuning the exposed crystal plane, particle size distribution, crystal structure, phase compositions, and surface chemistry, the photocatalytic properties of intrinsic TiO_2 could be controlled technologically. However, since this generation of TiO_2 only absorbs ultraviolet light, most of the solar energy spectrum is wasted and their applications are restricted. To increase the light absorption range, the second generation of TiO_2-based VLCs was subsequently developed based on cationic or anionic mono-doping routes. Although most of the elements in the atomic periodic table have been tried, the photocatalytic effects of resultant products are still not good. On one hand, mono-doping cations is difficult to enhance visible light absorption and thus often results in unimproved or even worse visible light catalytic properties. On the other hand, mono-doping anions suffers a technical difficulty in their high doping levels. Furthermore, the generation of "trapping or recombination centers" would also worsen photocatalytic efficiency since they "kill" photo-excited electron and hole carriers. FIG. 1 summarizes the development process, advantages and disadvantages of different TiO_2-based photocatalysts.

This work briefly reviews the recent progress of (N^{3-}, M^{5+}) co-doping strategies for the development of TiO_2-based VLCs. We first explain why N^{3-} and M^{5+} are chosen as co-dopants for TiO_2. Then, we summarize the synthesis methods, material properties, VLC performances and local defect structures of prepared (N^{3-}, M^{5+}) co-doped TiO_2 materials according to the type of used M^{5+} ions. Finally, we point out the existing concerns from current investigations into (N^{3-}, M^{5+}) co-doped TiO_2 materials and prospects for the future development of TiO_2-based VLCs.

The Selection of M^{5+} Cations for Co-Doping with N^{3-} Anions

In (N^{3-}, M^{5+}) co-doped TiO_2 materials, N^{3-} anions are used to substitute O^{2-} ions while M^{5+} cations are used to replace Ti^{4+} ions. The selected M^{5+} ions mainly include Nb^{5+}, Ta^{5+} and V^{5+}. In the atomic periodic table, niobium (Nb) is the 41st element with an electronegativity of 1.6 Pauling units and has the electronic configuration of $1s^22s^22p^63s^23p^63d^{10}4s^24p^64d^45s^1$. Nb ions normally have three chemical valences depending on the number(s) of electrons in 4d and 5s orbitals, i.e., Nb^{5+} (the ionic radius, r_{ion}=0.078 nm in six-coordinated octahedral), Nb^{4+} (r_{ion}=0.082 nm) and Nb^{3+} (r_{ion}=0.086 nm) [1].Tantalum (Ta) is the 73rd element with an electronegativity of 1.5 Pauling units and has the electronic configuration of $1s^22s^22p^63s^23p^63d^{10}4s^24p^64d^{10}4f^{14}5s^25p^65d^36s^2$. Ta^{5+}, Ta^{4+} and Ta^{3+} are their three stable ions at normal conditions. The ionic radii of Ta ions are the same as that of Nb ions (i.e., r_{ion} of Ta^{5+}=0.078; Ta^{4+}=0.082 nm; Ta^{3+}=0.086 nm). Vanadium (V) is the 43rd element with an electronegativity of 1.63 Pauling units and has the electronic configuration of $1s^22s^22p^63s^23p^63d^34s^2$. The ionic radii of V ions are smaller than that of Ta or Nb ions, and are 0.068 (V^{5+}); 0.072 (V^{4+}); and 0.078 nm (V^{3+}), respectively. Since Ta^{5+} and Nb^{5+} ions have almost the similar ionic radius as Ti^{4+} (r_{ion}=0.0745 nm) and their elements show the similar electronegativity to Ti (1.54), they are normally co-doped together with N^{3-} ions into host TiO_2 without generating a large distortion in the local/average crystal structure. The smaller V^{5+} ions are also sometimes

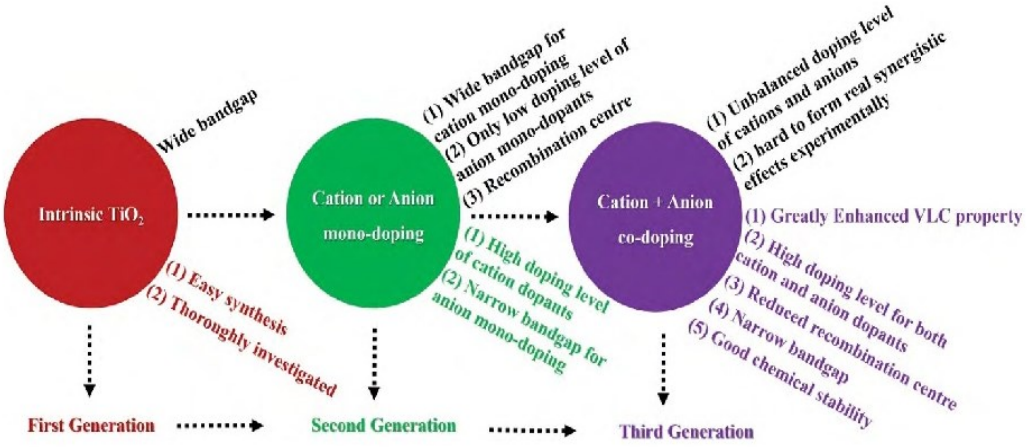

FIG. 1. **The development process, advantages (bottom) and disadvantages (top) of different TiO_2-based photocatalysts.**

chosen as co-dopants due to their easy substitution of Ti^{4+} ions. It is more important that M^{5+} dopant ions lose one additional electron in contrast to the Ti^{4+} host ions. This electron is well compensated by the co-doping of N^{3-} anions. The molar ratio of M^{5+} and N^{3-} co-dopants is thus expected to be 1:1 for the charge balance of the whole co-doped system. Any deviation of the stoichiometric ratio will generate extra Ti^{3+} ions or additional oxygen vacancies. In these two scenarios, (N^{3-}, M^{5+}) co-doping is actually accompanied by N^{3-} or M^{5+} mono-doping.

Two TiO_2 crystal structures, anatase with space group symmetry *I4 /amd* and rutile with space group symmetry *P4 /mnm*, are normally chosen as the host matrices since their syntheses are easier in comparison with other polymorphs. The coupling of N^{3-} and M^{5+} ions in TiO_2 host materials are considered to play three important roles in the enhancement of photocatalytic effects: [2] (1) activating the absorption of lower photon energies; (2) mutually compensating for the additional charges or defects generated by the introduction of dopants; and (3) facilitating a larger total dopant concentration (especially for N^{3-} anions) when N^{3-} and M^{5+} ions are bound together.

Synthesis, Characterization, Photocatalytic Properties and Related Theoretical Calculations of (N^{3-}, Nb^{5+}) Co-Doped TiO_2

Various experimental routes have been tried to date to synthesize (N^{3-}, Nb^{5+}) co-doped TiO_2 materials. TABLE 1 lists the synthesis processes, characterized properties and VLC effects for (N^{3-}, Nb^{5+}) co-doped TiO_2 [3-10,12,13]. The sources of used N are categorized into three types: (1) the colorless liquid HNO_3 (nitric acid), $C_4H_{11}N$ (*n*-Butylamine), NH_4OH (ammonia solution); (2) solid $C_6H_{12}N_4$ (hexamethylenetetramine), CH_4N_2O (urea) or $(NH_4)[NbO(C_2O_4)_2(H_2O)]\cdot nH_2O$ (ammonium niobium oxalate); and (3) NH_3 (ammonia) gas. Meanwhile, the sources of Nb are mainly focused on $NbCl_5$ (niobium pentachloride), $Ti_{1-x}Nb_x$ alloys (titanium-niobium alloys), $C_{10}H_{15}O_5Nb$ (niobium ethoxide) and $(NH_4)[(NbOF_4)(NbF_7)_2$ (ammonium uoroniobate salt). As for the Ti sources, $TiCl_4$ (titanium tetrachloride), Ti metal, $Ti_{1-x}Nb_x$ alloys, $C_{16}H_{36}O_4Ti$ (titanium *n*-Butoxide), $C_{12}H_{28}O_4Ti$ (titanium tetraisopropoxide) are normally used.

Different synthesis methods have been reported for the preparation of (N^{3-}, Nb^{5+}) co-doped TiO_2 materials depending on the selection of raw materials containing N, Nb and Ti elements. A simple approach has been recently demonstrated by Sun et al. [3]. They designed a novel solvothermal reaction route to directly synthesize (N^{3-}, Nb^{5+}) co-doped anatase TiO_2 nanocrystals without any post-sintering treatment by using concentrated HNO_3, $NbCl_5$, $TiCl_4$ and ethanol. Through this reaction route, it is easier to control the doping ratio of N^{3-}/Nb^{5+} and efficiently increase the doping concentration of difficult-dopant N^{3-} ions. This chemical reaction at the atomic level is also one of the most promising ways to guarantee the homogeneous distribution of co-dopants in TiO_2 crystal structures. Experimental and theoretical investigations confirmed that N^{3-} and Nb^{5+} co-dopants should locally form defect-pairs. FIG. 2 shows the TEM image of their synthesized (5.3 at% N^{3-}, 5.6 at% Nb^{5+}) co-doped anatase TiO_2 nanocrystals, the resultant local defect-pair motif, and the decomposition curve of Rhodamine B under only visible light illumination using the defect-pairs modified TiO_2-based VLCs. The formation of local N^{3-}- Nb^{5+} defect-pairs is critical to narrow the band gap to 2.2 eV from ~ 3.1 eV and to significantly enhance VLC efficiency (20 mg/L Rhodamine B solution is almost completely decomposed by loading 1 g/L defect-pair modified TiO_2-based VLCs under visible light illumination).

In addition, a one-step microwave-assisted hydrothermal method was also designed to simultaneously introduce N^{3-} and Nb^{5+} co-dopants into anatase TiO_2 nanoparticles [4,5]. Their bandgaps, however, are too broad (3.1 and 2.8 eV, respectively) for practical applications as VLCs. Another normal synthetic procedure is to firstly prepare Nb mono-doped TiO_2 by sol-gel or anodization treatment, and then to incorporate N dopants through high-temperature nitridation in NH_3 gas [6-10]. The high-temperature nitridation process depends on the diffusion of N ions, leading to only surface co-doping [10] or a gradient distribution of chemical compositions [11]. Moreover, an excess of Nb^{5+} dopants over N^{3-} would introduce a large number of Ti^{3+} ions to balance the charges of the whole material. In fact, these additional dopant ions and associated defects may play a detrimental role on VLC properties when compared with uniform (N^{3-}, Nb^{5+}) co-doping. Additionally, Chadwick et al. [13] designed an aerosol assisted chemical vapor deposition method to directly prepare (N^{3-}, M^{5+}) co-doped TiO_2 films by using *n*-butylamine and niobium ethoxide. The co-doping level of N^{3-} ions are proven to be too low (only 0.09 at. %) to strengthen the light absorption behaviors and visible light catalytic properties.

TABLE 1. **The synthesis processes, characterized properties and VLC effects for (N^{3-}, Nb^{5+}) co-doped TiO_2 (NP: Nanoparticle; NTA: Nanotube Array; RhB: Rhodamine B; MB: Methylene Blue; 4-CP: 4-Chlorophenol).**

Synthesis				Characterization					VLC properties				
N source	Nb source	Ti source	Method & Condition	N (at.%)	Nb (at.%)	Phase	Bandgap (eV)	Shape	Light source	Dye (mg/L)	VLCs (g/L)	C/C_0 (%)	Ref.
HNO_3	$NbCl_5$	$TiCl_4$	Solvothermal (200 °C, 12 h)	5.3 (XPS, TGA, N-O determinator)	5.6 (XPS)	Anatase	2.2	NP (<10 nm)	Xe lamp (500W, > 400nm, 10 cm)	RhB (20)	1	0@20 min	3
NH_4OH/ CH_4N_2O	$NbCl_5$	$Ti(SO_4)_2$	Microwave-assisted hydrothermal	15 (nominal)	10 (XPS)	Anatase	3.1	NP (~9 nm)	halogen lamp (500W, > 400nm)	H_2O	0.4	100 umol/h	4
$C_6H_{12}N_4$	$NbCl_5$	$TiCl_4$	Microwave-assisted hydrothermal (190 °C, 0.5 h)	-	2 (EDX)	Anatase	2.8	NP	LED lamps	NO (2ppm)	-	31%	5
NH_3	$NbCl_5$	$C_{16}H_{36}O_4Ti$	Sol-gel & Post-sintering (500 °C, 5 h, NH_3)	-	1-33.3 (nominal)	Anatase	2.0	NP (20 nm)	Xe lamp (150W, AM 1.5G filter)	MB (40)	-	7@120 min	6,7
NH_3	$NbCl_5$	$C_{16}H_{36}O_4Ti$	Sol-gel & Post-sintering (500 °C, 5 h, NH_3)	0.2 (XPS)	25 (XPS)	Anatase	2.2	NP (20 nm)	xenon lamp (150W, AM 1.5G filter)	H_2O	1	7umol/h	8
NH_3	$Ti_{1-x}Nb_x$	Ti1-xNbx	Anodization & Post-sintering (450 °C, 0.5 h,NH_3)	8.2 (XPS)	10 (nominal)	Anatase	2.8	NTA	halogen lamp (3.0mW/cm^2, > 400nm)	MB (2)	-	12@120min	9
NH_3	$(NH_4)[(NbOF_4)(NbF_7)_2]$	Ti foil	Anodization & Post-sintering (550 °C, 2 h, NH_3)	6.9 (XPS)	4 (bulk)	Anatase	-	NTA	Oriel EmArc (200W)	-	-	-	10
NH_4OH & HNO_3	$NbCl_5$	$C_{12}H_{28}O_4Ti$	Sol-gel & Post-sintering (400 °C, 3 h, air)	-	0.5	Anatase	2.98	NP	xenon lamp (300W, > 420nm)	4-CP	1	0@120 min	12
$C_4H_{11}N$	$C_{10}H_{15}O_5Nb$	$C_{12}H_{28}O_4Ti$	Aerosol assisted chemical vapor deposition	0.06-0.09 (XPS)	2-10 (XPS)	Anatase	2.4-3.5	film	-	-	-	-	13

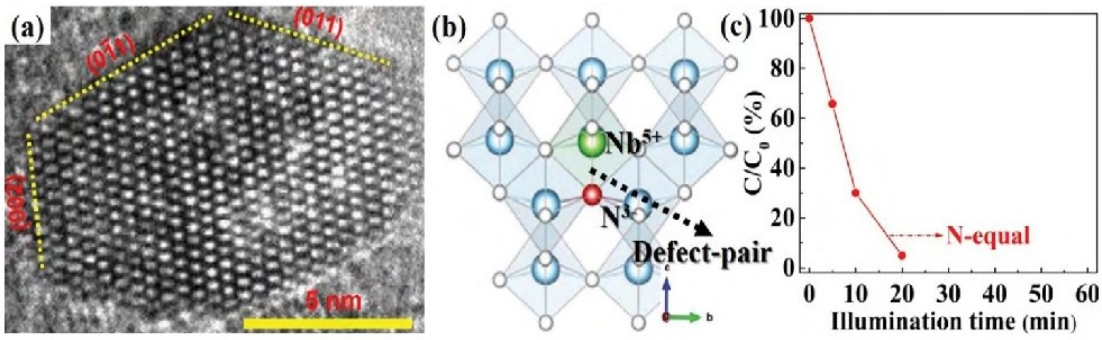

FIG. 2. **(a) The TEM image of (5.3 at % N^{3-}, 5.6 at % Nb^{5+}) co-doped anatase TiO_2 nanocrystals, (b) the resultant local defect-pair motif and (c) the decomposition curve of Rhodamine B under only visible light illumination using these defect-pairs modified VLCs. Copyright Wiley-VCH Verlag GmbH & Co. KGaA. Reproduced with permission from reference 3.**

It can be further seen from TABLE 1 that nearly all of the synthesized (N^{3-}, Nb^{5+}) co-doped TiO_2 materials have an anatase crystal structure. The reported morphologies refer to 0-D nanoparticles with different average particle sizes, 1-D nanotubes and 2-D films. The doping concentrations of N^{3-} and Nb^{5+} co-dopants are usually analyzed by XPS (X-ray photoelectron spectroscopy). Confusion has arisen on the correct XPS core levels of interstitial, substitutional or contaminated N in (N^{3-}, Nb^{5+}) co-doped TiO_2 materials. Moreover, XPS can only provide chemical information on sample surfaces. It is thus hard to quantitatively describe the doping levels of N^{3-} ions and further distinguish the "surface co-doping" or "bulk co-doping" by just relying on the XPS analysis. The combination of XPS with TGA-DSC (thermogravimetry and differential scanning calorimetry analysis) and N-O determinator measurements should give a more reasonable and more acceptable conclusion on the real N^{3-} doping concentration [3].

The decomposition of dyes like Rhodamine B (RhB), methylene blue (MB) and 4-chlorophenol (4-CP) under visible light was measured to present the VLC efficiency of (N^{3-}, Nb^{5+}) co-doped TiO_2. Water splitting experiments were also conducted by some researchers. Due to the different experimental setup and operations such as the light sources, the dye concentrations and types, or the VLCs loading amounts, it is difficult to compare the VLC efficiency of (N^{3-}, Nb^{5+}) co-doped TiO_2 achieved by different researchers. However, one commonly accepted fact is that (N^{3-}, Nb^{5+}) co-doping is more efficient in the enhancement of VLC properties than N^{3-} or Nb^{5+} mono-doping.

Synthesis, Characterization, Photocatalytic Properties and Related Theoretical Calculations of (N^{3-}, Ta^{5+}) Co-Doped TiO_2

In the synthesis of (N^{3-}, Ta^{5+}) co-doped TiO_2 materials, the synthesis methods, experimental processes and utilized Ti/N sources are very similar to that of (N^{3-}, Nb^{5+}) co-doped TiO_2, just with a replacement of the Nb sources with Ta sources. The selected Ta sources include $TaCl_5$ (tantalum pentachloride), Ta metal, $(Ta_2O_5)_{0.01}(TiO_2)_{0.99}$ ceramic pellets, $C_{15}H_{35}O_5Ta$ (tantalum isopropoxide) and $C_{10}H_{25}O_5Ta$ (tantalum ethoxide). TABLE 2 lists the synthesis processes, characterized properties and VLC effects for (N^{3-}, Ta^{5+}) co-doped TiO_2 [14-18]. It can be found that (N^{3-}, Ta^{5+}) co-doped rutile TiO_2 was synthesized by a combination of solvothermal and post-sintering methods [17,18]. During the solvothermal reaction process, Ta mono-doped rutile TiO_2 nanowires or nanorods were first prepared. The subsequent high-temperature nitridation treatment was used to introduce N^{3-} ions into the as-prepared Ta mono-doped rutile nanocrystals to form (N^{3-}, Ta^{5+}) co-doped rutile TiO_2. Comparing with the N mono-doped rutile TiO_2, the co-doping of N^{3-} and Ta^{5+} ions can prohibit the formation of amorphous layers on the nanowire surfaces and thus enhance the incident photon to current conversion efficiency [17]. However, the chemical composition, especially the doping levels of N^{3-} ions, is not discussed at all. It is thus difficult to compare their results with that of co-doped anatase TiO_2 nanomaterials.

The measured bandgaps of (N^{3-}, Ta^{5+}) co-doped TiO_2 materials range from 2.6 to 3.1 eV. It seems that the narrowed band gap can only be achieved at a higher N^{3-} and Ta^{5+} co-doping concentration [14-16]. This conclusion is consistent with the claims of Sun et al.[3] They point out that the higher and nearly equal doping concentrations of cation and anion co-dopants are key to tuning the light absorption behavior and are critical for significantly enhancing VLC properties. Using these synthesized (N^{3-}, Ta^{5+}) co-doped TiO_2, the degradation of MB and oleic acid was characterized under visible light illumination. For example, Zhao et al. [14] investigated the visible light degradation of MB (5 mg/L) under 1 g/L VLCs solution. They found that the C/C_0 (C is the dye concentration at different illumination time and C_0 represents the initial dye concentration) was 31.6% at the reaction period of 240 min. At the same time, Le et al. [15] also investigated the visible light degradation of MB with the same concentration (5 mg/L). The C/C_0 was 7% at the reaction time of 180 min by increasing the loading amount of VLCs to 3 g/L. Due to their different light sources and different loading amounts of VLCs, it is not easy to judge whose VLCs are better for the visible light catalytic decomposition of MB.

Theoretical calculations were performed on (N^{3-}, Ta^{5+}) co-doped TiO_2 to disclose where N^{3-} and Ta^{5+} ions are located in the TiO_2 crystal structure, how the synergistic effects between N^{3-} and Ta^{5+} co-dopants tune the bandgap and affect photocatalytic properties [14,16,19]. FIG. 3 shows a 108-atom super cell containing one substituted N and one replaced Ta. Among various co-doped configurations, N and Ta co-dopants prefer to directly bind together in one octahedron. The extension in the N-Ta distances will lead to higher total formation energy. Actually, N^{3-} and Ta^{5+} co-dopants locally form similar defect-pairs to the N^{3-} and Nb^{5+} co-doping system [3]. The hybridization of N2*p* and Ta5*d* states in N-Ta defect-pairs reduces recombination centers caused by impurity levels (FIG. 3b and 3c), narrows the bandgap, increases carrier mobility, and finally enhances the VLC properties. The calculated band

TABLE 2. **The synthesis processes, characterized properties and VLC effects for (N^{3-}, Ta^{5+}) co-doped TiO_2 (NP: Nanoparticle; NW: Nanowire; NR: Nanorod; MB: Methylene Blue).**

Synthesis				Characterization						VLC properties			
N source	Ta source	Ti source	Method & Condition	N (at.%)	Ta (at.%)	Phase	Bandgap (eV)	Shape	Light source	Dye (mg/L)	VLCs (g/L)	C/C_0 (%)	Ref.
CH_4N_2O	$TaCl_5$	$C_{16}H_{36}O_4Ti$	Sol-gel & Post-sintering (500 °C, 1 h, air)	13.4 (XPS)	12.8 (XPS)	Anatase	2.68	NP	Xe lamp (500W, > 420nm)	MB (5)	1	32@240min	14
NH_4OH	Ta	$C_{12}H_{28}O_4Ti$	Hydrothermal & Post-sintering (300 °C, 1 h, air)	1.7 (XPS)	0.29 (XPS)	Anatase	2.85	NP (20 nm)	Hg-Xe lamp (500W, > 420nm)	MB (5)	3	~7@180 min	15
N_2	$(Ta_2O_5)_{0.01}(TiO_2)_{0.99}$	Ti & $(Ta_2O_5)_{0.01}(TiO_2)_{0.99}$	Magnetron sputtering (400 °C)	0.5-0.6 (XPS)	2.3-1.3 (XPS)	Anatase	3.07-3.16	Film	Xe lamp (420-500nm)	Oleic acid	-	11@120 min	16
NH_3	$C_{15}H_{35}O_5Ta$	$TiCl_4$	Solvothermal & Post-sintering (500 °C, 2 h, NH_3)	-	0.29 (XPS)	Rutile	-	NW	Visible light (>420 nm)	-	-	-	17
NH_3	$C_{10}H_{25}O_5Ta$	$C_{12}H_{28}O_4Ti$	Microwave-assisted solvothermal & Post-sintering (350 °C, 1 h, NH_3)	-	-	Rutile	~2.6	NR	Xe lamp (500W, > 420nm)	H_2O	0.5	0.7 umol h^{-1}	18

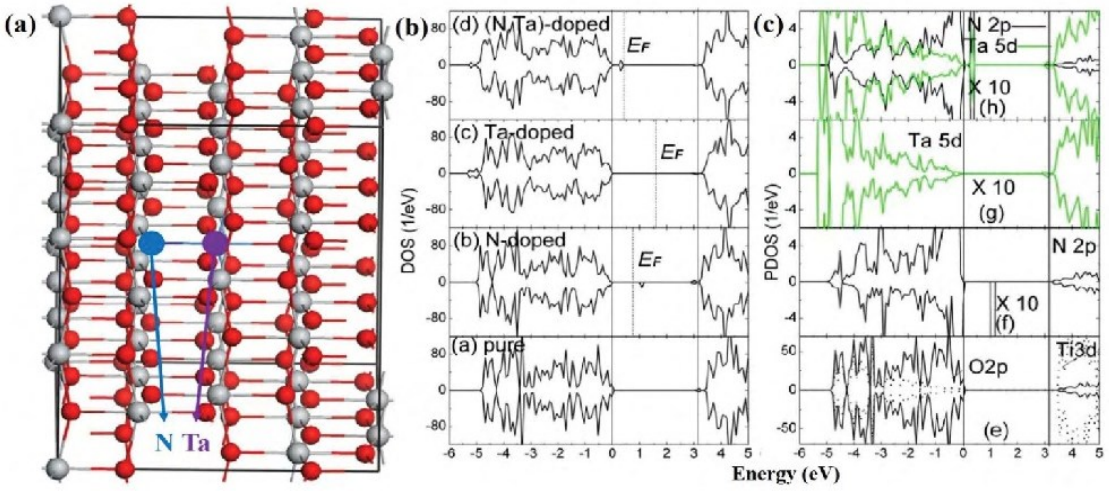

FIG. 3. **(a) A 108-atom supercell containing substituted N and Ta co-dopants, (b) the calculated total DOS and (c) PDOS of un-doped, Ta mono-doped, N mono-doped and (N, Ta) co-doped anatase TiO_2 Reprinted with permission from reference 19.**

gap of 2.7 eV is also consistent with the experimental results [14,18]. For (N^{3-}, Ta^{5+}) co-doped rutile TiO_2, there are no associated theoretical calculations to date.

Synthesis, Characterization, Photocatalytic Properties and Related Theoretical Calculations of (N^{3-}, V^{5+}) Co-Doped TiO_2

The synthesis methods used for the preparation of (N^{3-}, V^{5+}) co-doped TiO_2 materials are the same as that of (N^{3-}, Nb^{5+}) and (N^{3-}, V^{5+}) co-doped TiO_2. For example, the high-temperature nitradation in NH_3 is also used to introduce N^{3-} ions into as-prepared V mono-doped TiO_2. TABLE 3 lists the synthesis processes, characterized properties and VLC effects for (N^{3-}, V^{5+}) co-doped TiO_2 [20-25]. NH_4VO_3 is predominantly used as a V source. In contrast to the synthesis of (N^{3-}, Nb^{5+}) and (N^{3-}, V^{5+}) co-doped TiO_2, the hydrothermal route is frequently used to synthesize (N^{3-}, V^{5+}) co-doped TiO_2 [21-25]. It involves the incorporation of N^{3-} or V^{5+} co-dopant ions into the as-prepared V/N mono-doped TiO_2 precursor in a hydrothermal reaction autoclave. This wet chemical reaction

TABLE 3. **The synthesis processes, characterized properties and VLC effects for (N^{3-}, V^{5+}) co-doped TiO_2 (NP: Nanoparticle; NTA: Nanotube Array; RhB: Rhodamine B; MB: Methylene Blue; MO: Methylene Orange; PCP-Na: Sodium Pentachlorophenate; CAP: Chloramphenicol).**

Synthesis					Characterization					VLC properties			
N source	V source	Ti source	Method and Condition	N (at.%)	V (at.%)	Phase	Bandgap (eV)	Shape	Light source	Dye (mg/L)	VLCs (g/L)	C/C_0 (%)	Ref.
$C_6H_{15}N$	NH_4VO_3	$C_{16}H_{36}O_4Ti$	Sol-gel & Post-sintering (450 °C, 2 h, air)	4 (nominal)	2 (nominal)	Anatase	2.3	NP (7nm)	Xe lamp (150W, 15cm)	RhB (95.8)	0.29	0@60min	20
$C_6H_{15}N$	NH_4VO_3	$Ti(SO_4)_2$	Two-step hydrothermal (180 °C, 22h)	3.12 (XPS)	1.0 (ICP) & 0.5 (XPS)	Anatase	2.5	NP (13nm)	Xe lamp (400W, > 400nm)	PCP-Na (20)	0.4	~20@120 min	21
$C_6H_{15}N$	V^{4+}	$C_{16}H_{36}O_4Ti$	Two-step hydrothermal (180 °C, 22h)	-	-	Anatase	2.8	NP (5nm)	Xe lamp (400W, > 400nm, 25cm)	MB (1.6)	-	80@275 min	22
NH_4VO/NH_3OH	NH_4VO_3	TiO_2	Hydrothermal (180 °C, 12 h)	2.97 (XPS)	20 (nominal)	Anatase	-	NP (11nm)	Xe lamp (300W, > 420nm)	MO (3.3)	-	54.3@300 min	23
NH_4VO_3	NH_4VO_3	N-TiO_2	Hydrothermal (180 °C, 5 h)	3.4 (XPS)	4.2 (XPS)	Anatase	2.3	NTA	Hg lamp (300W, > 420nm)	CO_2	-	64.5 ppm h^{-1} cm^{-2}	24
$C_6H_{15}N$	NH_4VO_3	$C_{16}H_{36}O_4Ti$	Sol-gel & Hydrothermal (180 °C, 20 h)	0.62 (XPS)	2 (nominal)	Anatase	2.5	NP	Halide lamp (400W, > 420nm	CAP (25)	1	325x10^{-4} min^{-1}	25

route avoids the traditional high-temperature nitridation treatment and reduces the agglomeration of nanoparticles. However, it is debatable whether the dopants can be efficiently diffused into TiO_2 crystal structures at such mild reaction conditions and whether the "surface co-doping" dominates the photocatalytic properties.

Most of the measured bandgaps are around 2.3 and 2.5 eV for (N^{3-}, V^{5+}) co-doped TiO_2. This means that N^{3-} and V^{5+} co-doping can efficiently lower the bandgap and extend the light absorption to visible light regime. In almost all (N^{3-}, V^{5+}) co-doped samples prepared using NH_4VO_3 as raw materials, V^{5+} and V^{4+} ions are found to co-exist. If NH_4VO_3 is replaced by V^{4+}-containing raw material, V^{4+} and V^{3+} will co-exist in the samples. The reasons for the easy reduction of V ions remain unclear to date. The VLC properties of (N^{3-}, V^{5+}) co-doped TiO_2 were characterized through decomposing MB, MO (methylene orange), RhB and 4-chlorophenol; or reducing CO_2 into CH_4. In addition, Eswar et al. [25] used their synthesized (N^{3-}, V^{5+}) co-doped TiO_2 to treat antibiotics/bacteria and found that (N^{3-}, V^{5+}) co-doping would strengthen VLC properties comparing with N^{3-} or V^{5+} mono-doping. The key roles of (N^{3-}, V^{5+}) co-doping on the enhancement of VLC properties are also emphasized by other related researchers.

Theoretical calculations on (N^{3-}, V^{5+}) co-doped TiO_2 demonstrate that (N^{3-}, V^{5+}) co-doping can efficiently enhance VLC properties. FIG. 4 presents the co-doping positions of N and V in anatase TiO_2 and the calculated total DOS (density of states). Here, N^{3-} and V^{5+} chemically bind together to form defect-pairs, again. The formation of defect-pairs narrows the band gap by about 0.45 eV through providing an acceptor level of about 0.33 eV above the valence band and a donor level of about 0.12 eV below the conduction band

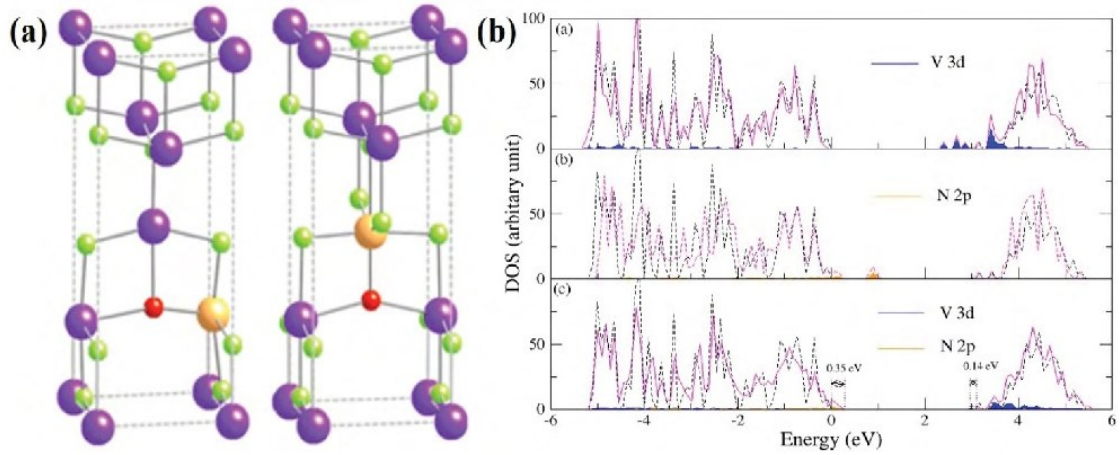

FIG. 4. **(a) The schematic illustration of (N, V) defect-pair configurations in anatase TiO_2 and (b) the calculated total DOS. The orange and red balls represent the co-doped Ta and N, respectively. Reprinted with permission from reference 26.**

[26]. Furthermore, the N-V defect-pairs have a large binding energy of about 0.77 eV, making them rather stable against separation. However, it is a technological challenge to experimentally control the chemical valences of V^{5+} dopants.

Conclusions and Prospects

In (N^{3-}, M^{5+}) co-doped TiO_2 materials, the introduced N^{3-} and M^{5+} ions would chemically bind together to form local defect-pairs. These defect-pairs are critical to narrow the bandgap of host TiO_2, reduce the "trapping or recombination centers" of photo-generated carriers, increase the doping levels of difficult-dopant N^{3-} ions, and thus significantly enhance visible light catalytic properties. Since Nb^{5+} and Ta^{5+} ions are stable in contrast to V^{5+}, it is better to select them as the co-dopants of N^{3-} ions. Given the difficulty in comparing and analyzing the photocatalytic effects reported by different research groups,

(1) A standard photocatalytic reaction setup and conditions should be developed and followed. It would include the used light source, the light illumination intensity, a fixed dye type and concentration, identical loading amounts of the catalysts, and identical reaction times;

(2) At the very least, commercial Degussa P25 should be used as a reference and all experimental results should be quantitatively compared with it;

(3) The chemical compositions of the synthesized samples should be carefully analyzed to easily unveil the intrinsic origin of observed photocatalytic activities.

Based on local defect structure design, it is expected that co-doping TiO_2 with (N^{3-}, M^{5+}) will significantly enhance their VLC properties. The development of defect-pair modified TiO_2-based VLCs is thus beneficial for the highly efficient utilization of clean and renewable solar energy.

REFERENCES

1. The ionic radius and electronegativity of Nb, Ta and V elements and ions can be found from the below website of https://www.webelements.com.
2. Asahi R, Morikawa T, Irie H, et al. Nitrogen-doped titanium dioxide as visible-light-sensitive photocatalyst: designs, developments, and prospects. Chem Rev. 2014;114(19):9824-52.
3. Sun Q, Cortie D, Zhang S, et al. The formation of defect-pairs for highly efficient visible-light catalysts. Adv Mater. 2017;29(11):1605123.
4. Lin HY, Shih CY. Efficient one-pot microwave-assisted hydrothermal synthesis of M (M=Cr, Ni, Cu, Nb) and nitrogen co-doped TiO_2 for hydrogen production by photocatalytic water splitting. J Mol Catal A: Chem. 2016;411:128-37.
5. Zhang P, Yin S, Sekino T, et al. Nb and N co-doped TiO_2 for a high-performance deNOx photocatalyst under visible LED light irradiation. Res Chem Intermed. 2013;39(4):1509-15.

6. Breault TM, Bartlett BM. Lowering the band gap of anatase-structured TiO_2 by coalloying with Nb and N: electronic structure and photocatalytic degradation of methylene blue dye. J Phys Chem C. 2012;116(10):5986-94.
7. Breault TM, Bartlett BM. Composition dependence of TiO_2:(Nb, N)-x compounds on the rate of photocatalytic methylene blue dye degradation. J Phys Chem C. 2013;117(17):8611-8.
8. Breault TM, Brancho JJ, Guo P, et al. Visible light water oxidation using a co-catalyst loaded anatase-structured $Ti_{1-(5\,x/4)}Nb_xO_{2-y-\delta}N_y$ compound. Inorg Chem. 2013;52(16):9363-8.
9. Xu Z, Yang W, Li Q, et al. Passivated n-p co-doping of niobium and nitrogen into self-organized TiO_2 nanotube arrays for enhanced visible light photocatalytic performance. Appl Catal B: Environmental. 2014;144:343-52.
10. Cottineau T, Béalu N, Gross PA, et al. One step synthesis of niobium doped titania nanotube arrays to form (N, Nb) co-doped TiO_2 with high visible light photoelectrochemical activity. J Mater Chem A. 2013;1(6):2151-60.
11. Liu G, Yin LC, Wang J, et al. A red anatase TiO_2 photocatalyst for solar energy conversion. Energy Environ Sci. 2012;5(11):9603-10.
12. Lim J, Murugan P, Lakshminarasimhan N, et al. Synergic photocatalytic effects of nitrogen and niobium co-doping in TiO_2 for the redox conversion of aquatic pollutants under visible light. J Catal. 2014;310:91-9.
13. Chadwick NP, Glover EN, Sathasivam S, et al. Photo-activity and low resistivity in N/Nb co-doped TiO_2 thin films by combinatorial AACVD. J Mater Chem A. 2016;4(2):407-15.
14. Zhao YF, Li C, Hu JY, et al. Ta and N modulated electronic, optical and photocatalytic properties of TiO_2. Phys Lett A. 2016;380:910-6.
15. Le NT, Thanh TD, Pham VT, et al. Structure and high photocatalytic activity of (N, Ta)-doped TiO_2 nanoparticles. J Appl Phys. 2016;120(14):142110.
16. Obata K, Irie H, Hashimoto K. Enhanced photocatalytic activities of Ta, N co-doped TiO_2 thin films under visible light. Chem Phys. 2007;339(1):124-32.
17. Hoang S, Guo S, Mullins CB. Coincorporation of N and Ta into TiO_2 nanowires for visible light driven photoelectrochemical water oxidation. J Phys Chem C. 2012;116(44):23283-90.
18. Nakada A, Nishioka S, Vequizo JJ, et al. Solar-driven Z-scheme water splitting using tantalum/nitrogen co-doped rutile titania nanorod as an oxygen evolution photocatalyst. J Mater Chem A. 2017;23(5): 11710-9.
19. Long R, English NJ. Band gap engineering of (N, Ta)-codoped TiO_2: a first-principles calculation. Chem Phys Lett. 2009 Aug 27;478(4):175-9.
20. Jaiswal R, Patel N, Kothari DC, et al. Improved visible light photocatalytic activity of TiO_2 co-doped with vanadium and nitrogen. Appl Catal B. 2012;126:47-54.
21. Liu J, Han R, Zhao Y, et al. Enhanced photoactivity of V-N codoped TiO_2 derived from a two-step hydrothermal procedure for the degradation of PCP-Na under visible light irradiation. J Phys Chem C. 2011;115:4507-15.
22. Gu DE, Yang BC, Hu YD. V and N co-doped nanocrystal anatase TiO_2 photocatalysts with enhanced photocatalytic activity under visible light irradiation. Catal Commun. 2008;9(6):1472-6.
23. Zhong J, Xu J, Wang Q. Nitrogen and vanadium co-doped TiO_2 mesosponge layers for enhancement in visible photocatalytic activity. Appl Surf Sci. 2014;315:131-7.
24. Lu D, Zhang M, Zhang Z, et al. Self-organized vanadium and nitrogen co-doped titania nanotube arrays with enhanced photocatalytic reduction of CO_2 into CH_4. Nanoscale Res Lett. 2014;9:272.
25. Eswar NK, Ramamurthy PC, Madras G. Novel synergistic photocatalytic degradation of antibiotics and bacteria using V-N

doped TiO_2 under visible light: The state of nitrogen in V-doped TiO_2. New J Chem. 2016;40:3464-75.

26. Phattalung SN, Limpijumnong S, Yu J. Passivated co-doping approach to bandgap narrowing of titanium dioxide with enhanced photocatalytic activity. Appl Catal B. 2017;200:1-9.

Chapter 4. Main Achievements and Outlook

(1) Main achievements

Based on local defect structural design and new chemical synthesis strategies, a major difficulty to efficiently introduce difficult-dopant ions such as N^{3-} and In^{3+} into TiO_2 crystal structures at high concentrations through wet chemical synthesis routes, was solved. Two high-efficient TiO_2-based visible light catalysts were successfully synthesized for environmental remediation by directly using the clean and renewable solar energy; and one raw material for manufacturing new ceramic capacitors and new TiO_2 metastable polymorphic phases was achieved. The investigations on doping mechanisms, defect formation and associated impacts on material performances will not only benefit the future development of physical chemistry, material science and defect chemistry, but also open a new route to design novel multifunctional materials based on local defect structures in materials.

As the first author, four peer-reviewed papers have been published on Advanced Materials, The Journal of Physical Chemistry Letters, Crystal Growth & Design, and Research and Reviews in Electrochemistry, respectively. Another paper is now under review after submitting to journals. As the corresponding author, one peer-reviewed paper have been published on Solid State Communications. As one of co-authors, five peer-reviewed papers have been published or are under review. In addition, five patents have been applied and two conference presentations have been provided.

(2) Prospects

In view of the experimental results presented in this thesis as well as the recent research progress reported in the literatures, much possible continuing work should be further done for the development of high-efficient visible light catalysts and TiO_2-based ceramic capacitors designed in terms of electron-pinned defect dipole mechanism.

- The technological bottleneck for manufacturing (N^{3-}, Nb^{5+}) or (N^{3-}, Ti^{3+}) co-doped TiO_2-based visible light catalysts should be explored in order to large-scalely commercialize them. The potential technological barriers are mainly focused on the reaction homogeneity of the whole reaction systems at magnified conditions, the repeatability of prepared methods at different batches, as well as the stabilities of material properties.

- The application of (N^{3-}, Nb^{5+}) or (N^{3-}, Ti^{3+}) co-doped TiO_2-based visible light catalysts in the complicated and realistic environments should be further investigated. These environments not only include pH values of wastewater, the concentrations of heavy metal ions and different types of pollutants, but also are related to the effects on live creatures and the recycling of visible light catalysts.
- The technological requirement of using the synthesized (In^{3+}, Nb^{5+}) co-doped TiO_2 nanocrystals to prepare single-layer/multi-layer ceramic capacitors should be explored. The experimental or industrial methods to control defect states of (In^{3+}, Nb^{5+}) co-doped TiO_2 materials should be also investigated during sintering processes. The feasibility of using these small nanocrystals to prepare single-/multi-layer ceramic capacitors should be demonstrated.
- The doping mechanism about difficult- and easy-dopant ions should be further demonstrated in other co-doped material systems. The significant roles of local defect structure in other materials or for other physicochemical properties should be also investigated in the continuous research work. Furthermore, the direct experimental evidences for the presence of local defect structures would be found.

Chapter 5. Publications, Patents and Conference Presentations

Publications

- **Sun Q.**, Cortie D., Zhang S., Frankcombe T.J., She G., Gao J., Sheppard L.R., Hu W., Chen H., Zhuo S., Chen D., Withers R.L., McIntyre G., Yu D., Shi W. and Liu Y. The formation of defect-pairs for highly efficient visible-light catalysts. *Advanced materials (2017),* 29 (11), 1605123.
- **Sun Q.**, Huston L.Q., Frankcombe T.J., Bradby J.E., Lu T., Yu D., Zhou C., Fu Z. and Liu Y. Trans-regime structural transition of (In^{3+}+Nb^{5+}) co-doped anatase TiO_2 nanocrystals under high pressure. *Crystal Growth & Design (2017),* 17 (5), 2529-2535.
- **Sun Q.**, Zheng C., Huston L.Q., Frankcombe T.J., Chen H., Zhou C., Fu Z., Withers R.L., Norén L., Bradby J.E., Etheridge J. and Liu Y. Bimetallic ions co-doped nanocrystals: doping mechanism, defect formation and associated structural transition. *The Journal of Physical Chemistry Letters (2017),* 8, 3249-3255.
- **Sun Q.**, Zhang S., Cortie D., Frankcombe T.J., Gao J., Chen H., Withers R.L., Kremer F., Yu D., Brink F., McIntye G., Shi W. and Liu Y. Highly efficient visible light catalysts driven by Ti^{3+}-V_O-2Ti^{4+}-N^{3-} defect clusters. *Submitted to Journals* (Under Review).
- **Sun Q.**, McBride B.R. and Liu Y. (N^{3-}, M^{5+}) co-doping strategies for the development of TiO_2-based visible light catalysts. *Research and Reviews in Electrochemistry (2017)*, 8 (1), 106.
- **Sun Q.**, Perri G., Withers R.L. and Liu Y. A novel material for water and air purification. *Australian Science* (In Submission).
- Sun Y., Hu C., Huang J., Sun Y., Xue X. and **Sun Q**.* Magnetic evolution of nickel ion doped In_2O_3 nanocrystals under high magnetic field. *Solid State Communications (2017),* 261, 6-9.
- Yu D.H., Avdeev M., Sun D.H., Huston L.Q., Shiell T.B., **Sun Q.**, Lu T., Gu Q., Liu H., Bradby J.E., Yie N., Liu Y., Wang J.Y. and McIntyre G.J. Understanding the Unusual Response to High Pressure in $KBe_2BO_3F_2$. *Scientific Reports (2017)* 7, 4027.
- Sun Y., Sun Y., **Sun Q.** and Xiao X. Lightweight ceramsites prepared by the solid waste of semiconductor and textile dying industry. *International Journal of Modern Physics B (2017) DOI: 10.1142/S0217979217440970.*
- Hou L., Zuo K.H., **Sun Q.**, Xia Y.F., Ren Z.M., Lu X.G., Zeng Y.P. and Li X. Structure evolution and magnetic property of cobalt-modified $Bi_{0.9}Gd_{0.1}FeO_3$ nanocrystal at morphotropic phase boundary. *Journal of Alloys and Compounds (2015),* 650, 489-493.

- Awan M. Q., **Sun Q.**, Liu Y. and Ahmad J. Effect of higher manganese doping on structural and dielectric properties of lead free piezoelectric BNT ceramics. *Journal of the European Ceramic society* (Under review).

Patents

- Liu Y. Fu Z., **Sun Q.**, Withers R.L., Norén L. and Zhou C. Anatase-doped titanium dioxide material and preparation method and application thereof. *PCT patent (2016)*, CN 201610288912.
- Liu Y. **Sun Q.**, Shi W. and Withers R.L. Photocatalyst. *Australian provisional patent (2016),* 2016903458.
- Hu H., Zeng Y., Zuo K., Xia Y., Yao D. and **Sun Q.** Method for preparing silicon nitride/silicon carbide ceramic composite by use of reaction sintering process. *Chinese patent (2016)*, CN 201310077618.
- Hu H., Zeng Y., Zuo K., Xia Y., Yao D. and **Sun Q.** Method for preparing silicon nitride and silicon carbide complex phase porous ceramic by virtue of polycrystalline Si cutting wastes. *Chinese patent (2014)*, CN 201310178070.
- Hu H., Zeng Y., Zuo K., Xia Y., Yao D. and **Sun Q.** Silicon nitride/silicon carbide complex phase porous ceramic and preparation method thereof. *Chinese patent (2014)*, CN 201310178105.

Conference presentations

- The 2nd Australia-China Symposium on Colossal Permittivity Materials and Applications in Energy storage (ACCP-2), New South Wales, Koala, Australia, January 2016. Oral presentation.
- Materials Chemistry Symposium, University of New South Wales, Sydney, Australia, August 2016. Oral presentation.